

UNCLASSIFIED

SECURITY CLASSIFICATION OF THIS PAGE (When Data Entered)

REPORT DOCUMENTATION PAGE		READ INSTRUCTIONS BEFORE COMPLETING FORM
1. REPORT NUMBER NWC TP 6490	2. GOVT ACCESSION NO.	3. RECIPIENT'S CATALOG NUMBER
4. TITLE (and Subtitle) Experimental Data for Characterizing Perforating Impacts: Fragmentation Processes		5. TYPE OF REPORT & PERIOD COVERED Technical Publication FY 81 and FY 82
		6. PERFORMING ORG. REPORT NUMBER
7. AUTHOR(s) Marvin E. Backman and Stephen A. Finnegan		8. CONTRACT OR GRANT NUMBER(s)
9. PERFORMING ORGANIZATION NAME AND ADDRESS Naval Weapons Center China Lake, CA 93555-6001		10. PROGRAM ELEMENT, PROJECT, TASK AREA & WORK UNIT NUMBERS DNL TASK ZR00001
11. CONTROLLING OFFICE NAME AND ADDRESS Naval Weapons Center China Lake, CA 93555-6001		12. REPORT DATE May 1985
		13. NUMBER OF PAGES 94
14. MONITORING AGENCY NAME & ADDRESS (if different from Controlling Office)		15. SECURITY CLASS. (of this report) UNCLASSIFIED
		15a. DECLASSIFICATION/DOWNGRADING SCHEDULE
16. DISTRIBUTION STATEMENT (of this Report) Approved for public release; distribution unlimited.		
17. DISTRIBUTION STATEMENT (of the abstract entered in Block 20, if different from Report)		
18. SUPPLEMENTARY NOTES		
19. KEY WORDS (Continue on reverse side if necessary and identify by block number) Damage Mechanisms, Penetration, Hypervelocity, Missile Warheads, Impact, Fragment Clouds, Perforation		
20. ABSTRACT (Continue on reverse side if necessary and identify by block number) See reverse side of this form		

(U) Experimental Data for Characterizing Perforating Impacts: Fragmentation Processes, by Marvin E. Backman and Stephen A. Finnegan. China Lake, Calif., Naval Weapons Center, May 1985. (NWC TP 6490, publication UNCLASSIFIED.)

(U) The impact of compact projectiles against plates has been investigated to improve the phenomenological description of the impact and perforation processes, especially at those speeds at which the projectile and target show significant breakup. This investigation identifies and characterizes the internal failure processes involved in perforation and fragmentation. It employs momentum and energy balances to characterize the dynamics of the system of fragments expelled following perforation. The experimental data cover a range of impact speeds from 0.5 to 3.0 Km/s. Data have been collected on a total of nine combinations of projectile and plate parameters but are most complete for four combinations of mild steel spheres fired against plates of steel and aluminum alloys of thickness approximately equal to the sphere diameter.

(U) Fractures that develop on or near adiabatic shear zones dominate the fracture mechanisms within the projectile and plate. Other fractures run between the fractures of the slip-line pattern established by the adiabatic shears. Momentum measurements and measurements of the velocities and masses of exit-debris indicate that fragments from the plug and fragments from a region peripheral to the plug involve distinct dynamic processes. This analysis indicates that the peripheral fragments derive their momentum from momentum transferred to the plate during the process of plug formation and perforation.

Experimental Data for Characterizing Perforating Impacts: Fragmentation Processes

by
Marvin E. Backman
and
Stephen A. Finnegan
Research Department

MAY 1985

// **NAVAL WEAPONS CENTER
CHINA LAKE, CA 93555-6001**



Approved for public release;
distribution unlimited.

Naval Weapons Center

AN ACTIVITY OF THE NAVAL MATERIAL COMMAND

FOREWORD

The research described in this report was performed during fiscal years 1981 and 1982 and supported by Navy Director of Laboratories Program Task Assignment ZR00001. It is part of a continuing effort to improve the foundation for the design methodologies applied to penetrating weapons in interaction with a wide spectrum of penetration resistant target elements.

This report is released at the working level. Because of the continuing nature of the research the work may be modified and extended.

This report has been reviewed for technical accuracy by John Pearson, Research Department.

Approved by
E. B. ROYCE, Head
Research Department
11 December 1984

Under authority of
K. A. DICKERSON
Capt., U.S. Navy
Commander

Released for publication by
B. W. HAYS
Technical Director

NWC Technical Publication 6490

Published by Technical Information Department
Collation Cover, 48 leaves
First printing 200 copies

CONTENTS

Introduction	3
A Survey of Perforation Phenomena	3
Summary of Failure Processes	8
Elastic and Plastic Deformation	8
Major Systems of Fragments	18
Plugging	19
Fragmentation of the Central Region	22
Peripheral Region	25
Fragmentation Processes in Representative Impact Systems	42
A Summary of the Systems	42
Comparison of Fragmentation in Targets of Three Steels and $T/d = 1$	43
Fragmentation of Aluminum Targets Struck by Aluminum Spheres	78
Conclusions	91
Nomenclature	92

INTRODUCTION

The present work comprises one part of a phenomenological investigation of the impact of a system of fragments against a compartmented structure. This part investigates the fragmentation processes that occur in the impact of a single projectile against a plate. The experimental data cover a range of impact speeds from 0.5 to 3.0 Km/s. This range includes the impact speeds for most projectiles and many warhead fragments and at the upper part of the range impacts produce considerable fragmentation of the projectile and target. The data of this report correlate the impact speed of the projectile and parameters that characterize the configuration of the projectile and plate to the internal failure processes that cause the formation of a crater, perforation of the plate, and the development of systems of fragments.

Data have been collected on a total of nine combinations of projectile and plate parameters. The data are most complete for four combinations of deforming spheres fired against aluminum alloy plates, plates of a U.S. armor, plates of a Soviet armor, and plates of 4130 steel in which plate thicknesses were approximately equal to the sphere diameter. These systems, although restricted in configuration, represent a configuration of interest in design and analysis, and avoid certain complexities arising from extensive lateral deformations of systems with low ratios of plate thickness to sphere diameter and other complexities in the modes of internal failure that occur in the perforation of still thicker plates. The remaining systems involve cubes rather than spheres or treat other ratios of plate thickness to projectile diameter.

A SURVEY OF PERFORATION PHENOMENA

When a projectile strikes a plate it moves the contact surface so as to form a crater that has comparatively uniform curvature and approximates a part of a spherical surface. The far side of the plate develops a corresponding bulge. The plate resists this deformation with forces that squash the front of the projectile and spread it laterally over the crater. As the impact speed increases the crater and bulge become larger and the region between them becomes more deformed. Perforation occurs when the region of the plate between crater and bulge develops internal ruptures or fractures so that the deformed projectile can

pass through. As the impact speed increases still further the internal failures in both the plate and the projectile increase in number and extent resulting in a system of fragments that passes into the region beyond the plate.^{1,2,3}

A series of firings of 6.35 mm mild steel spheres against 6.15 mm mild steel plates illustrate typical features of perforating impact for a compact projectile, *i.e.*, *one with its major dimensions approximately equal*. Spheres provide the ultimate in geometric simplicity since orientation of the projectile has no role in the impact process. Compact projectiles of more complicated shapes exhibit systematic departures from the data for spheres due to the differences introduced by shape and orientation. Mild steel was used because most warheads have mild steel cases that produce compact fragments. Furthermore, mild steel exhibits material characteristics common to several armors and structural steels but its large ductility gives uniformity of material behavior over a greater range of impact speeds than these more brittle materials.

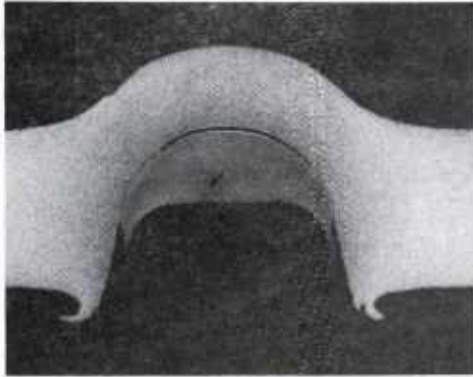
Figure 1 shows three cross-sections of impact craters in mild steel plates arranged in order of increasing speed of impact. The changes illustrate the trends in the mechanism of crater formation. These show the development of a crater and rear surface bulge in Figure 1(a), and the progressive enlargement of the crater and bulge in Figures 1(b) and 1(c). In addition, Figure 1(b) shows the initiation of fractures that eventually separate a plug-shaped piece of the plate immediately ahead of the sphere, as shown in Figure 1(c). At still higher speeds the projectile pushes the plug out of the plate and passes through the aperture formed by removal of the plug. The lowest speed at which the sphere passes through the plate is called the ballistic limit.

At impact speeds above the ballistic limit the processes of fracture that formed the plug continue to break up the plug and parts of the plate adjacent to the plug. The projectile has undergone deformations that cause an increase in the diameter of the crater. As in the plate, the deformations of the sphere result in breakup of the sphere. Thus increasing impact velocity leads to an increasingly fragmented system that emerges from the plate.

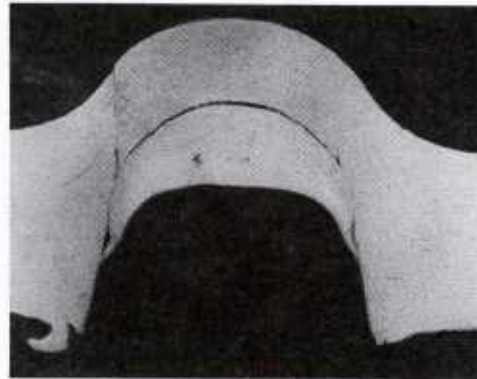
¹Backman, M. and W. Goldsmith. "The Mechanics of Penetration of Projectiles into Targets," *Int. J. Engng. Sci.*, Vol. 16, (1978) pp. 1-99.

²Naval Weapons Center. *Terminal Ballistics*, by Marvin E. Backman. China Lake, CA, NWC, February 1976. 230 pp. (NWC TP 5780, publication UNCLASSIFIED.)

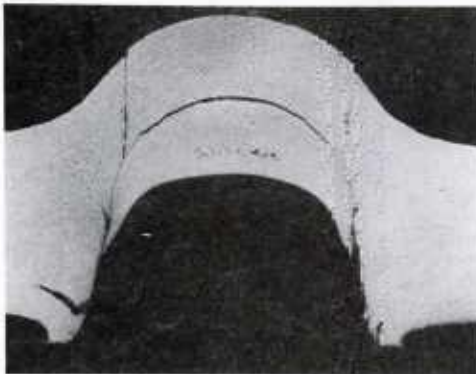
³Goldsmith, W. *Impact*, London, Edward Arnold, 1960, p. 379.



(a) Simple crater



(b) Beginning of plugging



(c) Plugging complete

FIGURE 1. Three Cross Sections of Impact Craters.

Figure 2 shows a series of fragment patterns behind a perforated plate. These were obtained by a Kerr cell camera and illustrate the progressive changes in the fragment system as impact velocity increases. At velocities just above the ballistic limit the plug is the only target fragment but with further increases in impact speed the number of fragments increase and have increasing speed off the original line-of-flight. The speed of the lead fragment \hat{V} depends on the impact speed V as shown in Figure 3. Such data can usually be fitted by the expression

$$\hat{V} = R \sqrt{V^2 - V_0^2} \quad (1)$$

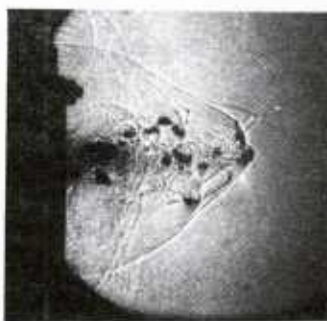
to within about 5%.⁴ The parameters R and V_0 are constants, and V_0 corresponds to the ballistic limit of the system.



(a) Plug only



(b) Plug and projectile



(c) Moderate breakup



(d) Extensive breakup

FIGURE 2. High Speed Photographs of Fragment Systems.

⁴Recht, R. and T. W. Ipson. "Ballistic Perforation Dynamics," *J. Appl. Mech.*, Vol. 30, Series E, No. 3 (Sept 1963), pp. 384-389.

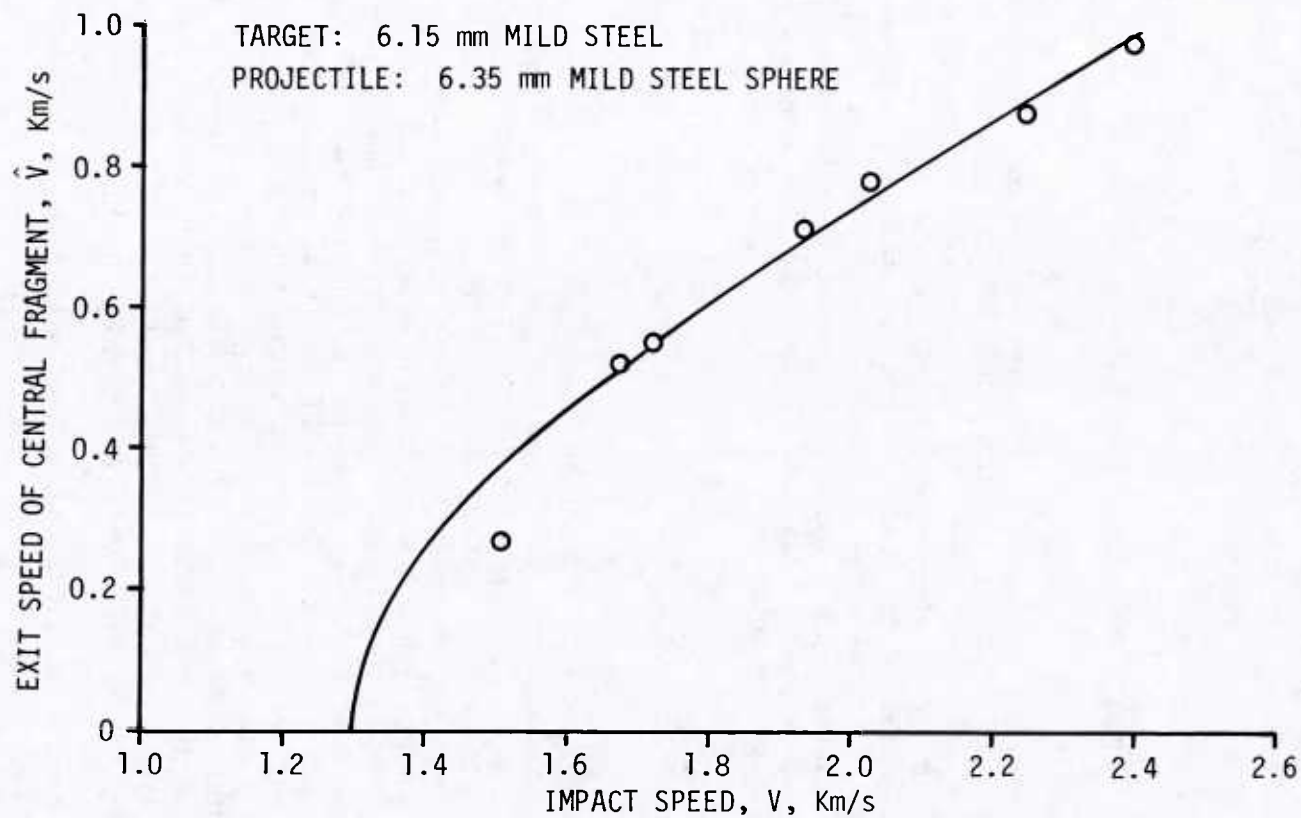


FIGURE 3. Residual Speed of the Lead Fragment as a Function of Impact Speed (mild steel sphere, mild steel plate $T/d \approx 1$).

The fragments other than the lead fragment have a component of motion off the line-of-flight of the lead fragment. The angle between the line-of-flight of the given fragment and the line-of-flight of the lead fragment specifies the direction of the given fragment. Figure 4 shows that the largest value of this angle for a given fragment system tends to increase with increasing impact speed above the ballistic limit up to a maximum value.

SUMMARY OF FAILURE PROCESSES

A given impact system, such as the mild steel sphere and mild steel plate, when subjected to increasing impact speeds has certain similarities to a static material test. The region between crater and bulge corresponds to the test specimen and increasing impact velocity corresponds to successive increases in the force applied to the specimen. In both the static and ballistic impact tests the specimen exhibits a sequence of material responses beginning with elastic, changing to plastic and ending up with failure of the specimen. This section describes the sequence exhibited by the ballistic impact test.

ELASTIC AND PLASTIC DEFORMATION

Elastic deformation, *i.e.*, deformation that completely recovers when the load is removed, predominates only below the lowest speeds considered in the present work. At 0.5 Km/s plastic deformations of considerable magnitude produce a well-defined crater. Although from the microscopic view plastic deformations depend on lattice imperfections and are therefore intrinsically inhomogeneous, from the macroscopic point of view plastic deformations are as homogeneous as elastic deformations. In a range of impact speeds just above 0.5 Km/s the interaction between a spherical deformable projectile and a plate of common alloys of steel and aluminum occurs exclusively by macroscopically homogeneous deformations. The usual methods of posing and solving the problem of the dynamics of impact come from continuum mechanics. Equations for the conservation of mass, momentum and energy and constitutive equations that describe the known properties of dynamic plastic deformations comprise the governing equations for the response of each body to boundary conditions specified at a variable contact surface.⁵ At low velocities it proves possible to linearize the governing equations and develop solutions to the impact

⁵Wilkins, M. L. "Calculation of Elastic-Plastic Flow," in *Methods in Computational Physics*, Vol. 3, New York, Academic Press, (1964) pp. 211-263.

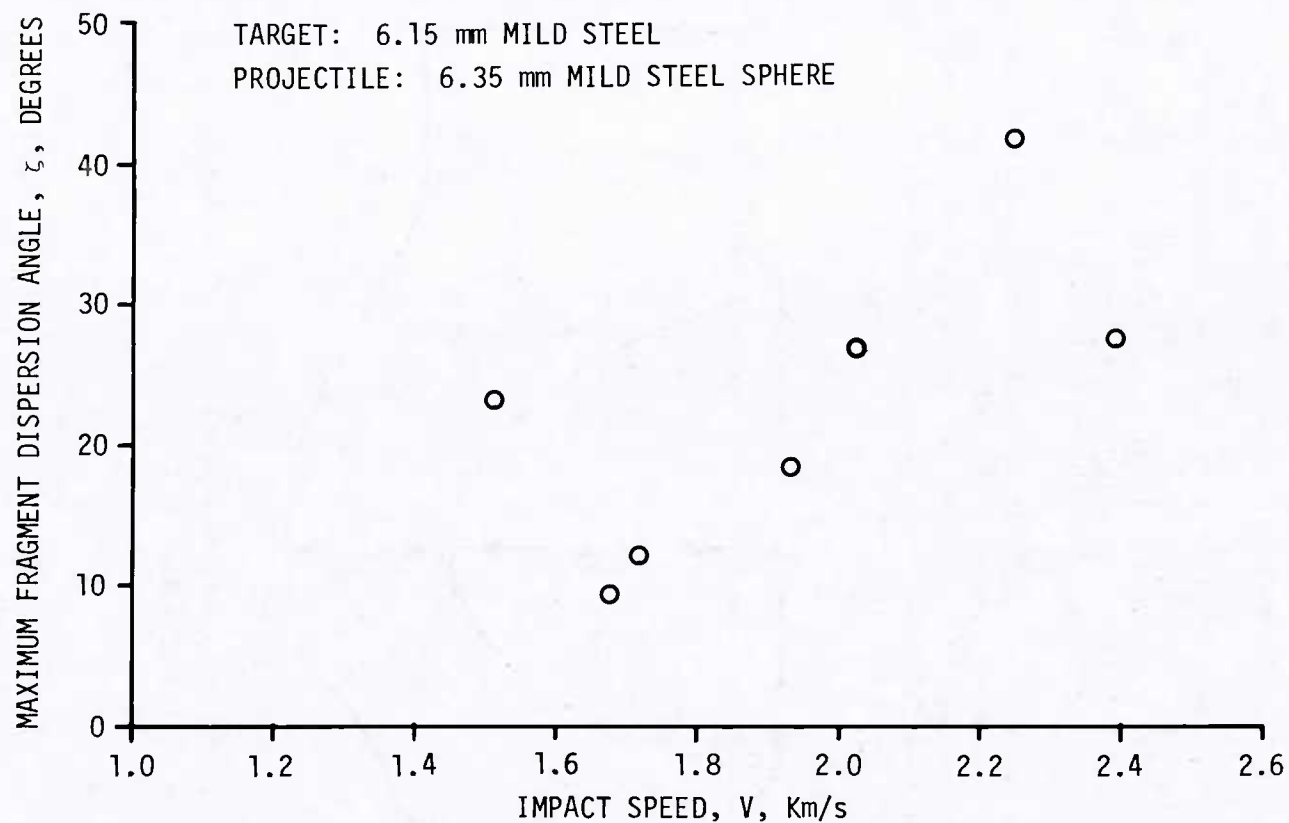


FIGURE 4. Maximum Dispersion Angle for Fragments as a Function of Impact Speed (mild steel sphere, mild steel plate, $T/d \approx 1$).

problem in terms of wave propagation models. In the regime of interest here the magnitude of displacements rules out such linearization. Solutions by finite difference or finite element numerical methods give solutions to impact problems that predict most if not all of experimentally observed features of impact described above.⁶ In fact, the degree of agreement between numerical solutions to impact problems and actual observations (such as crater shape and dimensions) provide evidence that the numerical model predicts the salient features of impact dynamics reasonably well and in considerable detail. For most applications the expense of these solutions prohibits extensive use. Certainly for most characterizations of the behavior of an impact system the direct collection of the experimental data cost less than the numerical simulation.

Measurements on the craters provide the data that readily characterizes the final effect of the impact. For the target, the penetration P , crater diameter at the front of the plate D , and the axial thickness H comprise the basic measurements of configurational change. The definition of these measurements is illustrated in Figure 5.

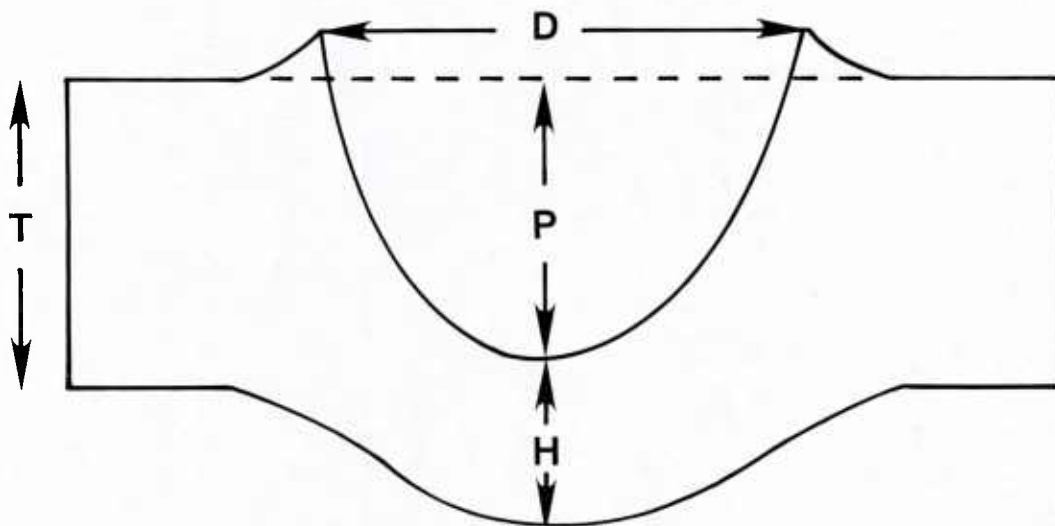


FIGURE 5. Diagram of the Basic Measurements of Configurational Change of the Target.

⁶Chandra J. and J. E. Flaherty, Editors. "Computational Aspects of Penetration Mechanics, *Lecture Notes in Engineering, Army Research Office Workshop on Computational Aspects of Penetration Mechanics*, Ballistic Research Laboratory, Aberdeen Proving Ground, MD, 27-29 April, 1982.

The craters have spherical to oval shapes so that the gross plastic strains can be estimated by mean strains ϵ_1 and ϵ_2 defined from P, D, and H as follows:

$$\epsilon_1 = 1 - H/T \quad (2)$$

$$\epsilon_2 = \sqrt{4(P/D)^2 + 1} - 1 \quad (3)$$

where T is the thickness of the plate. Each of these definitions uses the basic crater measurements to define a relative change in dimensions, ϵ_1 the relative change in thickness, ϵ_2 the relative elongation of the material along the crater bottom (using an ellipse with axis P and D/2 to approximate the crater cross-section). These parameters characterize the craters, show the development of crater formation as velocity increases, and afford a means for defining these parameters even though a central fragment has begun to separate from the target. Figure 6 shows the development of these strains for mild steel.

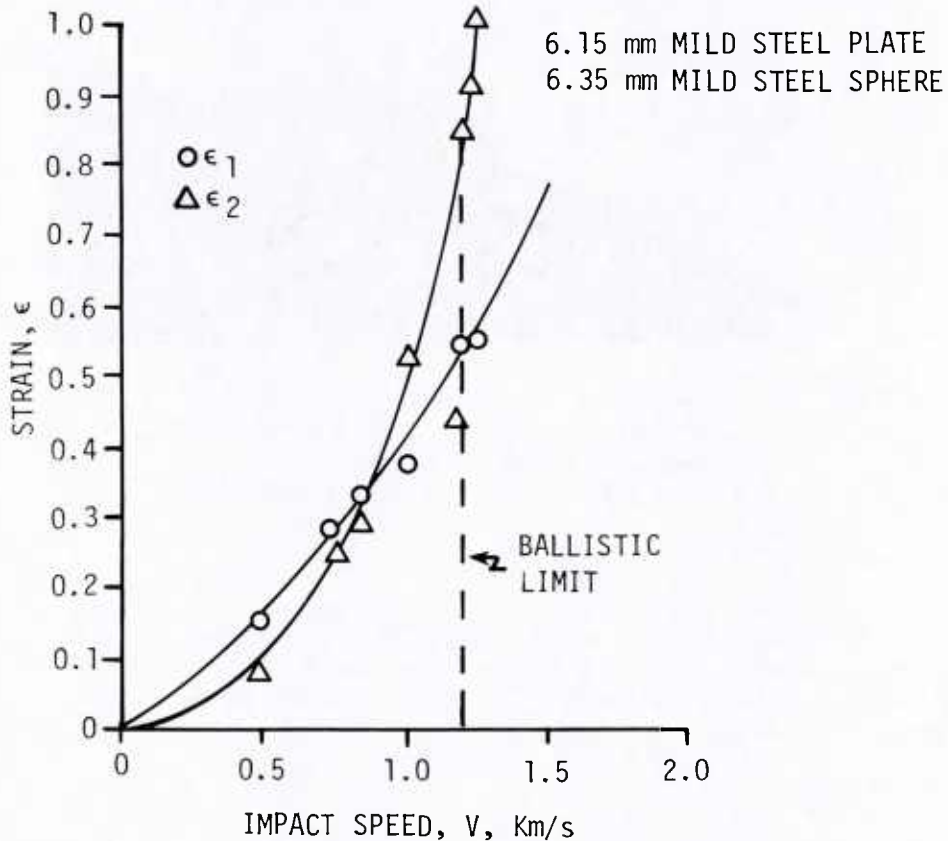


FIGURE 6. Mean-Strains as a Function of Impact Speed (mild steel sphere, mild steel plate, $T/d \approx 1$).

Inhomogeneous Plastic Deformations

Above some critical point (ϵ^*, V^*) on the mean-strain velocity curve for a particular projectile and plate the nature of plastic strains changes. Inhomogeneous plastic strains occur on a macroscopic scale, *i.e.*, extremely narrow bands of intense shear become obvious from sharp shifts of the crater boundary. Figure 7 shows an enlarged section of a crater boundary that exhibits a shift due to an inhomogeneous shearing process. In polished and etched cross sections of craters the distortion of the microstructure of the material reveals the details of the inhomogeneous shear.

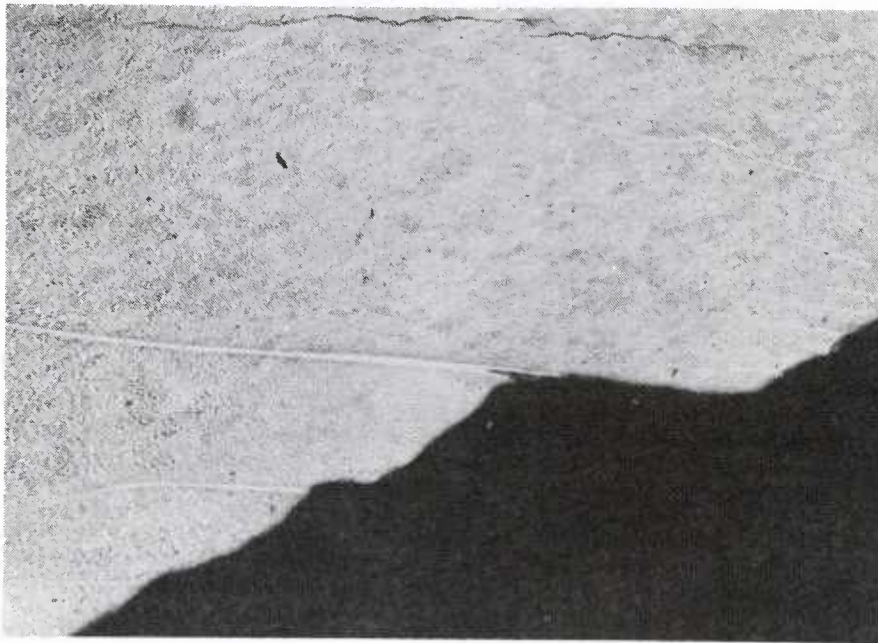


FIGURE 7. A Section of a Crater Boundary Showing an Inhomogeneous Shear Band (mild steel sphere, 4130 steel plate, $T/d \approx 1$, $V = 1.2$ Km/s, 100X magnification).

Metallurgical examination of impact and explosively loaded materials reveal these narrow bands of intense deformation for a wide range of materials and loading conditions.⁷ Such bands exist in warhead fragments and comprise the mechanism that underlies one method of fragment control.

⁷Rogers, H. C. *Adiabatic Shearing - A Review*, Drexel U., U.S. Army Research Office (1974).

Impacts against high strength metals in the ordnance velocity range and higher virtually always produce these bands. In spite of great frequency of occurrence and a fair amount of work on them these bands are not well understood. A recent survey summarizes the status of work on these phenomena and has many references to work on the subject.⁸ The prevailing opinion is that an initial shear inhomogeneity of low intensity causes localized heating that in turn increases the deformation through thermal softening resulting in growth of the inhomogeneity. The phenomena intrinsically belong to conditions of rapid and intense loading because the rate of localized plastic deformation must heat the material more rapidly than the cooling by conduction. These bands develop by the unstable localization of continuous plastic deformation processes and frequently but not invariably result in fracture. The fractures that do follow shear banding have a variety of properties of their own, making it most appropriate to consider these fractures phenomenologically distinct from the inhomogeneous plastic deformations.

Inhomogeneous plastic failures have patterns similar to those predicted by slip-line analysis.⁹ This can be seen in Figure 8 which compares the patterns of inhomogeneous shears (A) to theoretical calculations of slip lines for a purely compressive distribution of stress around a spherical crater (B). Figure 8 exploits the fact that for this material there is a close relationship between fracture and inhomogeneous plastic failure since this macrograph of the crater actually shows fractures and thus makes the plastic failures visible. The theoretical relationship between the pattern of inhomogeneous plastic failure lines will be developed in greater detail in a later section.

Craters in thick plates ($T/d \approx 2$) reveal an effect of granular structure on the direction of inhomogeneous shear banding. Thick plates of more homogeneous materials develop inhomogeneous shears and fractures on inward directed slip surfaces, Figure 9. Thick plates with rolling texture develop inhomogeneous shear bands and fractures on outward directed slip surfaces and the outer extremities of these surfaces follow the texture of the plate, Figure 10. At impact velocities below the minimum velocity for perforation isolated failures are occasionally observed along the direction of the rolling texture as the result of the bending deformations of the plate that occur in crater formation, Figure 11. An explanation of these differences in behavior of materials with textural differences is that a tendency to fail along the rolling direction under bending deformations overrides the normal tendency to follow the inward directed family of slip surfaces.

⁸The National Research Council. "Adiabatic Shear Banding," in *Materials Response to Ultra-High Loading Rates*, Chapter 8, NMAB-356, (1980), pp. 129-142.

⁹Backman, M. E. and S. A. Finnegan. "The Propagation of Adiabatic Shear," in *Metallurgical Effects at High Strain Rates*, ed. R. W. Rhode, et. al., Plenum (1973).

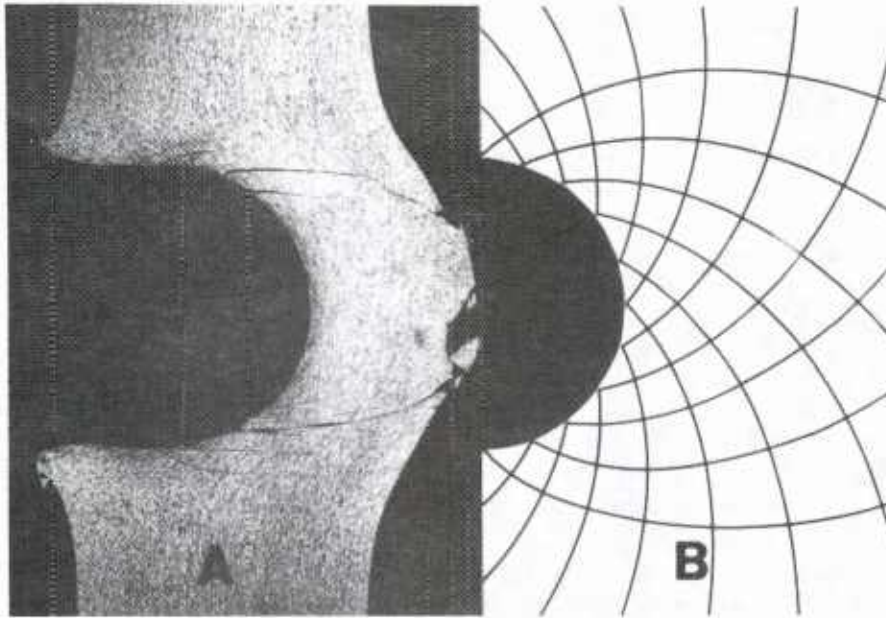


FIGURE 8. (A) Slip-Line Pattern for Compressive Stresses About a Spherical Crater, (B) Theoretical Calculations of Slip Lines. (Hard steel sphere, 2024-T4 aluminum plate, $T/d \approx 1$, $V = 0.56$ Km/s.)

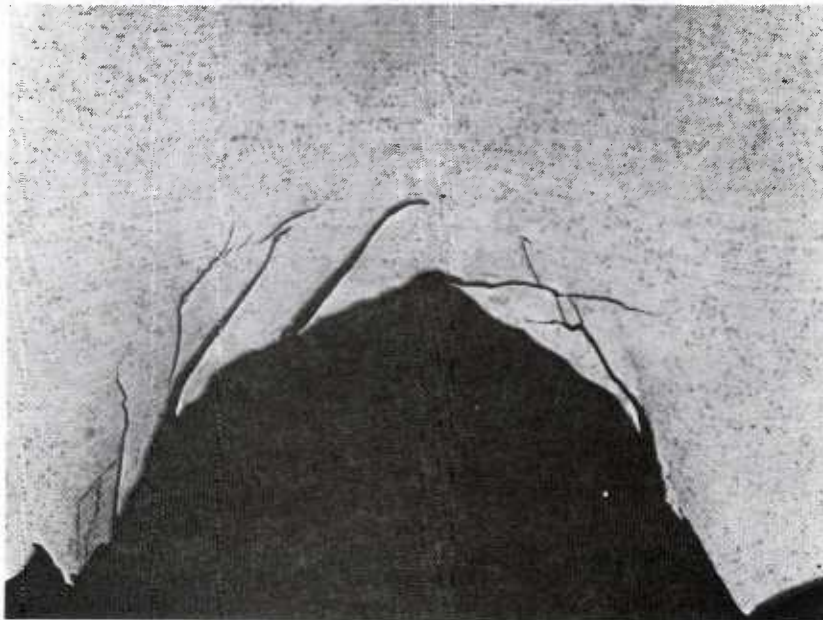


FIGURE 9. Fractures in a Thick Homogeneous Plate. (Mild steel sphere, 4340 steel plate, $T/d = 4$, $V = 2.4$ Km/s.)

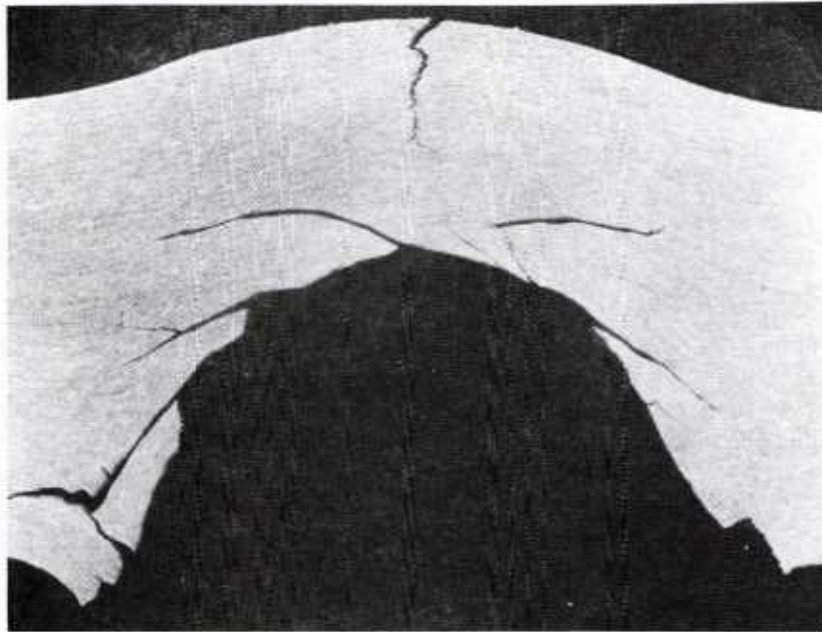


FIGURE 10. Fractures in a Thick Plate with Rolling Texture. (Aluminum sphere, 2024-T4 aluminum plate, $T/d = 2$, $V = 2.7$ Km/s.)

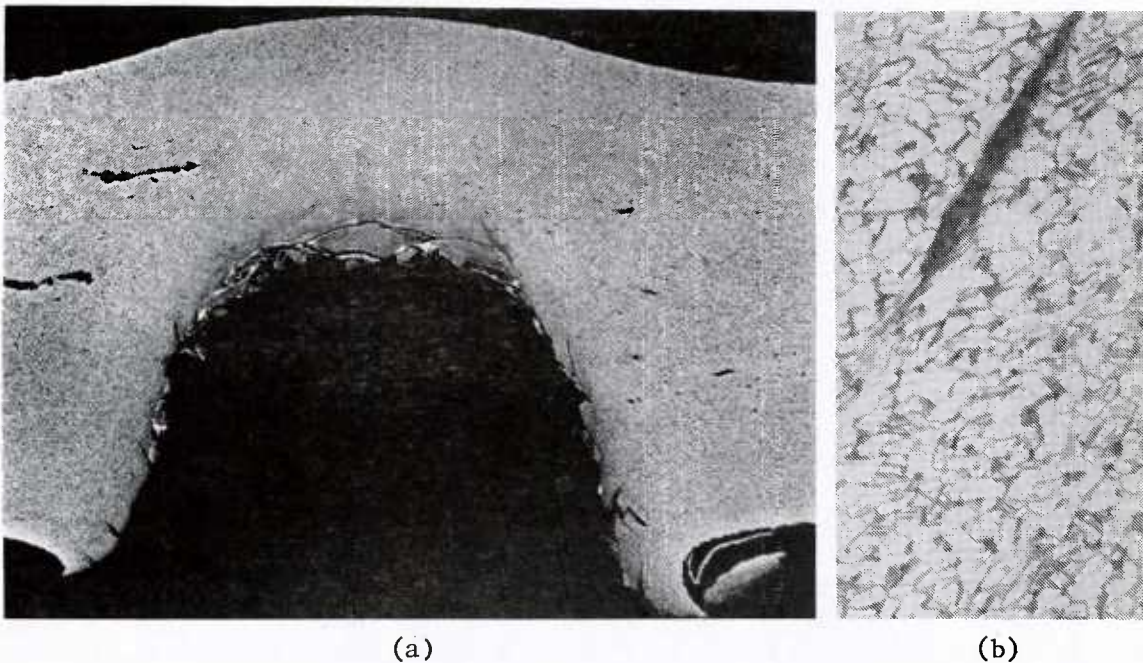


FIGURE 11. Shear Fractures and Associated Fractures Due to Bending Alone.
(a) Mild steel sphere, 4130 steel plate, $T/d = 2$, $V = 2.6$ Km/s
(b) Mild steel sphere, mild steel plate, $T/d = 1$, $V = 1.3$ Km/s
200X magnification

Fractures

Mean-strain-velocity curves may also be used to identify the conditions for fracture in the plates of the present impact system. The fractures can be identified on the basis of microscopic examination according to standard quasi-static types, ductile fracture, brittle fracture, and with either transcrystalline or intercrystalline forms; however, the occurrence of these impact fractures solely in regimes of inhomogeneous plastic failure makes them uniquely dynamic.

All of the materials that developed inhomogeneous shear bands also developed fractures that showed the influence of the inhomogeneous deformations by proximity to the shear bands and similarity between the pattern of fracturing and the pattern of the shear bands. Microscopic examination indicates that the fracture mechanisms vary with the material and location in the body. The fracture mechanisms appear to have the same forms commonly observed under quasi-static loading but the close association with inhomogeneous plastic failure justifies consideration of these fractures as a different class.

Microscopic examination of the fractures associated with shear bands reveals a great variety of fracture phenomena. In most of the materials that produce the bands we have called deformed shear bands, the mechanism of fracture appears to be ductile and involves a progressive separation of the material at the crack tip and normal to the crack surface but with the crack surface coincident with the slip surface for the shear band. An example is shown in Figure 12. Some materials for which this conclusion holds are 70-30 brass, 60-40 brass, 2024-T4 aluminum alloy, titanium alloys, and some 4130 tempered martensites.

Materials that fail by inhomogeneous shear and form transformed shear bands,⁷ *i.e.*, bands that show signs of having undergone a change of phase, exhibit more complex forms of fractures than those for deformed zones. In one region a single fracture may open up along the center of the band, but further along the same band the fracture pattern may change to a series of short fractures running diagonally across the band. Examples of these fracture phenomena are shown in Figure 13. These observations of multiple fracturing within the band and diagonal fracturing that extends beyond the band suggest that the processes of band formation and fracturing are to some extent independent.

In addition to these fractures on or near inhomogeneous plastic failure other fractures develop during impact that either occur away from inhomogeneous shears or in completely unrelated directions. In some cases these fractures may be due to stress-wave interaction, *i.e.*, spalling. In other cases these fractures resemble the fractures that radiate from the axis of symmetry to form petals in the perforations of very thin targets. Figure 14 shows a plug of 2024-T4 aluminum alloy that exhibits tensile fractures that emanate from an origin at the axis of symmetry of the plug.

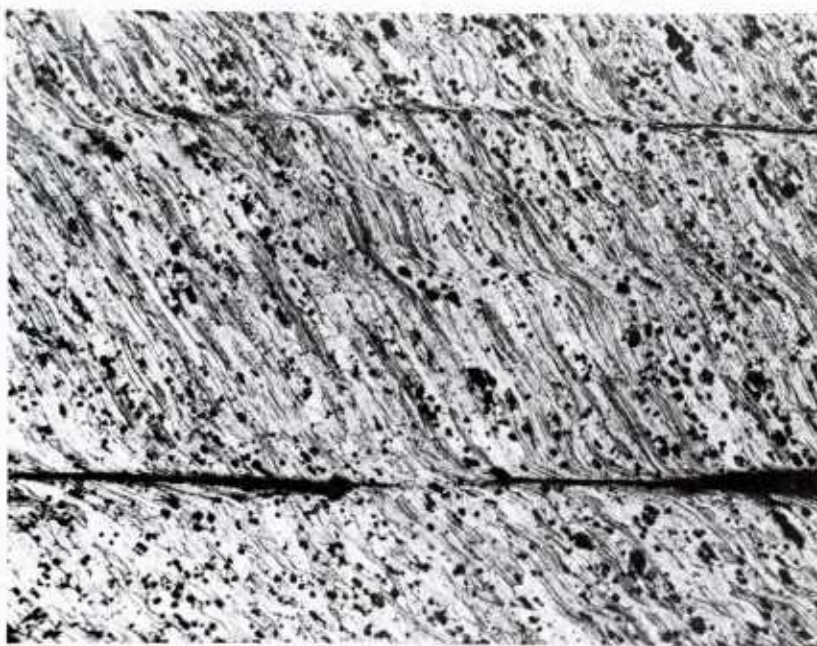


FIGURE 12. Plug Fragmentation Along an Inhomogeneous Shear Band. (2024-T4 Aluminum, 100X magnification.)

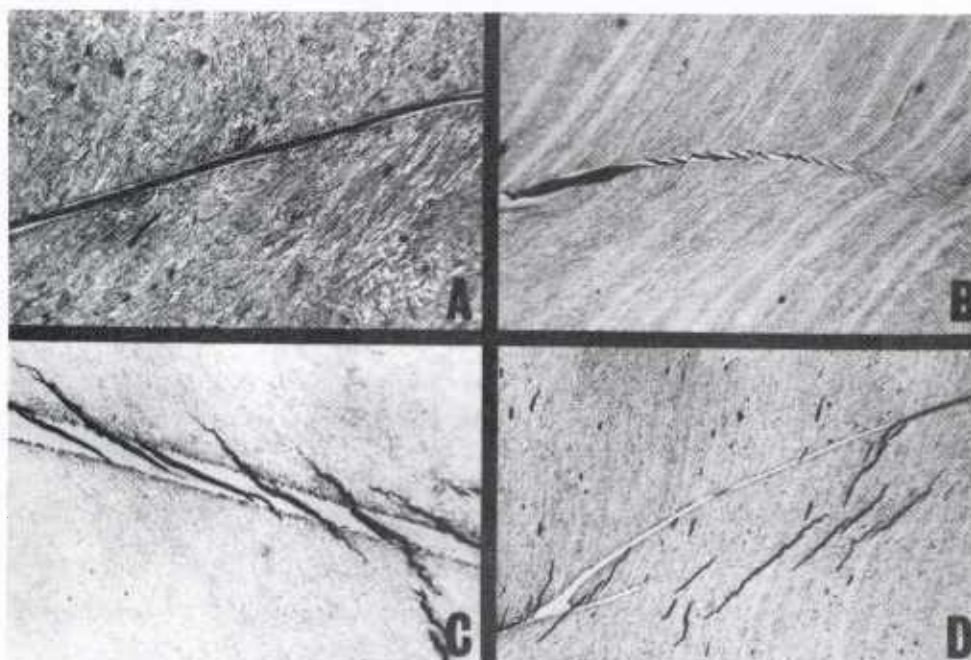


FIGURE 13. Fractures in or Near Transformed Shear Bands. (4130 steel, various magnifications.)

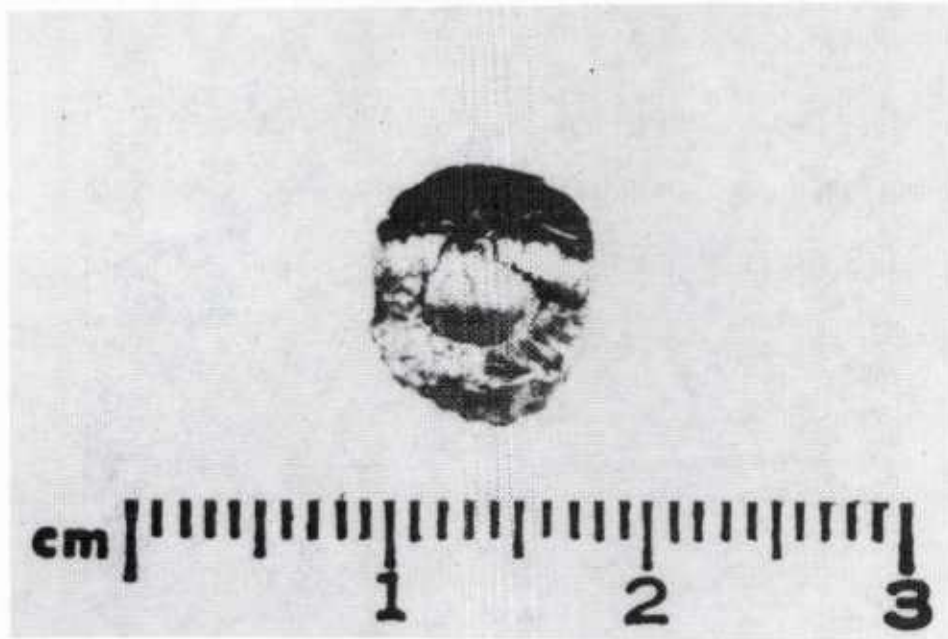


FIGURE 14. Radial Tensile Fractures. (Aluminum sphere, 2024-T4 aluminum, $T/d = 1$, $V = 1.6$ Km/s.)

MAJOR SYSTEMS OF FRAGMENTS

The deformation and fracture processes outlined above individually or in consort produce a system of fragments. Near the ballistic limit the result is a single fragment but as the impact speed increases the number of fragments also increases. This section summarizes and systematizes observations on these fragmentation processes and the kinematics of the systems of fragments in order to identify distinct regions of the plate and projectile from which the fragments come. The sections that follow will identify three source-regions in the plate; (1) on the entry side of the plate fragments come from the edges of the crater, (2) on the exit side of the plate fragments come from a central region, and (3) from a peripheral region surrounding the central region. These regions are shown in Figure 15 by the shaded areas.

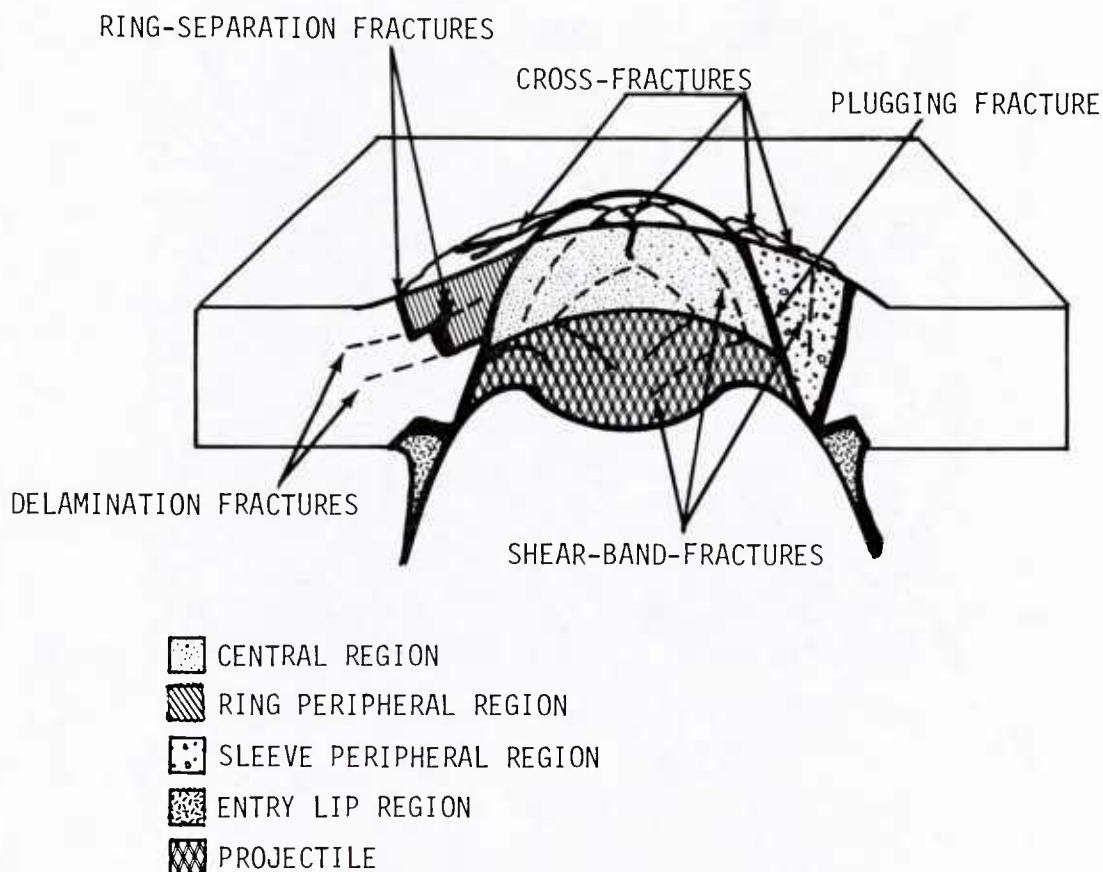


FIGURE 15. Impact Fragmentation Pattern.

PLUGGING

Impacts in a range of speeds just above the lowest speed for perforation form a single fragment, the plug. In this speed range the separation of the fragment occurs over a roughly axially symmetric surface by a process commonly called plugging because of the shape of the fragment that it forms. Figure 15 shows this surface of fragmentation. Our principal data on this fracture process come from a series of firings against plates of several materials and the examination of cross-sections by metallurgical microscopy. The examination of incipient plugging, for impacts below the ballistic limit, reveals two significantly different failure processes. In targets of material such as 60-40 brass, 2024-T4 aluminum alloy, and 4130 steel with tempered martensite structure, plugging fractures are associated with inhomogeneous plastic failures, *i.e.*, fractures either occur along the zones of inhomogeneous shear (60-40 brass, for example, see Figure 16) or near the zone. On the other hand very ductile steels such as SAE 1020 or pearlitic or spheroidized martensitic microstructures exhibit plugging by a rupture process (similar to normal

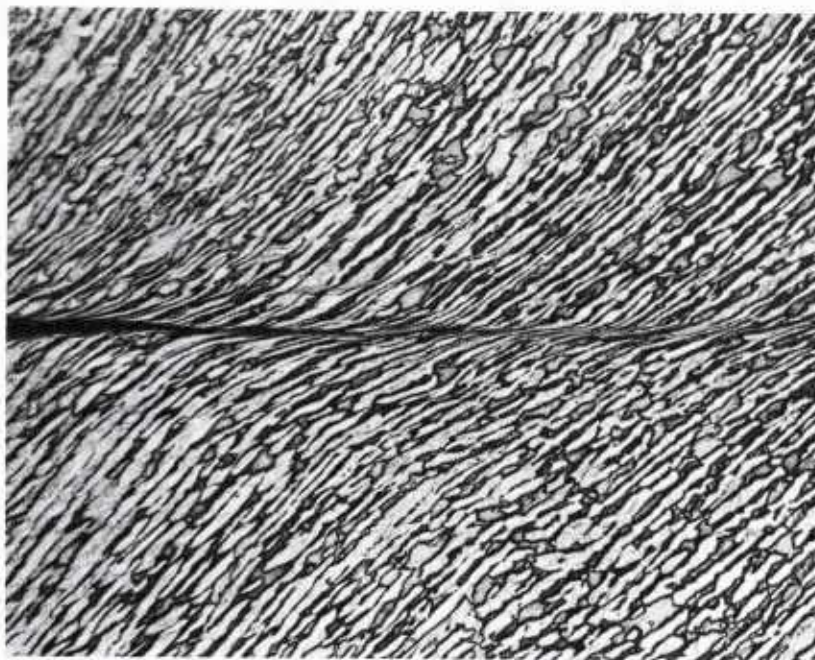


FIGURE 16. Plugging Along a Band of Inhomogeneous Shear. (Mild steel sphere, 60-40 brass target, $T/d = 1$, $V = 1.1$ Km/s, 100X magnification.)

rupture) with no evidence of any inhomogeneous plastic failures (see Figure 17). These materials do exhibit inhomogeneous plastic failure under explosive loading (Pearson and Finnegan)¹⁰ and may also exhibit this mode of failure at higher velocities than studied here.

The curvature of these plugging surfaces depends on both the parameter T/d and the impact speed V . For $T/d = 1$ and at speeds near the ballistic limit the surfaces have the least curvature and tend to traverse directly across the plate. As speed increases the surfaces tend to increase in curvature and to converge toward the axis of symmetry. Figure 18 illustrates this tendency by a series of macrographs for two materials arranged from left to right in order of increasing impact speed. For lower values of T/d the same trends exist but do not develop as far, so that for a very thin plate the fracture surface almost turns out cylindrical and corresponds to the assumptions made.⁴ All of these qualitative observations support the hypothesis that the tangents to the surfaces follow directions of maximum shear.⁹

¹⁰Pearson, John and S. A. Finnegan. "A Study of the Material Failure Mechanisms in the Shear-Control Process," Chapter 13, *Shock Waves and High Strain-Rate Phenomena in Metals*, Ed. by M. A. Meyers and L. E. Murr, Plenum, pp. 205-218 (New York, 1981).

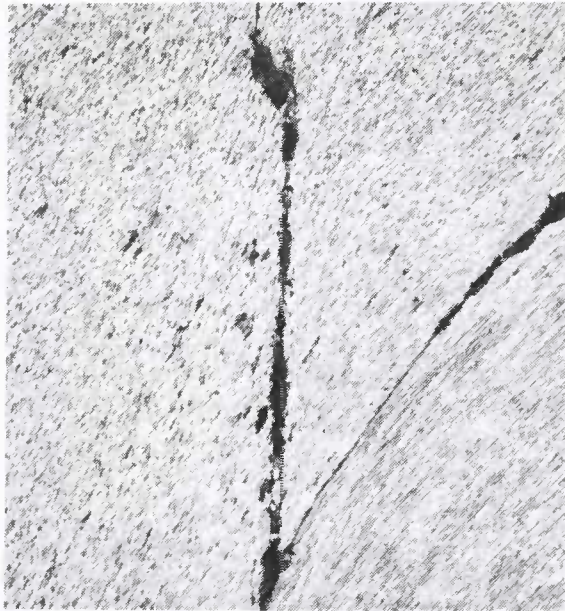
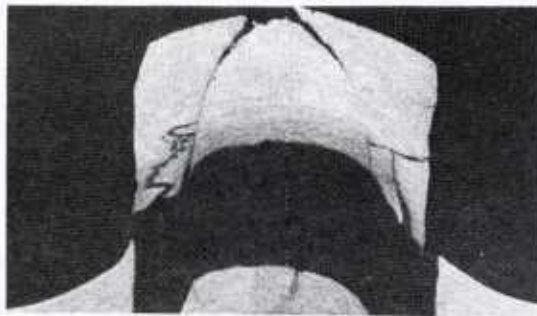
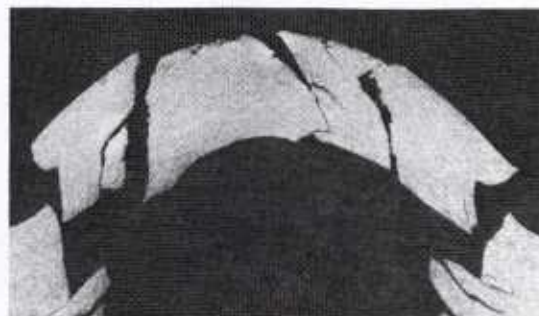


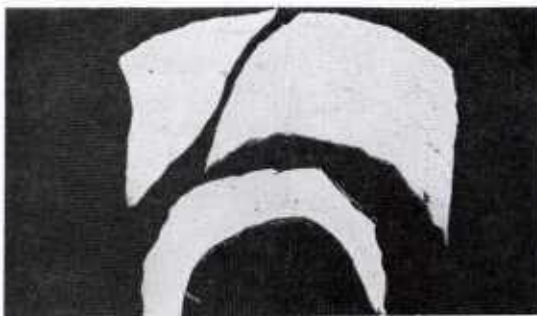
FIGURE 17. Plugging by Ductile Rupture. (Mild steel sphere, mild steel plate, $T/d = 1$, $V = 1.3 \text{ Km/s}$, 50X magnification.)



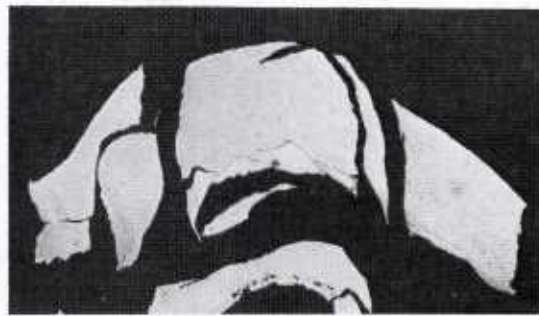
1.6 Km/s



2.0 Km/s



1.7 Km/s



1.8 Km/s

FIGURE 18. Cross Sections of Craters and Reassembled Ejecta for Two Target Systems and Impact Speeds. (Top: Aluminum sphere, aluminum plate, $T/d = 1$, Bottom: Mild steel sphere, U.S. armor plate, $T/d = 1$.)

FRAGMENTATION OF THE CENTRAL REGION

For any of the plates with $T/d \approx 1$ the range of impact speeds in which a single fragment emerges from the plate extends only a few hundred meters per second above the ballistic limit. For example, Figure 19 shows data for mild steel plates in the form of the number of recovered fragments for impact speeds from the ballistic limit to 2.4 Km/s. The figure suggests a range of about 0.1 Km/s as the speed range for the formation of a plug alone. Above this range the central region becomes increasingly fragmented. Some indications of the mechanism of fragmentation come from the examination of plugs recovered intact, cross-sections of these plugs, and recovered plug fragments. In many instances one can reconstruct the plug from the recovered fragments and gain insight into the nature of the fragmentation process. These various means of observation indicate the following families of fractures contributed to fragmentation:

(1) Shear-band fractures. This form of fracture exists in a wide range of materials. In addition to the materials mentioned in the Introduction as the principal materials for this study, isolated tests on several other materials showed the development of inhomogeneous plastic shear bands into internal fractures within plugs. These follow directions of maximum shear as shown in Figure 15. The fractures always resemble this pattern but do not necessarily have the complete symmetry of Figure 15. Figure 20 shows several cross-sections of plugs that illustrate the diversity of the occurrence of these fractures.

(2) Cross-fractures that join shear-band fractures. The examination of plugs, either recovered intact or reconstructed, reveals cross-fractures that connect the roughly axisymmetric shear band fractures that comprise the principal patterns of crater cross-sections. The direction of these cross-fractures varies from direct traversal of the region separating the shear bands to oblique traversal of the region depending on the plate material and possibly on the configuration and impact speed. Observations on these failures are far less complete than for the shear band fractures seen in crater cross-sections. In some materials it appears that the irregularities and asymmetries of the shear band fractures cause these to intersect one another and form discrete fractures without cross-fractures (Figure 20(a)).

(3) Spalls. These failures result from stress-wave interactions following reflections from free surfaces in which the reflection process changes compressive stresses to tensile stresses.^{10,11} The process depends on the net tensile stress wave having sufficient impulse to cause

¹¹Rinehart, John S. *Stress Transients in Solids*. Santa Fe, NM, HyperDynamicS, 1975, p. 230.

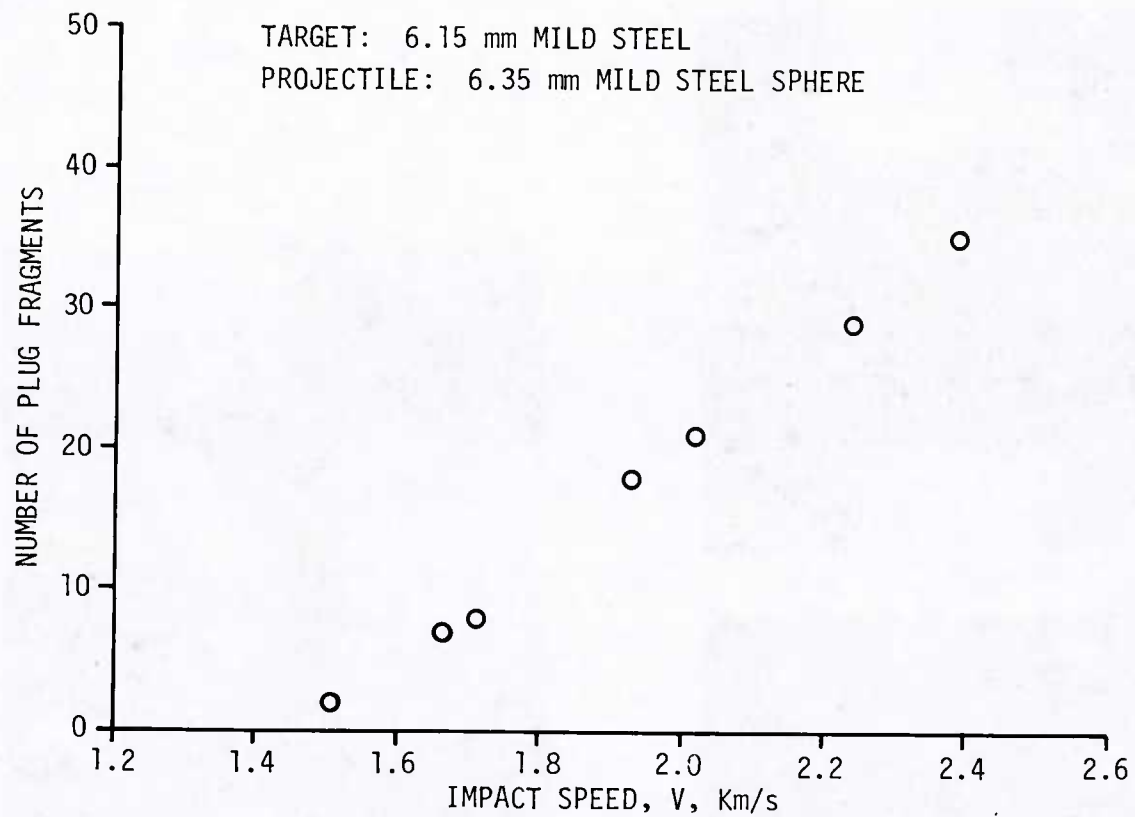
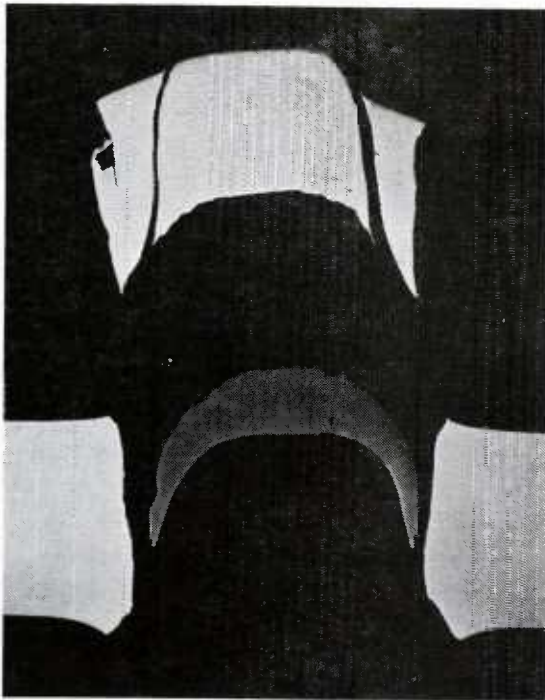
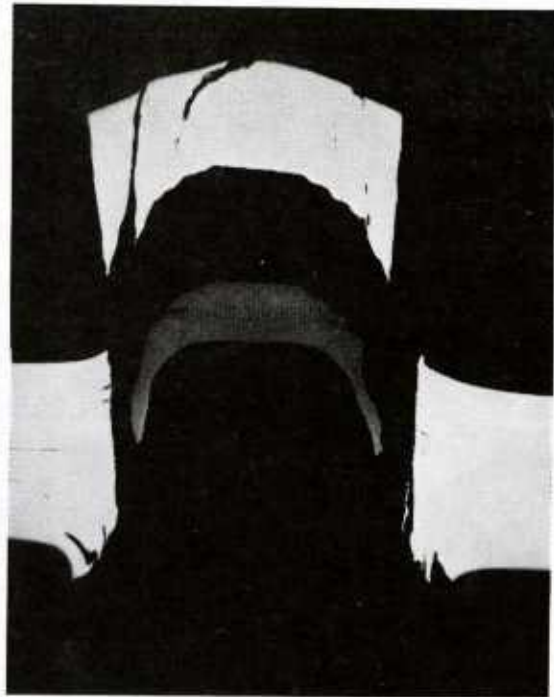


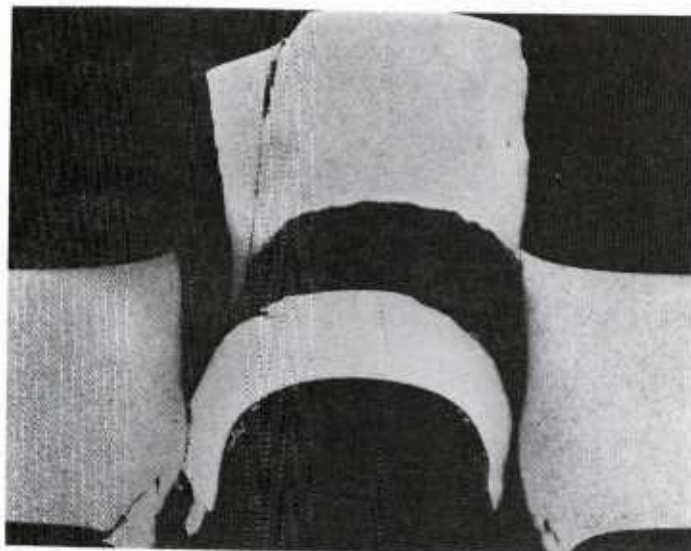
FIGURE 19. Number of Fragments from the Central Region as a Function of Impact Speed. (Mild steel sphere, mild steel plate, $T/d = 1.$)



(a) 1.3 Km/s



(b) 1.7 Km/s



(c) 1.2 Km/s

FIGURE 20. Examples of Variations in Fragmentation Patterns in the Central Region. (Mild steel sphere, Soviet armor plate, $T/d = 1.$)

failure. In the materials and range of impact speeds of interest here this form of fracture occurs infrequently and predominantly in the less ductile materials and at the higher impact speeds.

PERIPHERAL REGION

In certain materials failures occur at the periphery of the crater as impact speed increases beyond a critical value. Such materials have planes of weakness parallel to the plane of the plate, and fractures (which we call delaminating fracture) occur along these planes (Figure 15). A separate set of fractures (which we call ring separation fractures) then develops perpendicular to these planes. The net result of the combined processes is to separate a ring-shaped fragment from the peripheral region. The contributing fractures are shown in Figure 21 and examples of the reassembled rings are shown in Figure 22. Peripheral fragmentation for materials with a definite rolling texture is clearly quite different from the peripheral fragmentation of more homogeneous materials and these differences are apparently due to differences in the granular structure.

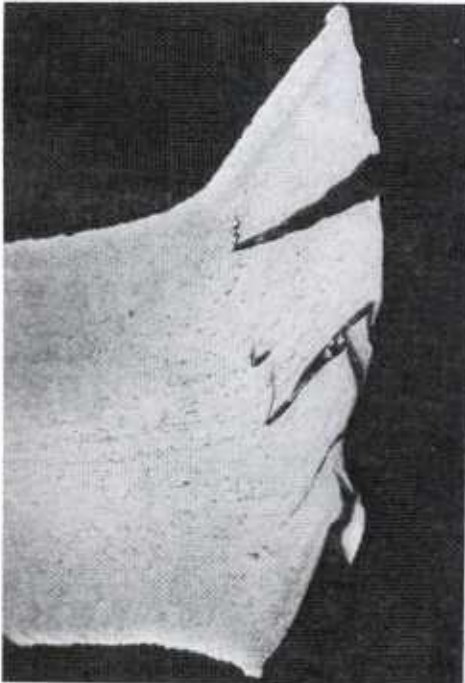


FIGURE 21. Fractures Responsible for Ring Formation. (Mild steel sphere, U.S. armor plate, $T/d = 1.$)

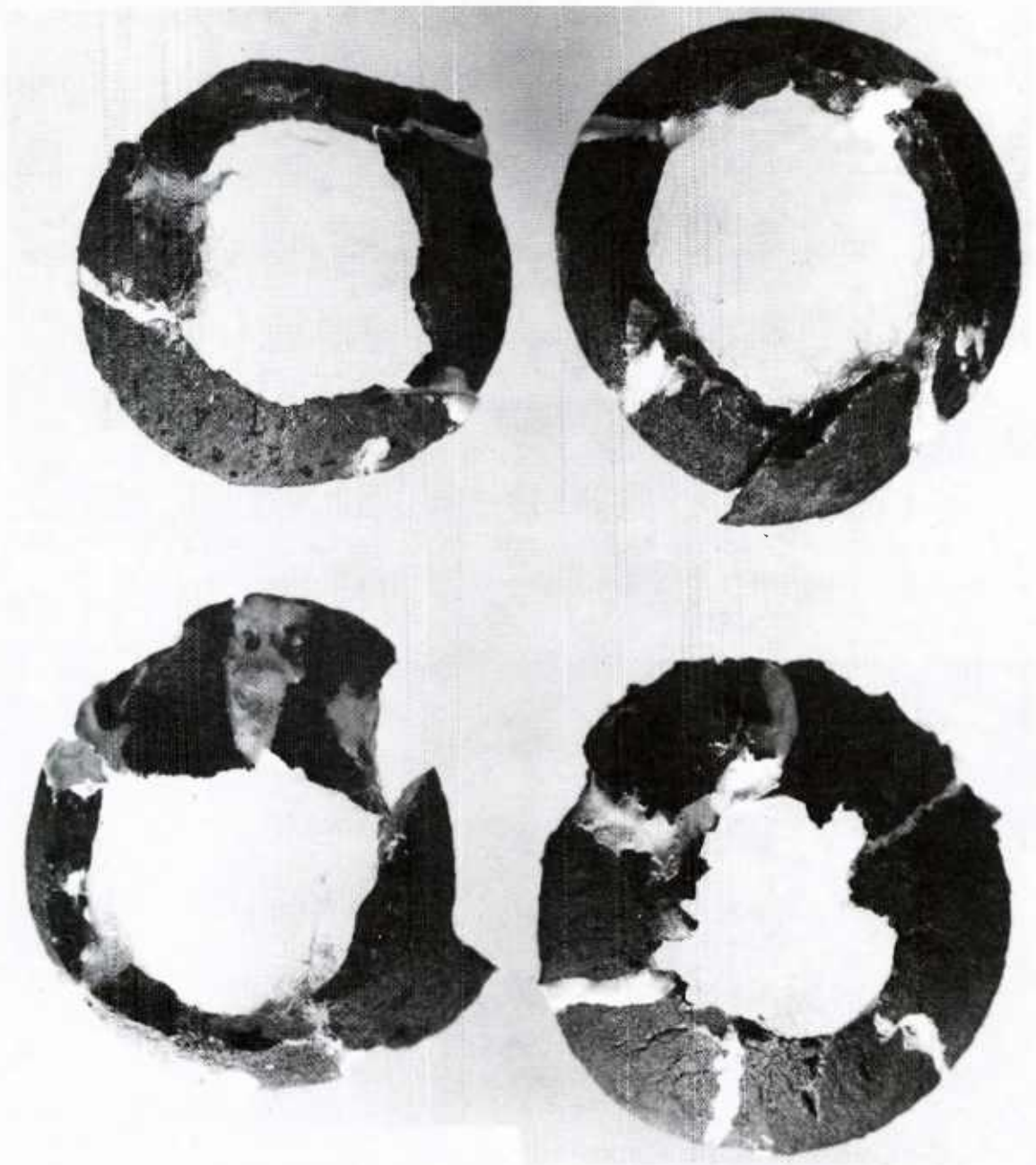


FIGURE 22. Reassembled Rings. (Mild steel sphere, U.S. armor plate, $T/d = 1.$)

While the evidence from recovered fragments strongly supports the development of separate and distinct rings and plugs some recovered fragments show evidence of both processes. Figure 23 shows a plug with ring attached. This kind of fragmentation may occur consistently for a very limited range of impact conditions or simply as an occasional statistical oddity.

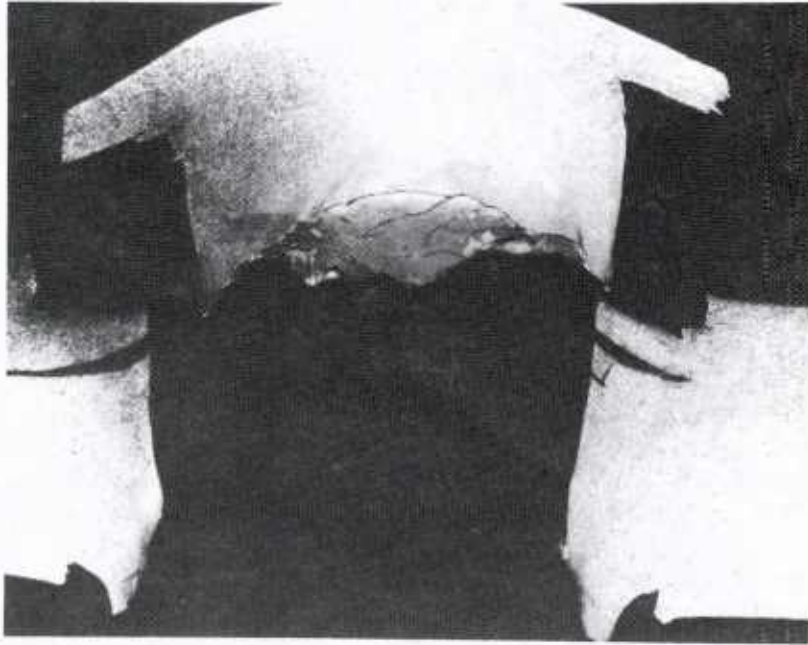


FIGURE 23. A Ring and Plug Joined. (Hard steel sphere, 4130 steel plate, $T/d = 1$, $V = 1.3 \text{ Km/s.}$)

Some evidence that fragments from the peripheral region have significantly different behavior from those of the central region come from measurements of the momentum transferred to the target as a function of impact speed and the inferences that can be drawn from such measurements on the minimum speed for perforation. It proves convenient to begin with a simple system. In Footnote 4 momentum and energy conservation applied to idealized impacts by cylinders against thin plates lead to the conclusions that the speed of the center of mass of the plug projectile systems \bar{V} after perforation has the value

$$\bar{V} = \frac{m_p}{m_p + m_q} \sqrt{V^2 - V_x^2} \quad (4)$$

in which V_x , the minimum-perforation velocity, has a constant value if the work done in separating the plug from the plate remains constant. For this idealized system the momentum transferred to the plate becomes

$$L = m_p V \left(1 - \sqrt{1 - \left(\frac{V_x}{V} \right)^2} \right) \quad (5)$$

and solving this equations for the parameter V_x yields

$$V_x = V \sqrt{1 - \left(1 - \frac{L}{m_p V} \right)^2} \quad (6)$$

Measurements of the residual velocity and momentum transferred to the plate show that the above equations hold for a very hard sphere perforating thin plates of mild steel and a titanium alloy. The points in Figure 24 present measurements of residual speed of a 6.35 mm sphere fired against 1.47 mm mild steel plates as a function of impact speed. The solid line shows a fit of Equation 4 to these data by an appropriate choice of m_q and the parameter V_x . Figure 25 shows correlations of measurements of the momentum transferred to the plate to impact speed and compares these to predictions of transferred momentum given by Equation 5 using the selected value of V_x . Figure 26 shows the computations of V_x made from the measurements of momentum according to Equation 6 and the fact that the momentum measurements do imply a constant value for the parameter V_x . Figures 27, 28 and 29 show the same sequence of curves for the system consisting of a 4.76 mm sphere and a 1.50 mm thick plate of Ti-8Al-1Mo-1V titanium alloy. Figure 27 shows the fit of residual speed data to Equation 4. Figure 28 shows the agreement between the momentum data and Equation 5 and Figure 29 shows the implied constancy of the parameter V_x .

A mild steel sphere and a thicker plate of steel or aluminum alloy comprises a system in which the projectile deforms and the mechanism of crater formation changes with increased speed so that the conditions for a constant V_x do not exist. In that case V_x does indeed depend on the impact speed and one can determine V_x from the momentum transferred to the plate by the equation

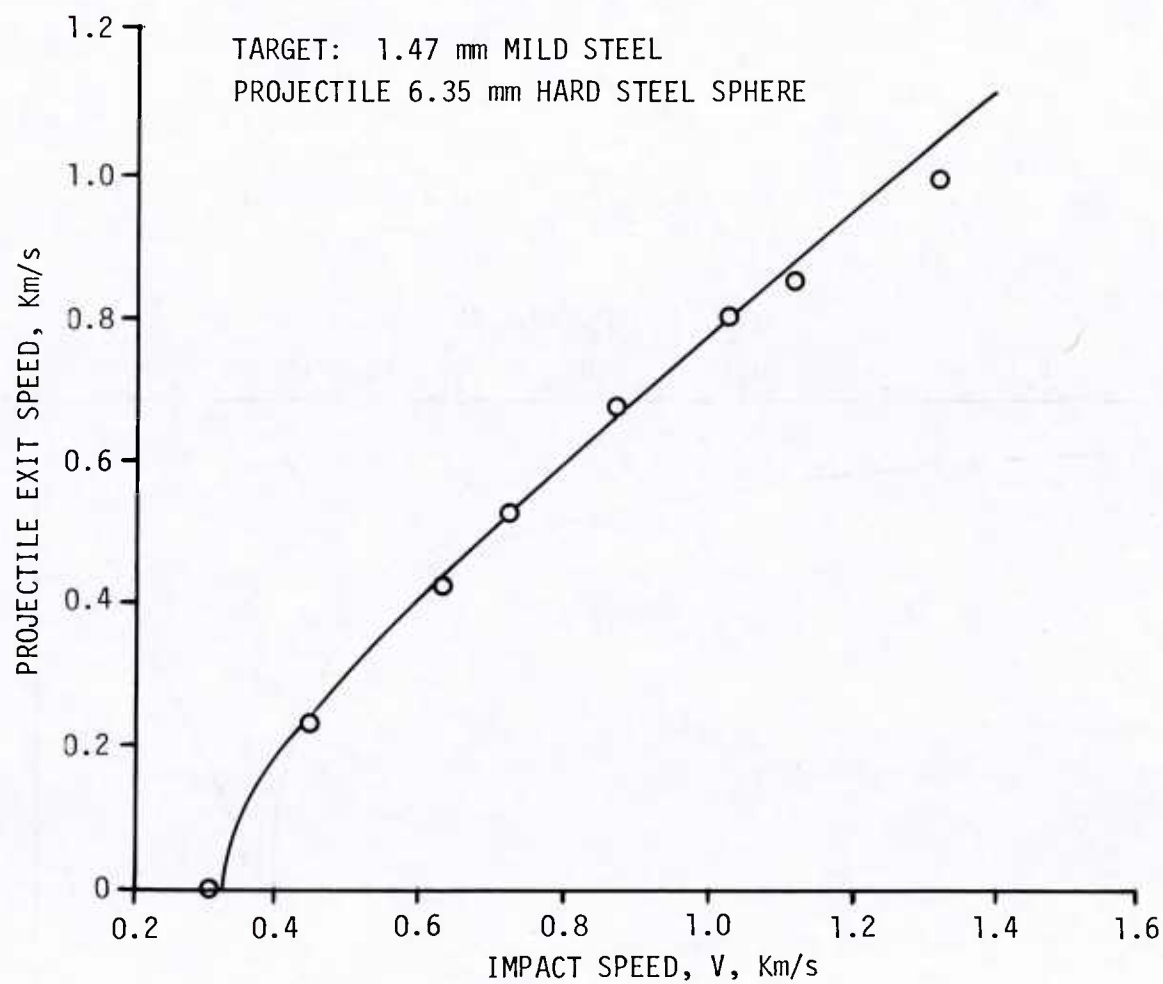


FIGURE 24. Residual Speed of the Projectile as a Function of Impact Speed.
(Hard steel sphere, mild steel plate, $T/d = 0.25$.)

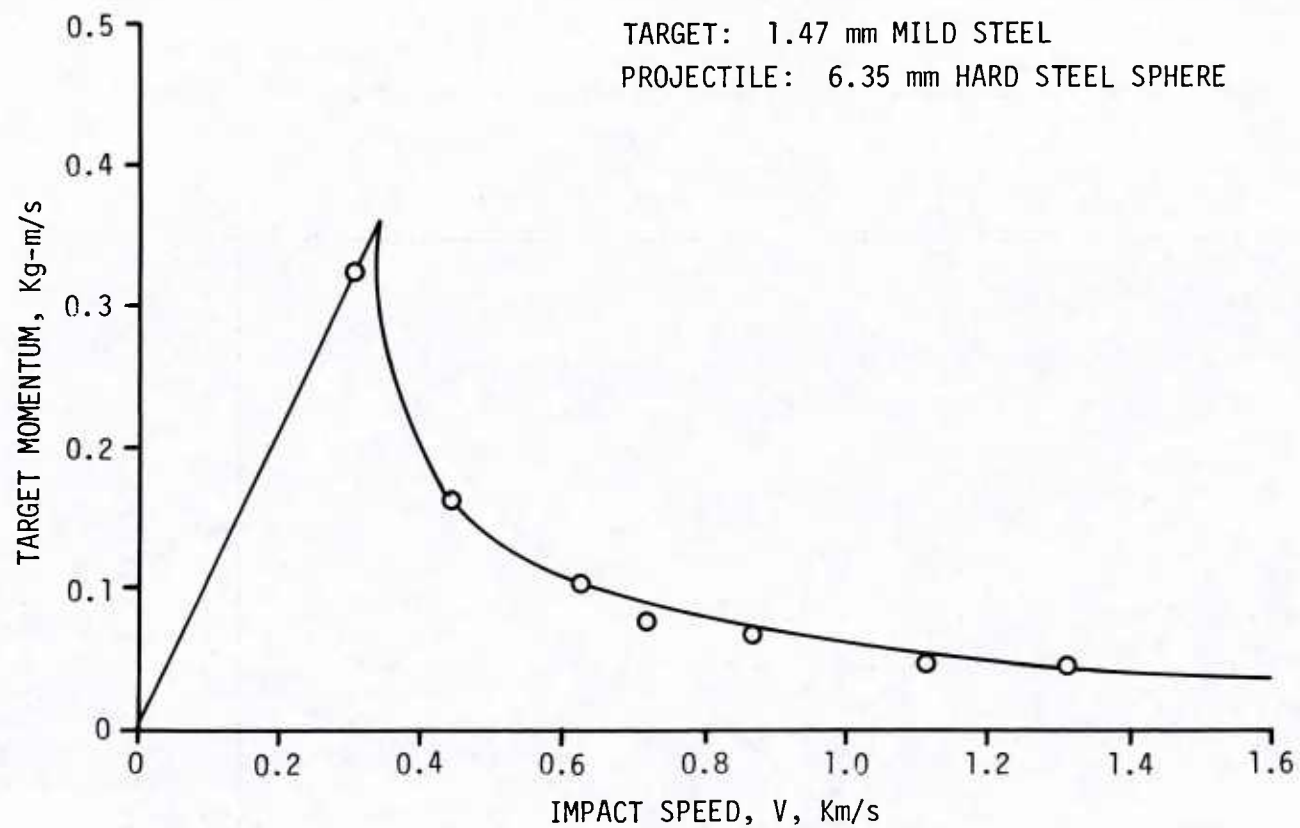


FIGURE 25. Target Momentum as a Function of Impact Speed.
(Hard steel sphere, mild steel plate, $T/d = 0.25$.)

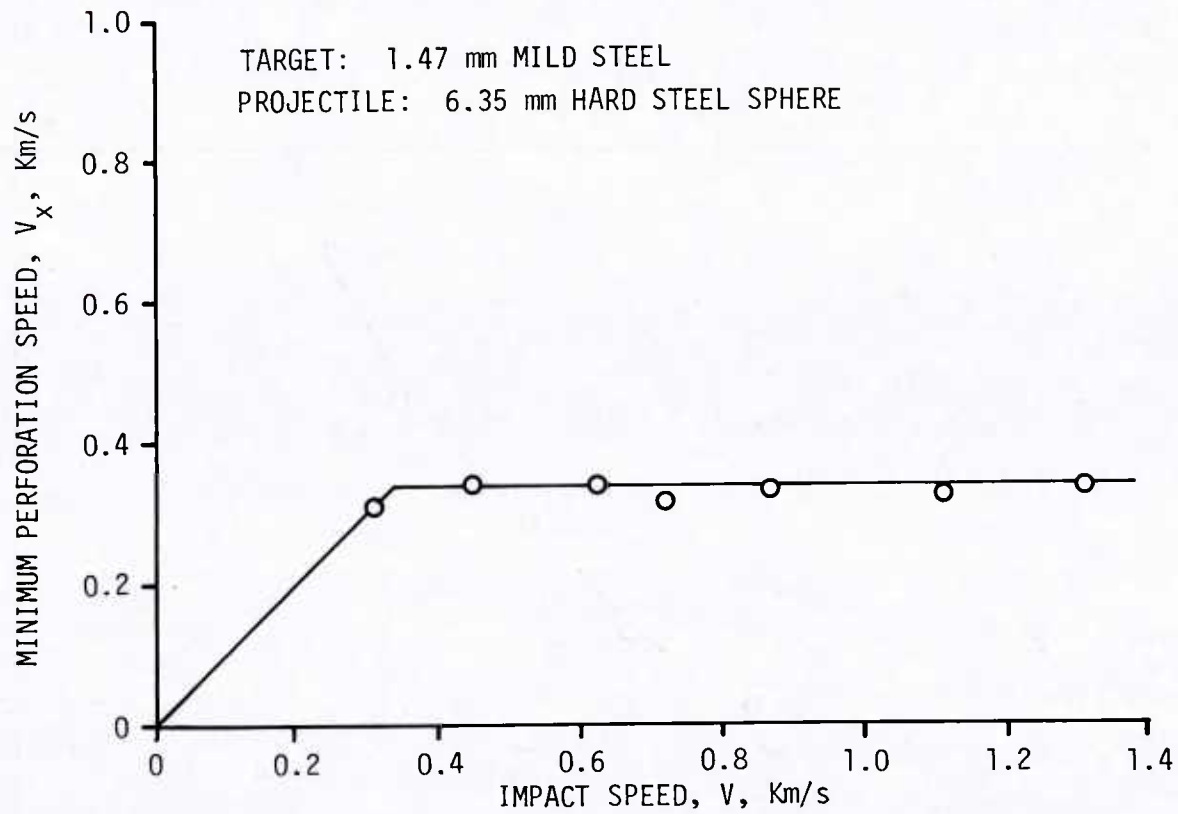


FIGURE 26. Minimum Perforation Speed as a Function of Impact Speed.
(Hard steel sphere, mild steel plate, $T/d = 0.25$.)

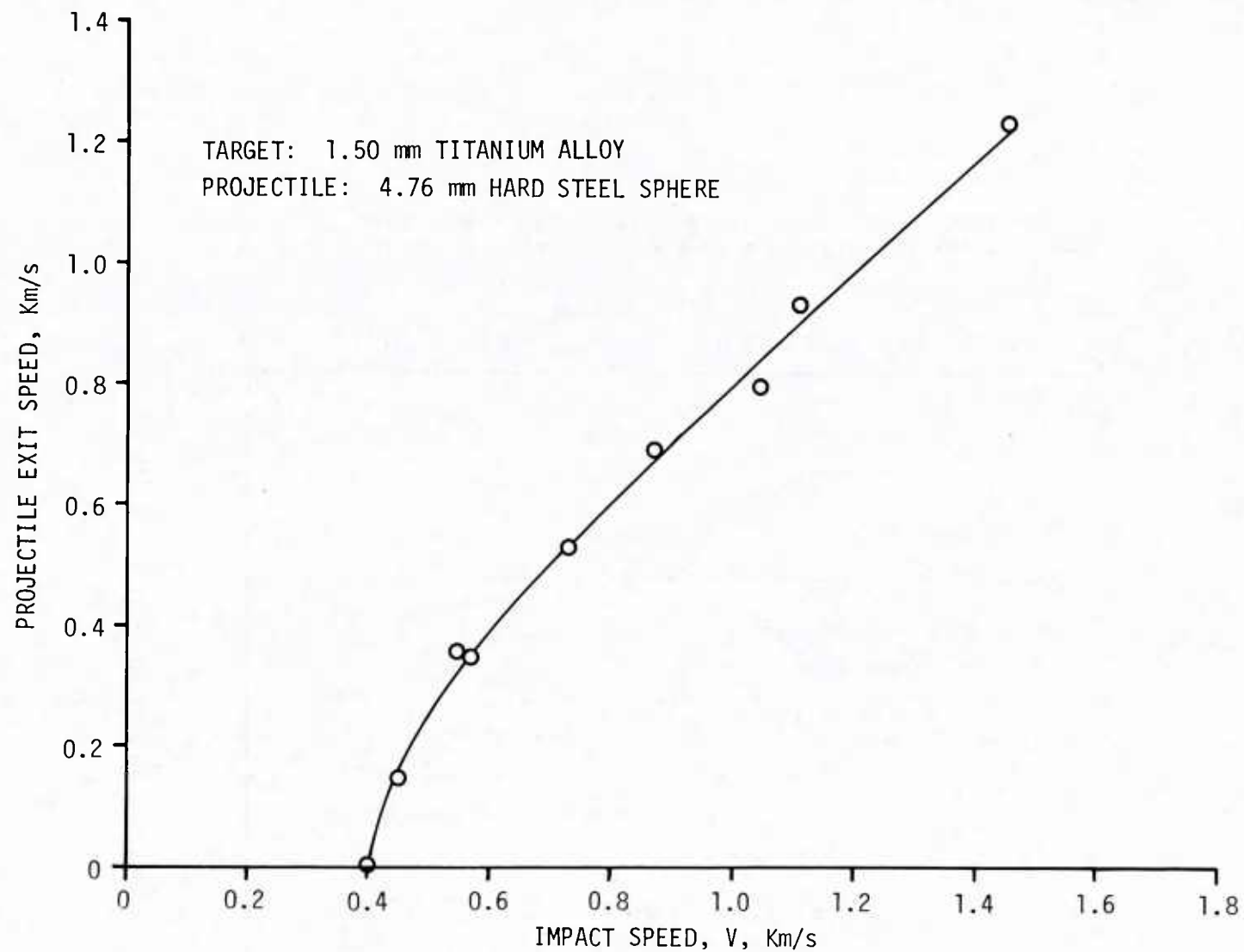


FIGURE 27. Residual Speed of the Projectile as a Function of Impact Speed.
(Hard steel sphere, titanium plate, $T/d = 0.3$.)

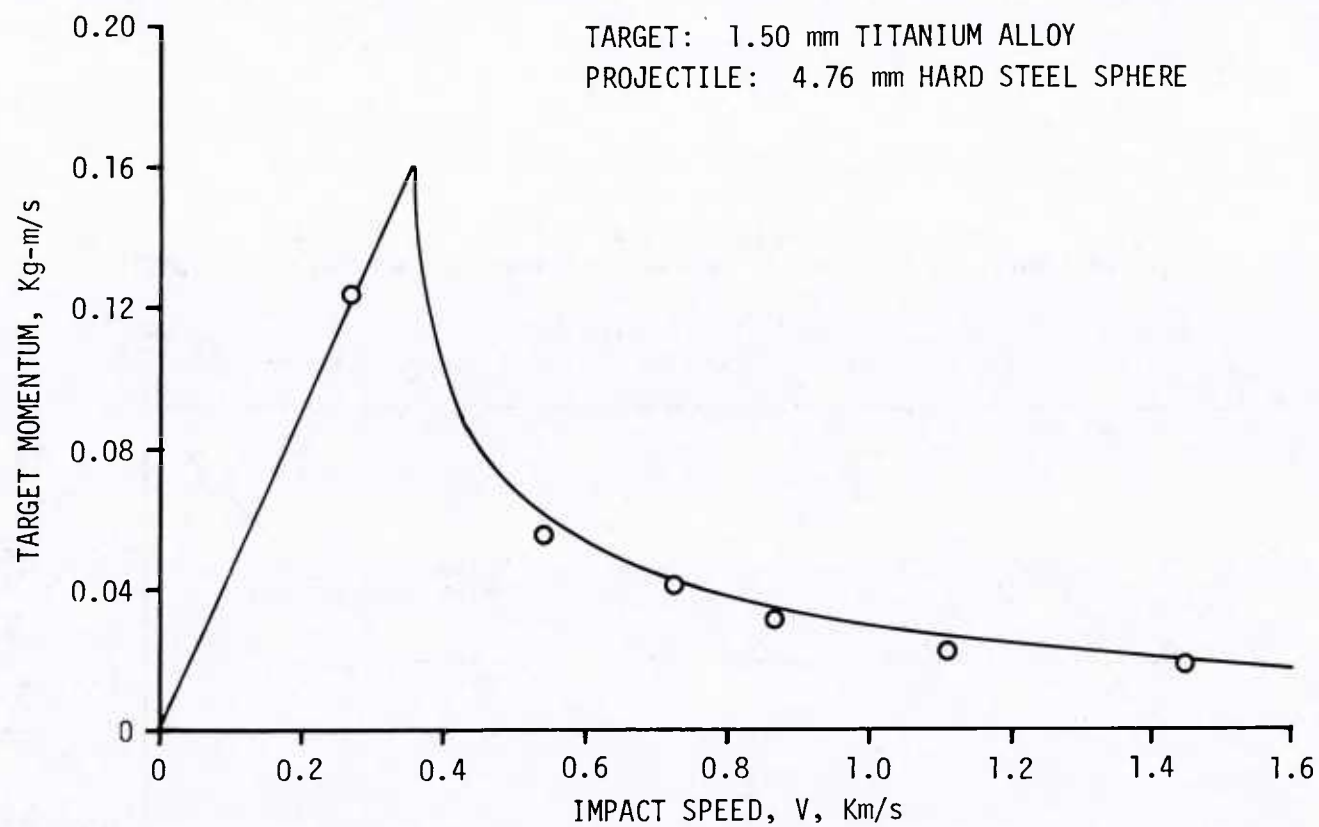


FIGURE 28. Target Momentum as a Function of Impact Speed.
(Hard steel sphere, titanium plate, $T/d = 0.3$.)

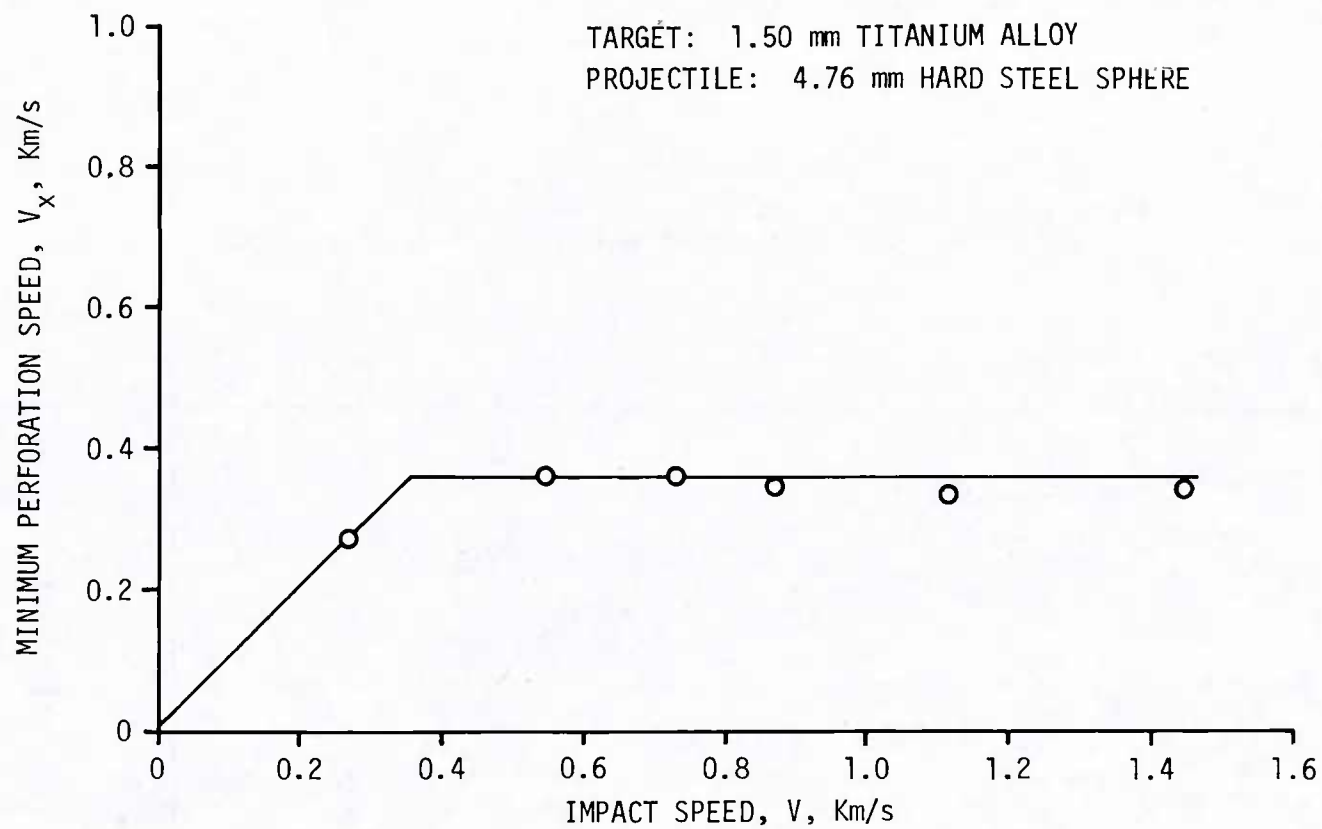


FIGURE 29. Minimum Perforation Speed as a Function of Impact Speed.
(Hard steel sphere, titanium plate, $T/d = 0.3$.)

$$V_x = V \sqrt{1 - \left[\frac{\left(1 - \frac{L}{m_p V}\right)^2}{\left(\frac{m'_p + m_q}{m_p + m_q}\right)} \right]} \quad (7)$$

where m'_p is the projectile mass after the perforation.¹²

This equation comes from a momentum balance that presumes projectile deformation and allows mass loss. If the fragment spray from the front of the plate involves significant momentum this must be included in the momentum balance and

$$L = L^* - L_f \quad (8)$$

where L^* is the ballistic pendulum measurement and L_f is the backsplash momentum.

Figure 30 presents a plot of V_x against impact speed for the impact of mild steel spheres against mild steel targets with $T/d = 1$. Near the ballistic limit V_x increases as V increases. This proves consistent with the behavior of metals reported¹² and has the interpretation that the deformation of the projectile increases the energy required to separate the plug from the target. The decreases in V_x at higher speeds coincide with the speed at which peripheral fragments form. From the location and nature of these fragmentation processes it seems highly doubtful that these could reduce the energy required for plug separation. An alternative explanation is that the peripheral fragments derive their momentum from the plate and thus make the measurement of L^* inaccurate. If one accepts this hypothesis and corrects the measured momentum for both backspray and the peripheral fragments the values of V_x continue the trend of the lower speed regime. This then corroborates the hypothesis of a new mechanism that involves momentum already transferred to the plate.

In the above observations the lamellar microstructure of the material appears to control the direction of at least part of the fragmentation process. A change of material to SAE 4130 barstock allows a comparison to a material whose lamellar structure runs across the plate rather than parallel to it. Impacts against this material do in

¹²Ipson, T. and R. F. Recht. "Ballistic Penetration Resistance and Its Measurement," *Experimental Mechanics*, Vol. 15, No. 7, July 1975.

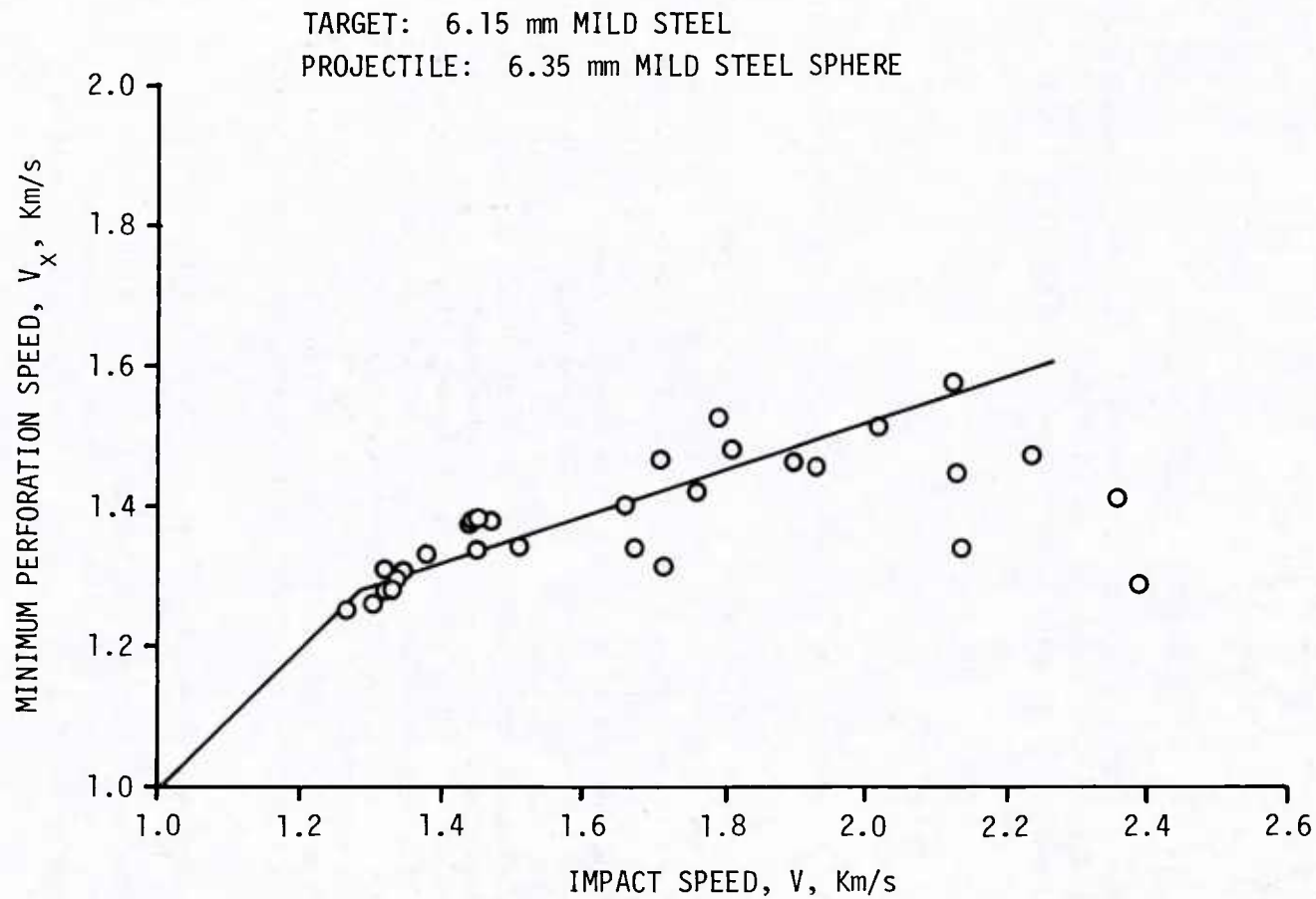


FIGURE 30. Minimum Perforation Speed as a Function of Impact Speed.
(Mild steel sphere, mild steel plate, $T/d = 1$.)

fact produce craters without rings at any impact speed in the range of this investigation. Control by those planes of weakness implies that if peripheral fragmentation occurs it involves a process similar to that which formed the plug, *i.e.*, fragmentation associated with inhomogeneous shear, and which follows members of the same family of slip surfaces (the inward directed ones). This process would result in separation of sleeve-like pieces from the plate. An example of an unbroken sleeve is shown in Figure 31. Examples of the fractures that produce this mode of fragmentation are shown in Figure 32. In Figure 33 the points in triangle show the results of calculating V_x from ballistic pendulum measurements as outlined above. Again these calculated values of V_x begin to fall at higher impact speeds and with no other change in the performance of the system of comparable magnitude. As will be shown later, estimates of the velocities and masses of sleeves that could come off in this range of impact speeds result in the corrected estimates of V_x shown as circles. These tend to continue the trend established at lower speeds.

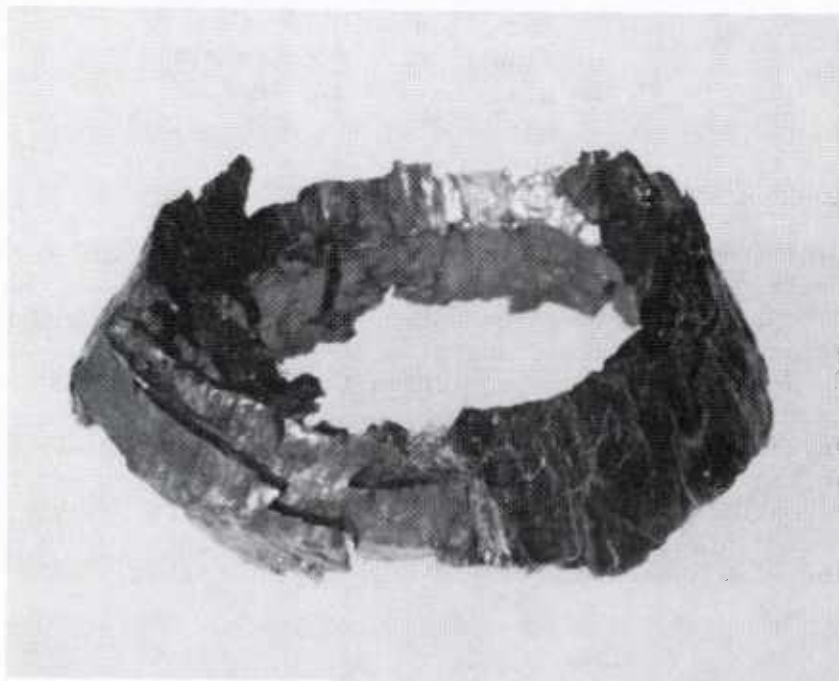


FIGURE 31. An Unbroken Sleeve. (Mild steel sphere, Soviet armor plate, $T/d = 1.$)

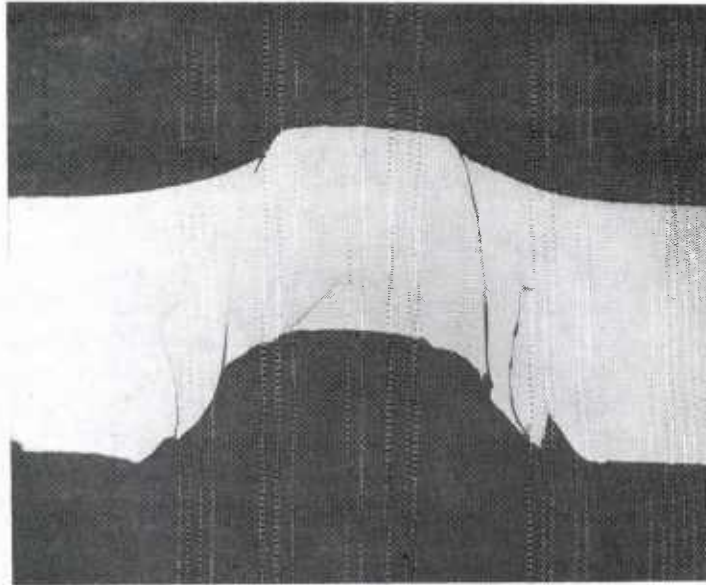


FIGURE 32. Fractures Leading to Sleeve Formation. (Mild steel sphere, 4130 steel plate, $T/d = 1$, $V = 1.2$ Km/s.

Fragmentation of the Entry Lip

An impact in the velocity range above 1 Km/s generates extremes of stress and strain that become most evident in the phenomena that occur on the entry side of the plate. The entry deformations resemble the splash of an object striking a liquid surface. The deformations severely tax the capacity of computational procedures that can be used to model the impact process.¹³ The particles that comprise the fragment system have very small sizes and their velocities are as much as an order of magnitude greater than the impact velocities. This fragment system often produces intense luminosities making it difficult to observe the initial stages of the impact. In general, the forms of failure operative in the region belong to the list generated for the rest of the target.

¹³Dienes, J. K. and J. M. Walsh. "Theory of Impact: Some General Principles and the Method of Eulerian Codes," in *High-Velocity Impact Phenomena*, Chapter III, Ed. by Ray Kinslow. New York and London, Academic Press, 1970, pp. 45-104.

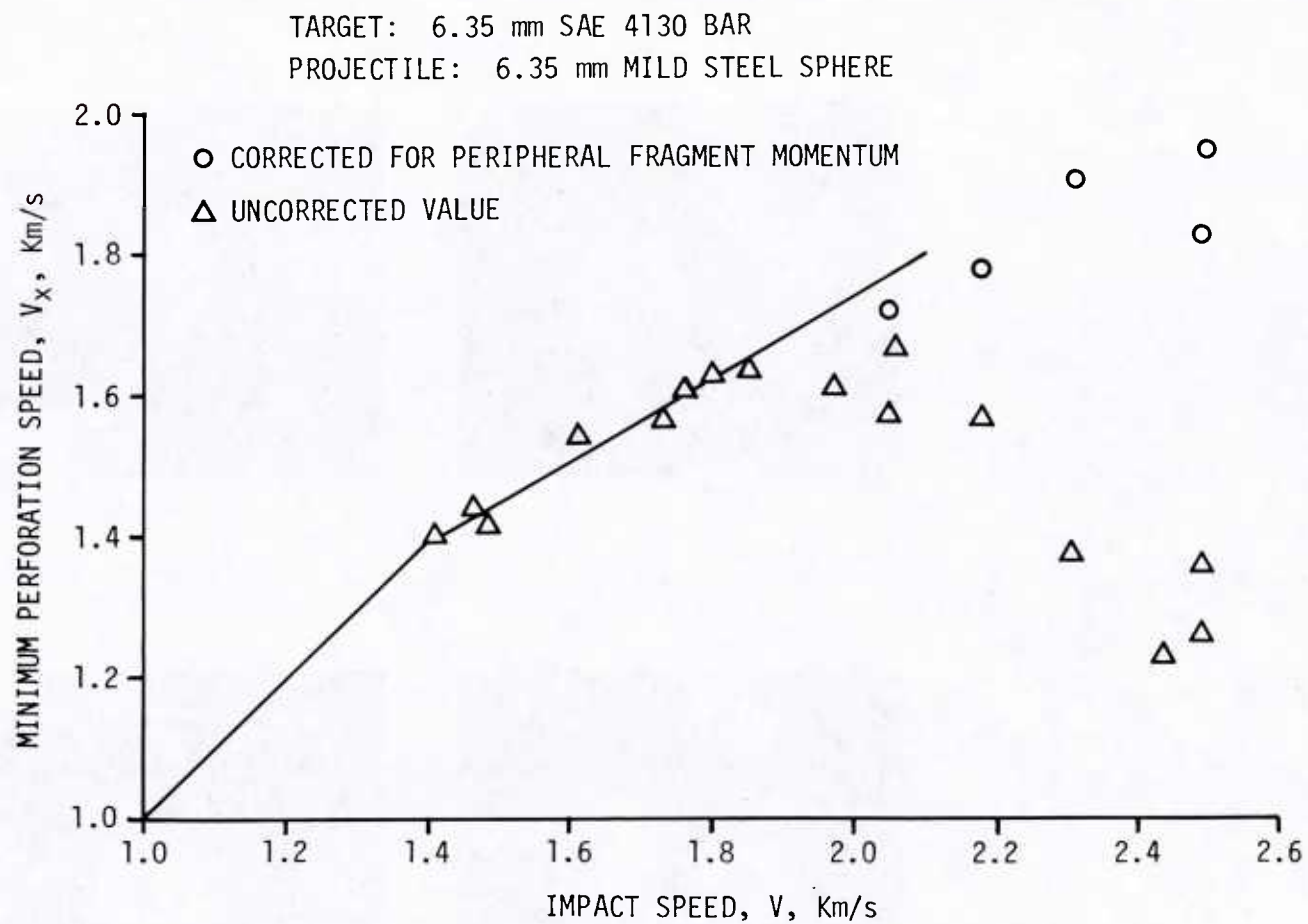
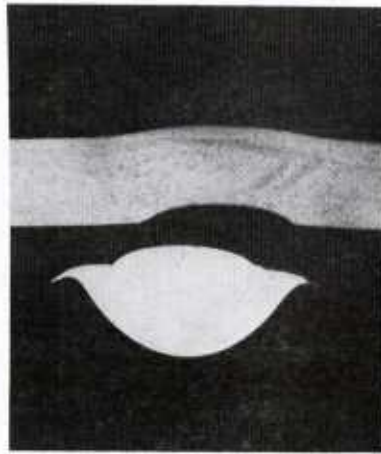


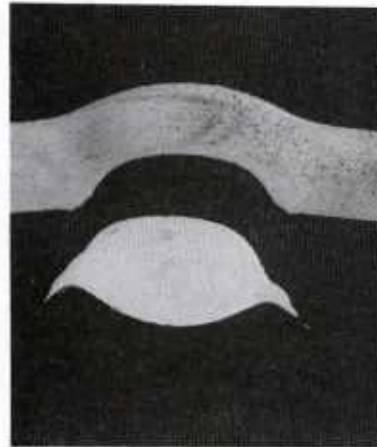
FIGURE 33. Minimum Perforation Speed as a Function of Impact Speed.
(Mild steel sphere, 4130 steel bar, $T/d = 1.$)

Fragmentation of the Projectile

The impact of the sphere against the plate causes a squashing deformation of the sphere, *i.e.*, the impact loads on the contact surface compress the sphere in the direction of motion while the stress free surfaces to the sides allow the sphere to expand laterally. In the range of impact speeds for which the internal stresses are elastic this squashing consists of the distortion of the original spherical shape to oblate spheroidal. Above the elastic range the same tendencies continue but are drastically modified by the marked increases in the amount of deformation corresponding to increases in internal stress and the marked decrease in the rate at which stress conditions travel throughout the body. These changes increase the amount of squashing and make it take place closer to the contact surface. Figure 34 shows these changes of the deformation of the sphere as impact speed increases.



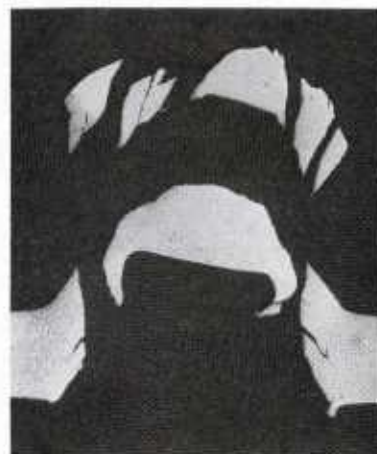
0.5 Km/s



0.8 Km/s



1.1 Km/s



1.5 Km/s

FIGURE 34. Successive Deformations of a Sphere. (Mild steel sphere, U.S. armor plate, $T/d = 0.5$.)

As impact speed increases the sphere shows the same sequence of deformation mechanisms as the plate. At lower speeds the deformations are homogeneous plastic deformations and increased impact speed eventually leads to inhomogeneous plastic deformation and fracture. As in the plate these latter failures tend to travel along trajectories of maximum shear (slip surfaces). Figure 35 shows a schematic representation of these failure patterns. The piece in the center of this pattern has a vaguely conical shape and is found in virtually all groups of recovered fragments. The remaining projectile fragments come from radially directed cross fractures that breakup the flanged sections around the central fragment. Thus the failure processes in the projectile prove identical to those in the plate and consist of (1) shear-band fractures, (2) cross fractures and (3) at very high speeds may include spalls.

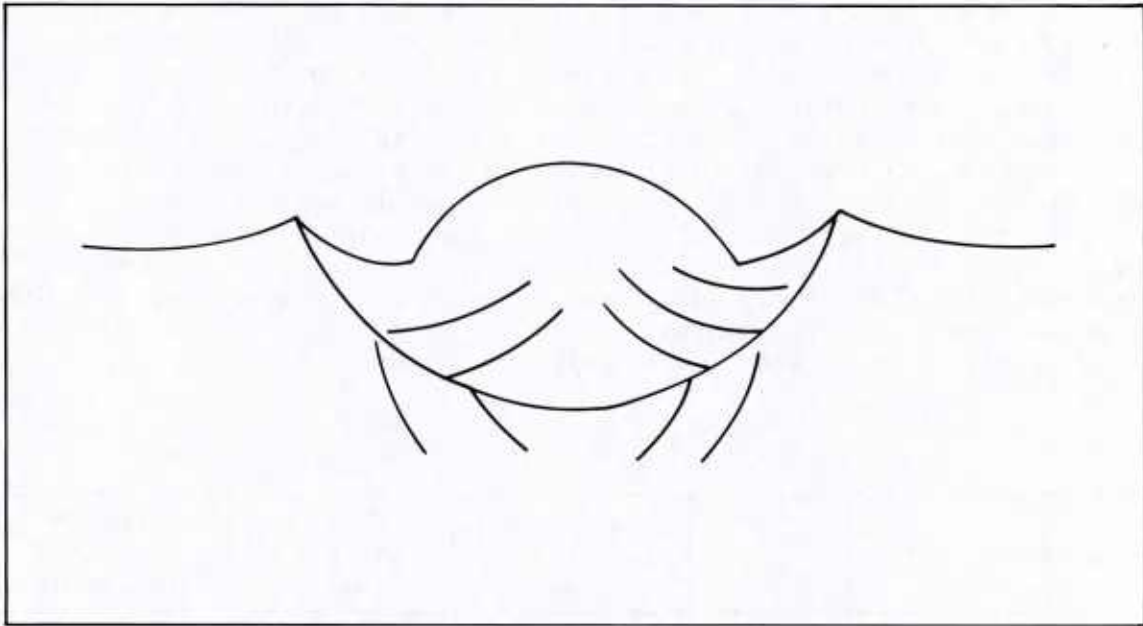


FIGURE 35. Schematic Fracture Patterns for a Spherical Projectile.

FRAGMENTATION PROCESSES IN REPRESENTATIVE IMPACT SYSTEMS

A SUMMARY OF THE SYSTEMS

Ten impact systems have been investigated in sufficient detail to reach conclusions on the dependence of the fragmentation processes on material and configurational parameters. Table 1 presents the main features of the systems divided into six groups. The first group contains two systems consisting of mild steel plates with $T/d \approx 1$ and $T/d \approx 0.25$. These comprise convenient base systems for the following discussion because the material response has the least complexities. They also exhibit no peripheral fragmentation over a large part of the impact speed range of interest so that it becomes particularly easy to characterize the exit fragment systems. The second group contains three thicknesses of U.S. armoring material that exhibits ring-type peripheral fragmentation for which it proves easy to establish the existence of a peripheral source of fragmentation and to estimate the amount of peripheral material. The third group contains a single system, SAE 4130 with $T/d \approx 1$, a material that exhibits the sleeve-type peripheral fragmentation and demonstrates the problems in establishing the amount of peripheral fragmenting material for this type of peripheral fragmentation. The fourth group contains a single system, a Soviet armoring material, $T/d \approx 1$, that exhibits a mixture of ring and sleeve types of peripheral fragmentation. The fifth and sixth groups contain two systems for which a small amount of data permits a limited comparison of the preceding ferrous alloys to an aluminum and titanium alloy.

TABLE 1. Impact Systems of This Investigation.

Plate material	Proj. shape	Projectile dimension (mm)	Plate thickness (mm)	Mode of peripheral fragmentation
Mild steel (low carbon)	Sphere	6.35	6.15	None
	Sphere	6.35	1.47	None
U.S. armor	Sphere	6.35	6.55	Ring
	Sphere	6.35	3.43	Ring
	Sphere	6.35	1.52	Ring
	Cube	5.13	6.55	Ring
SAE 4130 barstock	Sphere	6.35	6.35	Sleeve
Soviet armor	Sphere	6.35	6.35	Mixed
2024-T4 Al	Sphere	6.35	6.35	Ring
Ti-8Al-1Mo-1V	Sphere	4.76	1.50	Ring

COMPARISON OF FRAGMENTATION IN TARGETS OF THREE STEELS AND $T/d = 1$

Table 2 lists the metallurgical and mechanical properties of the target and projectile materials of the present studies. Among these materials the mild steel, U. S. armor and Soviet armor comprise a set of steel alloys with significant differences in strength, ductility, and microstructure. These differences allow a comparison of the characteristics of fragmentation among materials with the same density and general composition but a range of other properties. The choice of $T/d = 1$ resulted primarily from the availability of a considerable amount of data on this configuration. The value $T/d = 1$ has the advantage that it puts the impact conditions for perforation in a range of impact speeds of direct interest to ordnance research and design and turns out to be representative of the phenomenological complexities of practical problems. The materials serve well to illustrate the variations in fragmentation characteristics that one type of material can exhibit.

Crater Development

The differences in the mechanical properties of the three steels result in corresponding differences in the development of impact craters with increasing impact velocity as shown in Figures 6, 36 and 37, which present the measures of mean strain ϵ_1 and ϵ_2 as functions of impact speed. The slopes of these curves show the least resistance to deformation for mild steel and increasing resistance for U.S. armor and still greater resistance for Soviet armor. The ballistic limit data show that the more resistant Soviet armor permits perforation at about the same speed as mild steel and at a far lower speed than the U.S. armor.

Figures 3, 38 and 39 show the speed of the lead fragment among the system of fragments that emerge after perforation for these same three steels. These show that the overall trend in this measure of residual speed tends to correlate with the resistance to crater formation (*i.e.*, with the slopes of the curves of Figures 36 and 37) more than with the speed for the completion of perforation failure (*i.e.*, the points on Figures 36 and 37 at which a fragment first separates from the plate).

Comparison of the Size of the Central Region for the Three Steels

Two methods have provided estimates of the mass of the central region of fragmentation, m_q . In one method, Celotex bundles or wax blocks collect the fragments from the exit side and a skilled operator makes a fragment-by-fragment decision on the source of the fragments. This method proves to be reasonably accurate and effective for a small number of fragments of reasonable size and for materials that display a ring-mode of peripheral fragmentation. For example, firings against the U.S. armor

TABLE 2. Physical Properties of Target and Projectile Materials.

Material	Dimension (mm)	Hardness (Bhn)	Approximate tensile strength (psi)	Heat treatment	Primary microstructure
Target					
Low carbon steel	6.15	116	58,000	Hot rolled	Ferrite/lamellar pearlite
Low carbon steel	1.47	91	45,000	Hot rolled	Ferrite/lamellar pearlite
U.S. armor*	6.55, 3.43 1.52	372	182,000	Quench and temper	Tempered martensite
Soviet armor*	6.35	382-448	188,000- 229,000	Quench and temper	Tempered martensite plus ferrite
SAE 4130 (bar)	6.35	352	171,000	Quench and temper	Tempered martensite
2024-T4 aluminum	6.35	120	70,000		
Ti-8Al-1Mo-1V	1.50	290	140,000		Widmanstätten α and equiaxed primary α
Projectile					
Low carbon steel	6.35, 5.13	160	91,000		
2024-T4 aluminum	6.35	120	70,000		
AISI 52100 steel	6.35, 4.76	700			

*Chemical analysis (%)

U.S. armor - 0.51C, 0.54Mn, 0.41Si, 1.3Cr, 0.24Ni, 0.41Mo, 0.29V.

Soviet armor - 0.22C, 1.19Mn, 1.25Si, 0.92Cr, 1.0Ni, 0.16Mo.

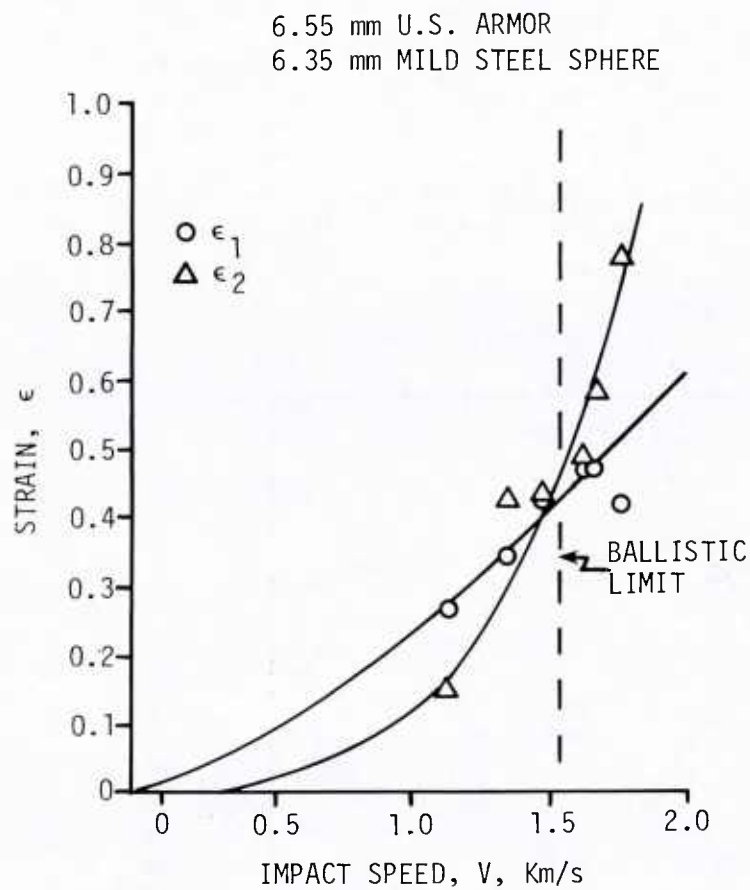


FIGURE 36. Mean-Strains as a Function of Impact Speed. (Mild steel sphere, U.S. armor plate, $T/d = 1.$)

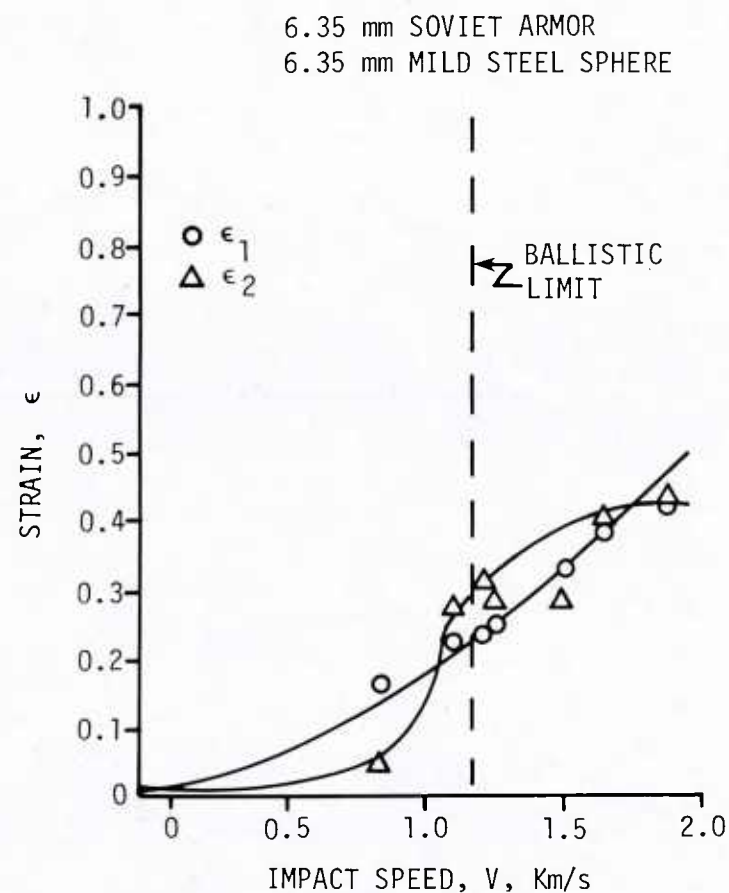


FIGURE 37. Mean-Strains as a Function of Impact Speed. (Mild steel sphere, Soviet armor plate, $T/d = 1.$)

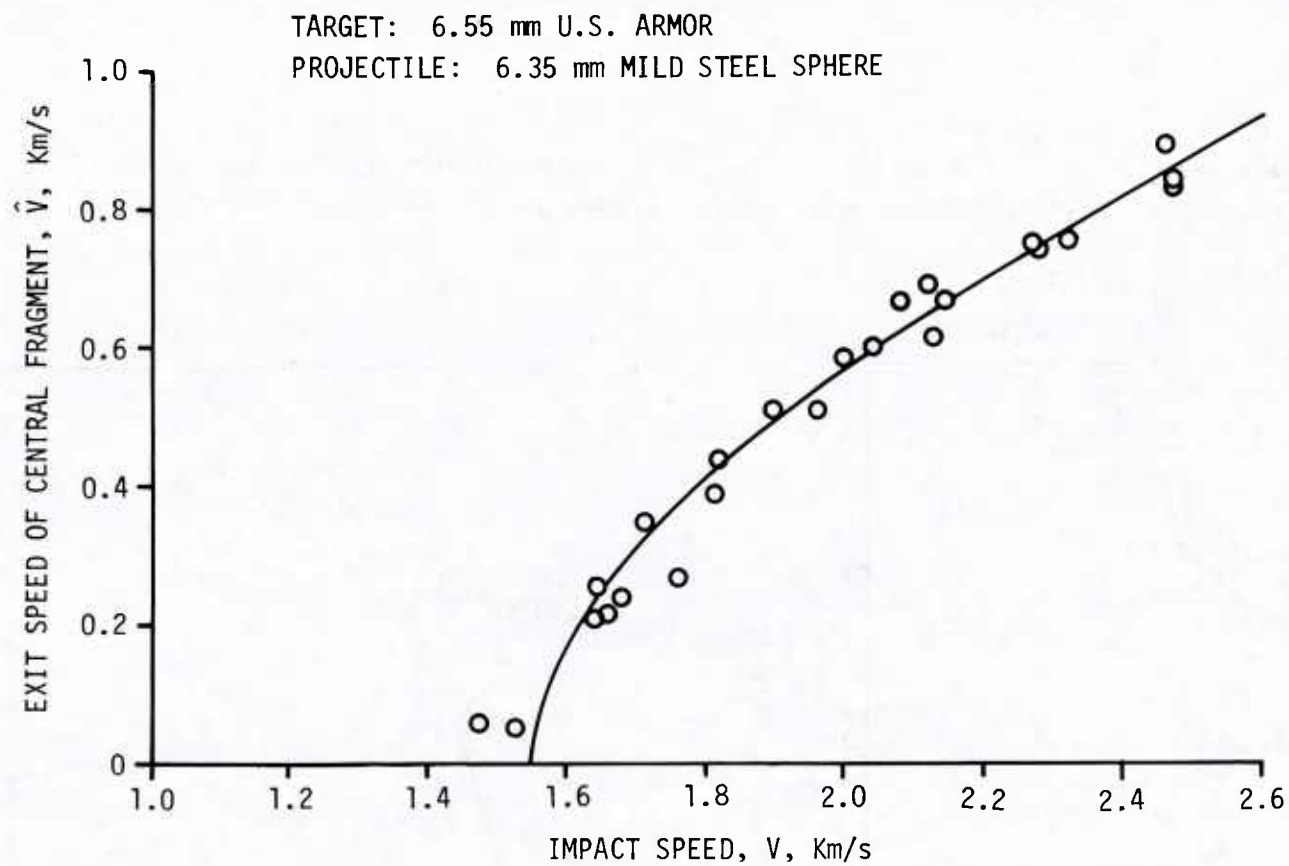


FIGURE 38. Residual Speed of the Lead Fragment as a Function of Impact Speed. (Mild steel sphere, U.S. armor plate, $T/d = 1.$)

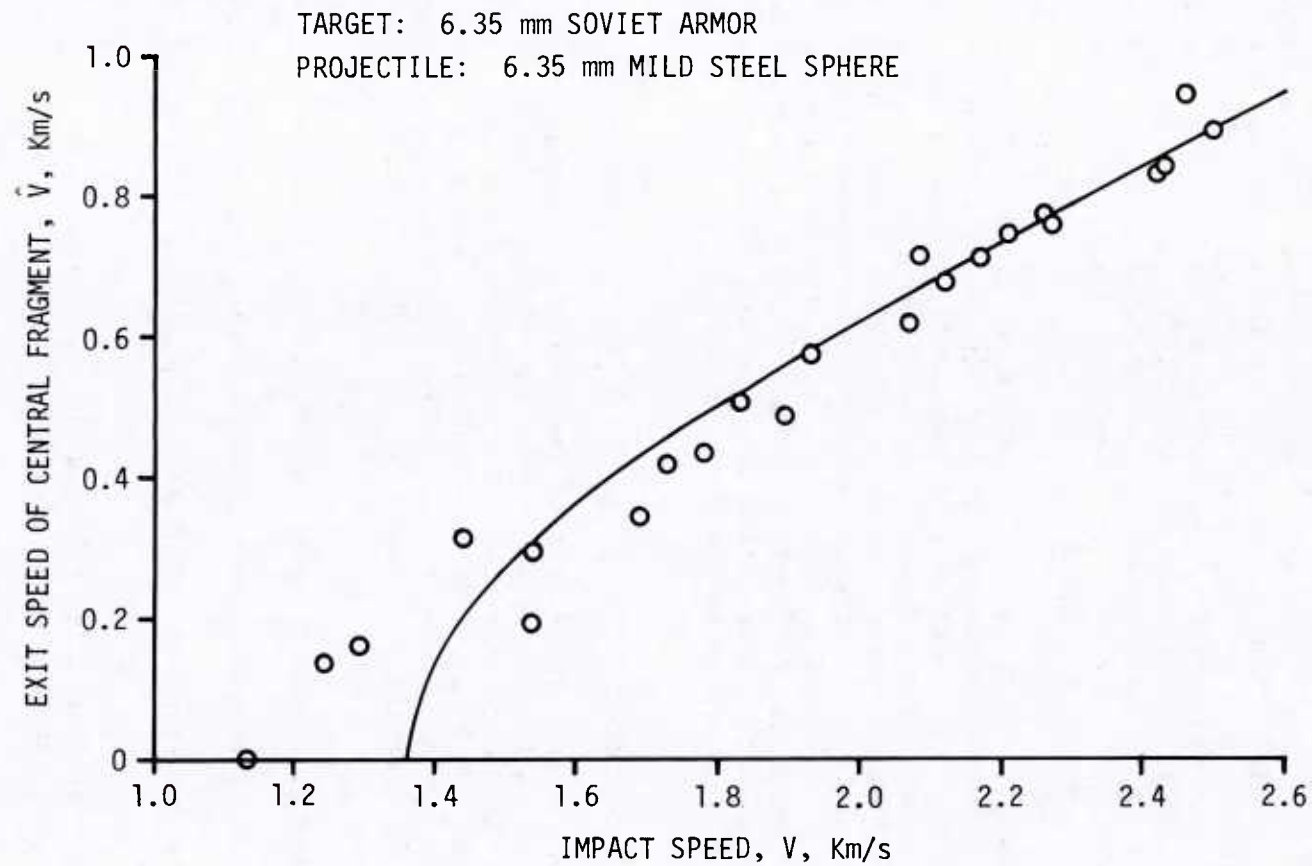


FIGURE 39. Residual Speed of the Lead Fragment as a Function of Impact Speed. (Mild steel sphere, Soviet armor plate, $T/d = 1$.)

and the Soviet armor with $T/d = 1$ and at impact speeds up to 2.0 Km/s result in a fragment system in which virtually all of the major fragments have identifiable source regions. The other method involves measurement of the total mass m_T from the plate by the difference in weight before and after firing, and subtracting an estimate of the mass ejected from the front side of the plate m_f derived from measurements of average speed and measurements of total momentum. One measures the average speed by determining the displacement of the tip of the entry splash for known time intervals between frames of the record from a Kerr cell camera and the total momentum of the entry splash by a ballistic pendulum with a small aperture for the initial passage of the impacting sphere. This method has been applied to the mild steel system in the range of impact speeds in which no peripheral fragmentation occurs.

Figure 40 shows all of these data for the three steels. The data have considerable scatter that we believe comes from considerable variability in the failure processes plus comparable or large errors in the measurement schemes. These data indicate a decrease in the size of the central region with increasing impact speed. It is impossible to use these data to make a definitive statement on the comparative size of the region for the three steels; however, the three steels appear to have about the same size central regions. This implies that despite the differences in the extent of deformation at the moment of plug separation the central regions have approximately the same size.

Fragmentation of the Central Region

The collected fragments provide data that measure the extent of fragmentation of any of the source regions by the number of fragments from each region. In addition one can count the number of holes in either the outer surface of the Celotex recovery bundle or in a sheet of paper placed on the outer surface of the bundle to give an independent estimate of the total number of fragments. Thus, the final data consist of the following:

- n_p the number of fragments identified as pieces of the projectile
- n_q the number of fragments identified as pieces of the central region
- n_y the number of fragments identified as pieces of the peripheral region
- n_x the number of fragments collected but that do not have recognizable features of any region

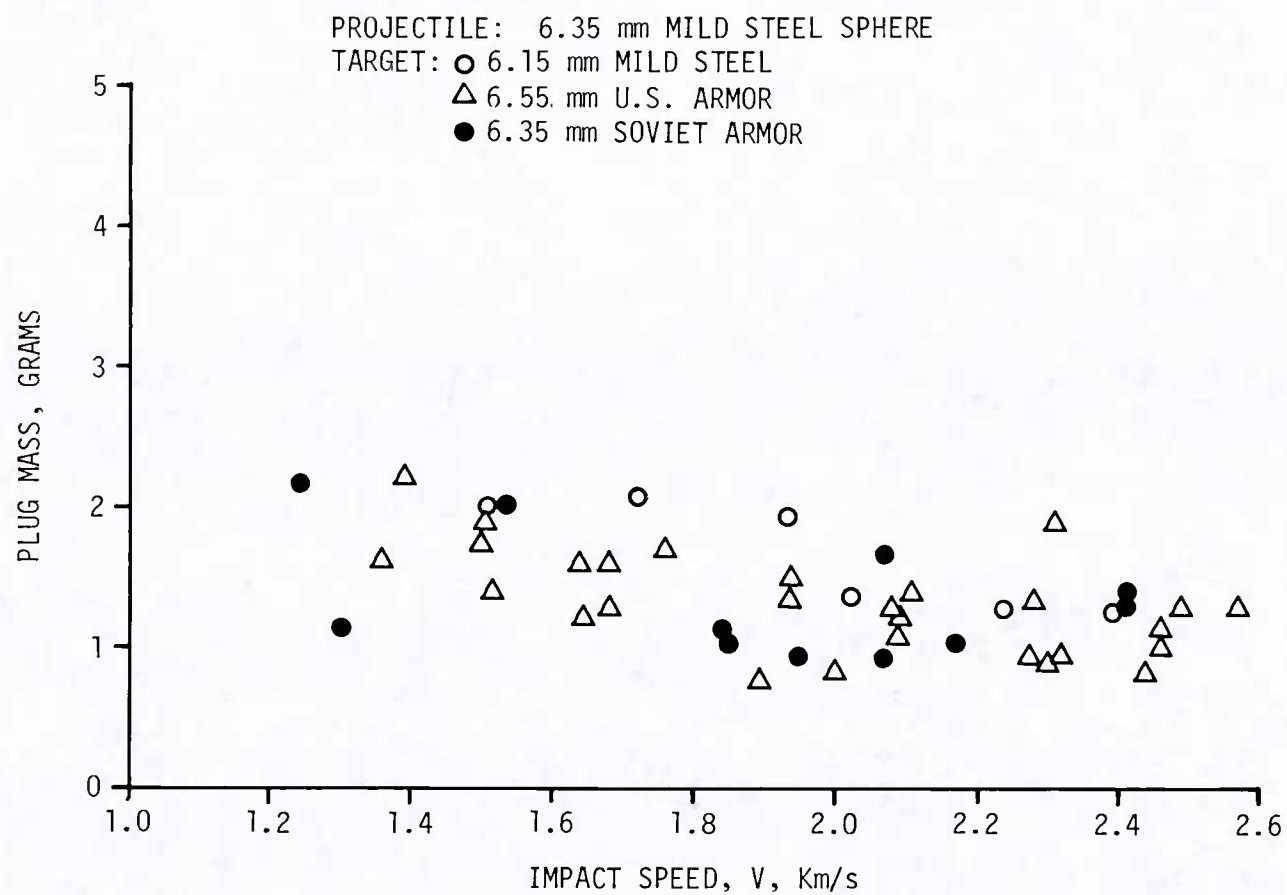


FIGURE 40. Mass of the Central Region as a Function of Impact Speed.
 (Mild steel sphere, U.S. and Soviet armor plate,
 $T/d = 1.$)

N the total number of fragments from counts of holes in a paper layer

N* the total number of fragments from counts of holes in a Celotex layer

The total number of collected fragments $n_p + n_q + n_y + n_x$ turns out less than either N* or N. The numbers N consistently have the larger values than N* and apparently have the greater accuracy. For one thing the texture of the Celotex surface tends to obscure small holes more than the paper layer.

In order to estimate the number of fragments from each source region we adjusted the number of identifiable fragments from a given source region n_i by adding to it the observed percentage of unidentifiable fragments and then using the resulting adjusted counts of collected fragments to determine the percentage of the total number of fragments that belong to that source region. For example the estimated number of fragments from the central region N_q^* for a total count N* based on holes in the first Celotex layer becomes

$$N_q^* = \left[\frac{n_q + n_x \left(\frac{n_q}{n_p + n_q + n_y} \right)}{n_q + n_p + n_y + n_x} \right] N^* \quad (9)$$

Figure 19 presented these data on the number of fragments from the central region for targets of mild steel. Figure 41 compares these data to data on the U.S. armor alloy and the Soviet armor alloy. These data on the three materials exhibit the same trends as the measures of mean plastic strain, Figure 6, 36 and 37, and thus suggest a correlation of the extent of fragmentation at a given impact speed to the amount of plastic strain at that impact speed.

Fragmentation on the Entry Side

The fragmentation on the entry side of the plate belongs to a complicated kind of splashing process. Fragments formed early in the process have small sizes, make up a comparatively minor part of the total fragmented mass, and tend to have extremely high speeds. Fragments formed later are larger and slower. The whole fragment system has an important role in the interaction with structures at very high impact speeds because of its contribution to the momentum of the target. Measurements of momentum which serve to interpret the dynamics of impact require one to account for the momentum of the entry side splash.

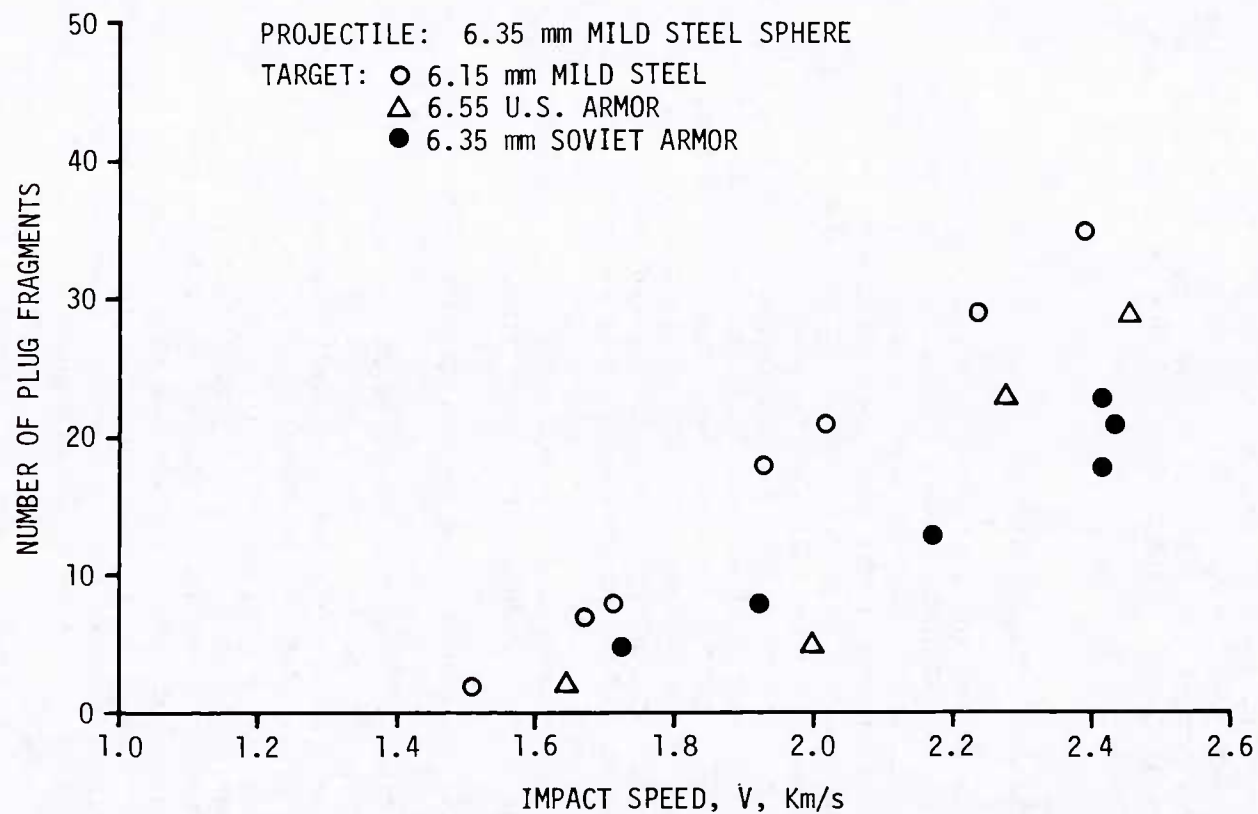


FIGURE 41. Number of Fragments from the Central Region as a Function of Impact Speed for Mild Steel, a U.S. Armor and a Soviet Armor ($T/d = 1$).

A special ballistic pendulum serves to measure this back splash momentum. This pendulum uses Celotex sheets as the momentum collector. These sheets have a hole that permits the projectile to pass through the collector but the entry fragment system forms a hollow cone that strikes the collector. In general a separate set of measurements determines the behavior of this system. Figure 42 shows an example of measurements for mild steel plate with $T/d = 1$. Other examples of this type of measurement will accompany measurements of the momentum transferred to a given kind of target. These constitute an essential part of the interpretation of such momentum measurements.

Evidence for a Distinct Peripheral Region

Experimental evidence for the existence of a peripheral region of fragmentation was presented in the previous section for the impact of mild steel spheres against mild steel plates. The evidence consisted of the simultaneous development of changes in the exit side of the perforation craters and changes in the values of V_x computed from measurements of momentum. Firings against U.S. armor provide even more readily observable examples of peripheral fragmentation and will be discussed before a more detailed discussion of the mild steel. At velocities a few hundred meters per second above the ballistic limit well defined cavities develop on the exit side of the perforation crater. (Figure 21 has shown the internal fractures that caused these cavities.) Thus observations on crater shape alone suggest that the mechanism that forms the ring-shaped contributions to the craters and the mechanism of perforation operate independently and for mild steel this suggestion receives further support from measurements of momentum.

The characteristic shape of the peripheral fragments from the armor-ing material make it comparatively easy to identify the recovered fragments that belong to the peripheral region. Figure 43 presents a plot of the total mass of these fragments against impact speed. High speed photography (using a Kerr cell camera) reveals the distribution of these fragments in space at known times and thus permits measurements of the speeds of the individual fragments. Figure 44 shows an example of the fragment patterns observed in this way. The group of large fragments close to the plate comprise a consistent feature of such records and suggest the identification of these fragments as ring fragments. Assuming that these fragments do come from the peripheral region, the average speed of these fragments becomes a measure of the average speed of fragments from the peripheral regions. Figure 45 shows measurements of the average speed of peripheral fragments as a function of impact speed. (These data actually include the results from firings with both spheres and cubes. In most respects these systems perform alike and the inclusion of the cube data expands the amount of available data.) Linear fits to these data appear to describe the significant trends and therefore provide an estimate of the momentum in the ring system. Hence, for

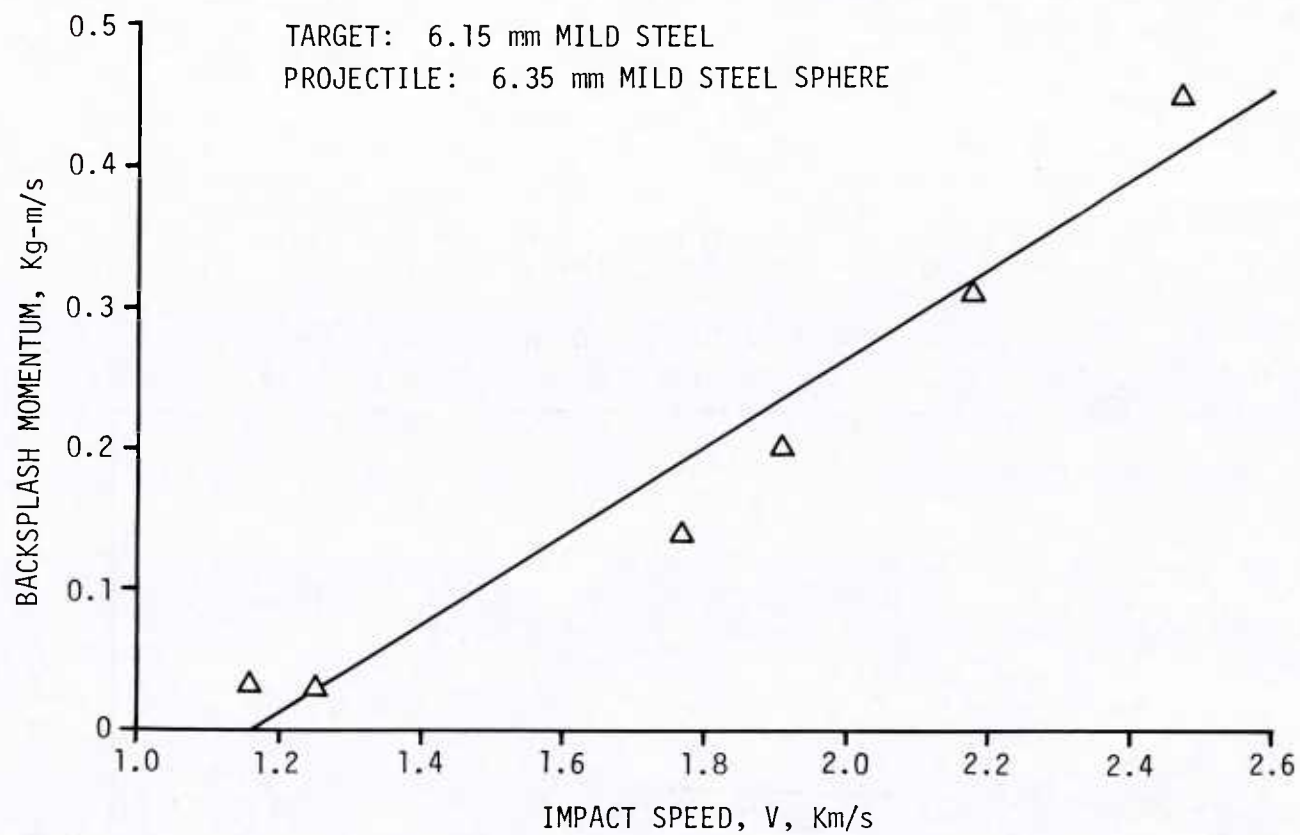


FIGURE 42. A Typical Measurement of Backsplash Momentum as a Function of Impact Speed. (Mild steel sphere, mild steel plate, $T/d = 1.$)

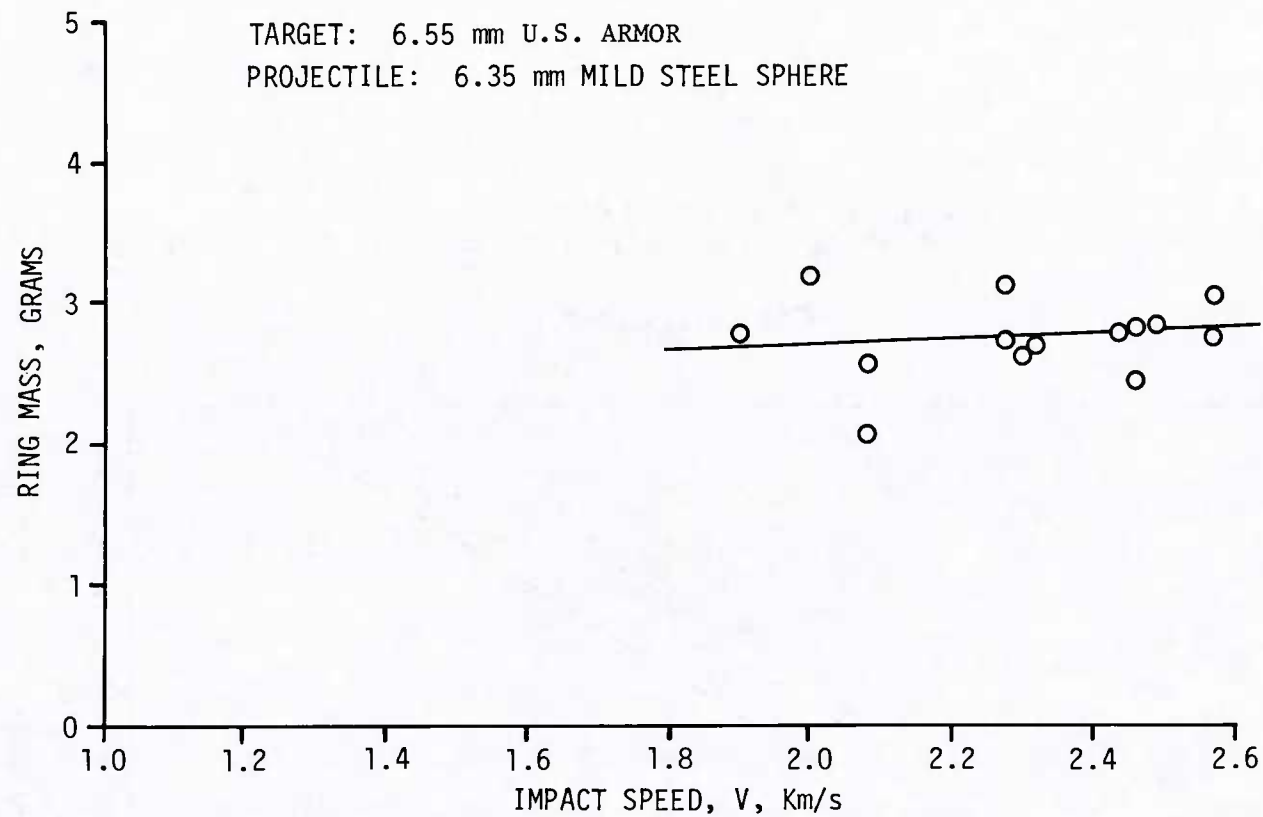


FIGURE 43. Mass of the Ring-Mode Peripheral Region as a Function of Impact Speed. (Mild steel sphere, U.S. armor plate, $T/d = 1.0$.)

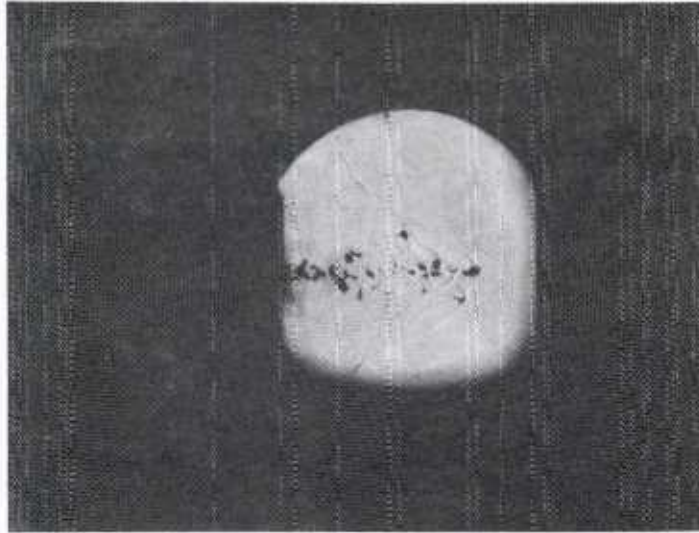


FIGURE 44. Photograph of a Fragment Pattern for a U.S. Armor ($V = 2.3 \text{ Km/s}$, $T/d = 1$).

$$V_y = V_{yc} + \alpha(V - V_{yo}) \quad (10)$$

and

$$m_y = m_{yc} + \beta(V - V_{yo}) \quad (11)$$

the momentum becomes

$$L_y = V_{yc} m_{yo} + (\beta V_{yo} + \alpha m_{yo}) (V - V_{yo}) + \alpha \beta (V - V_{yo})^2 \quad (12)$$

The following considerations of the conservation of momentum suggest that the peripheral fragments derive their momentum from that transferred to the plate during the perforation process. The calculation of the momentum transferred to the plate L from ballistic pendulum measurements L^* and the backsplash momentum L_f , Equation 8, when used in Equation 7 provide a calculation of V_x , the minimum perforation velocity (Footnote 12).

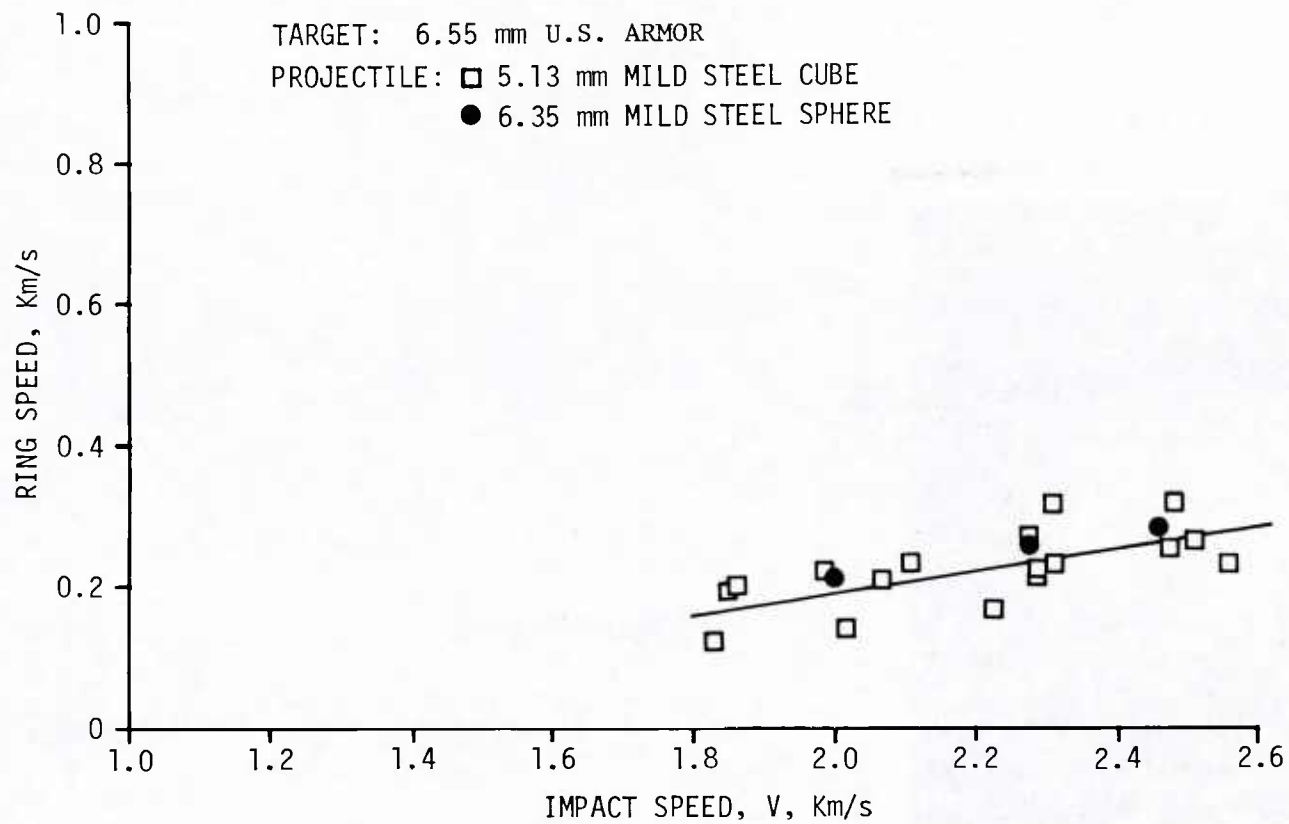


FIGURE 45. Average Speed of Ring Fragments as a Function of Impact Speed. (Mild steel projectiles, U.S. armor plate, $T/d = 1.$)

Figure 46 presents these calculations for the data on the U.S. armor as triangles. The experimental points from the ballistic limit to about 1.8 Km/s correspond to impacts without peripheral fragmentation. The increase in minimum perforation velocity with impact speed, in this region, means that the minimum energy for separating a plug from the plate has increased which can be attributed to the deformation of the projectile. The points above 1.8 Km/s decrease with increasing impact speed and this should mean that the perforations require less and less energy; however, the craters continue to increase in size and the projectiles continue to increase in deformation and the new fragmentation processes require still more energy. Thus, it appears that the peripheral fragmentation has influenced the input to Equation 8. The data below 2.2 Km/s have the trend approximated by the linear-best-fit shown in Figure 46 by the solid line. Figure 47 shows the values of transferred momentum measured by the ballistic pendulum as circled points. The dotted curve represents the predictions of momentum for a plugging perforation using the equation

$$L = m_p V \left(1 - \sqrt{1 - \frac{V_x^2}{V^2}} \right) \quad (13)$$

in which the values of V_x come from the linear-best-fit to the data below 2.2 Km/s. The backsplash momentum corrects this curve to the solid curve. The measured values of momentum cluster about this prediction below 1.8 Km/s but become increasingly discrepant above this speed and consistently below the predicted values. The difference constitutes an estimate of the momentum of the peripheral system as a function of impact speed. This estimate compares closely with that obtained from fragment measurements as seen in Figure 48. Figure 48 represents two different estimates of ring momentum. The solid line represents a linear-best-fit to data from Figure 47 while the dotted line represents a linear-best-fit to data from Equation 12.

One can use the main ideas of this approach to interpret the data for mild steel. The recovered fragments for mild steel have shapes that do allow estimates of the mass of the peripheral region but the Kerr cell camera data involve so many fragments that the frame-to-frame identification of fragments proves extremely difficult. This difficulty completely precludes the identification of fragments by the region of origin and prevents a meaningful measurement of the average speed of the peripheral system. The momentum measurements below 2.0 Km/s permit an estimate of V_x as a function of V which Figure 30 has shown as the linear fit to the values of V_x . Using this expression for V_x in Equation 13 gives a prediction of the momentum transferred to the target in a plugging perforation. Figure 49, which plots momentum against impact speed, shows this prediction by the dotted curve while the correction for the measured backsplash momentum results in the solid curve. At the lower speeds the measured momenta from which it was derived fit to within the scatter

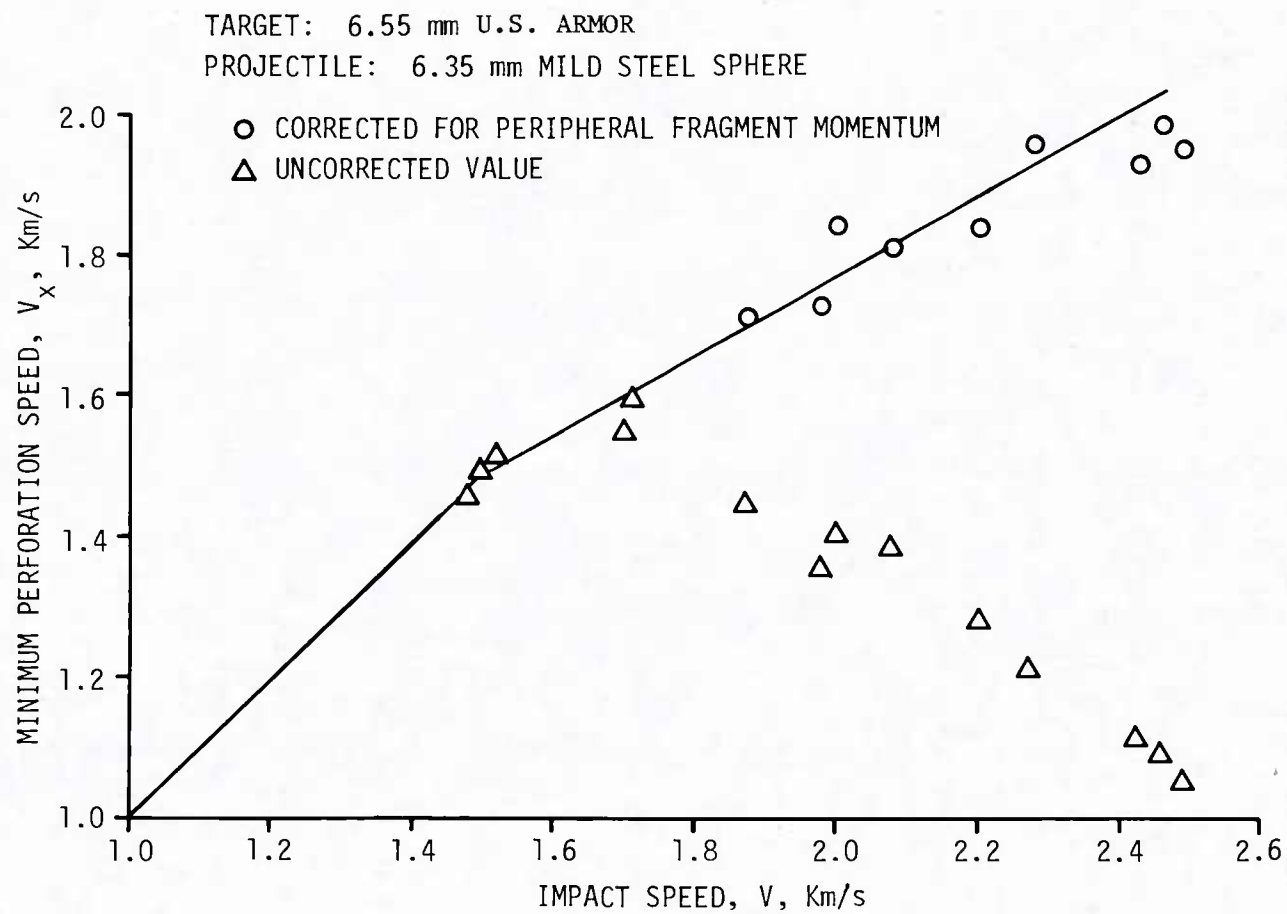


FIGURE 46. Minimum Perforation Speed as a Function of Impact Speed.
(Mild steel sphere, U.S. armor plate, $T/d = 1$.)

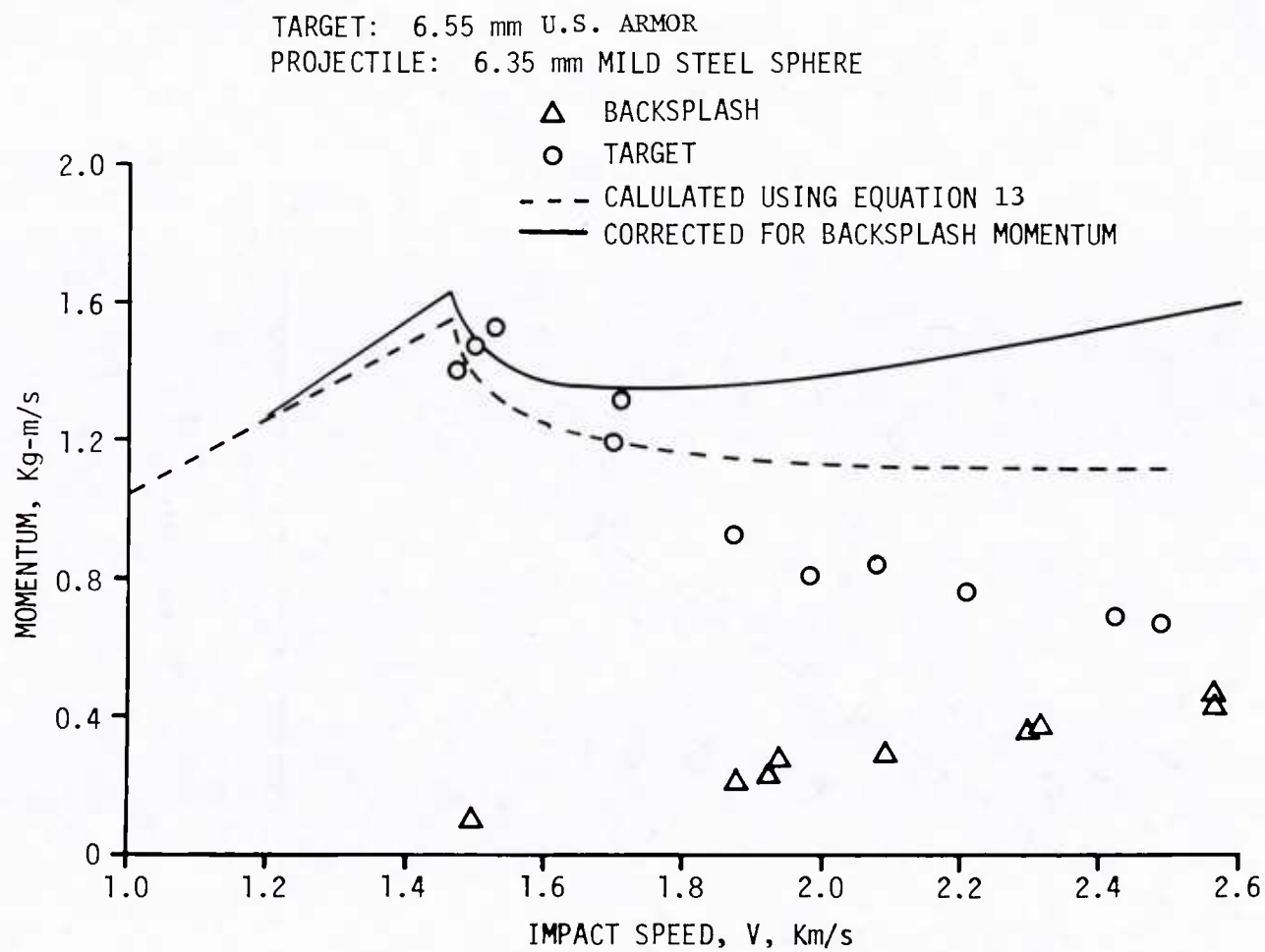


FIGURE 47. Momentum as a Function of Impact Speed.
(Mild steel sphere, U.S. armor plate,
 $T/d = 1.$)

TARGET: 6.55 mm U.S. ARMOR
PROJECTILE: 6.35 mm MILD STEEL SPHERE

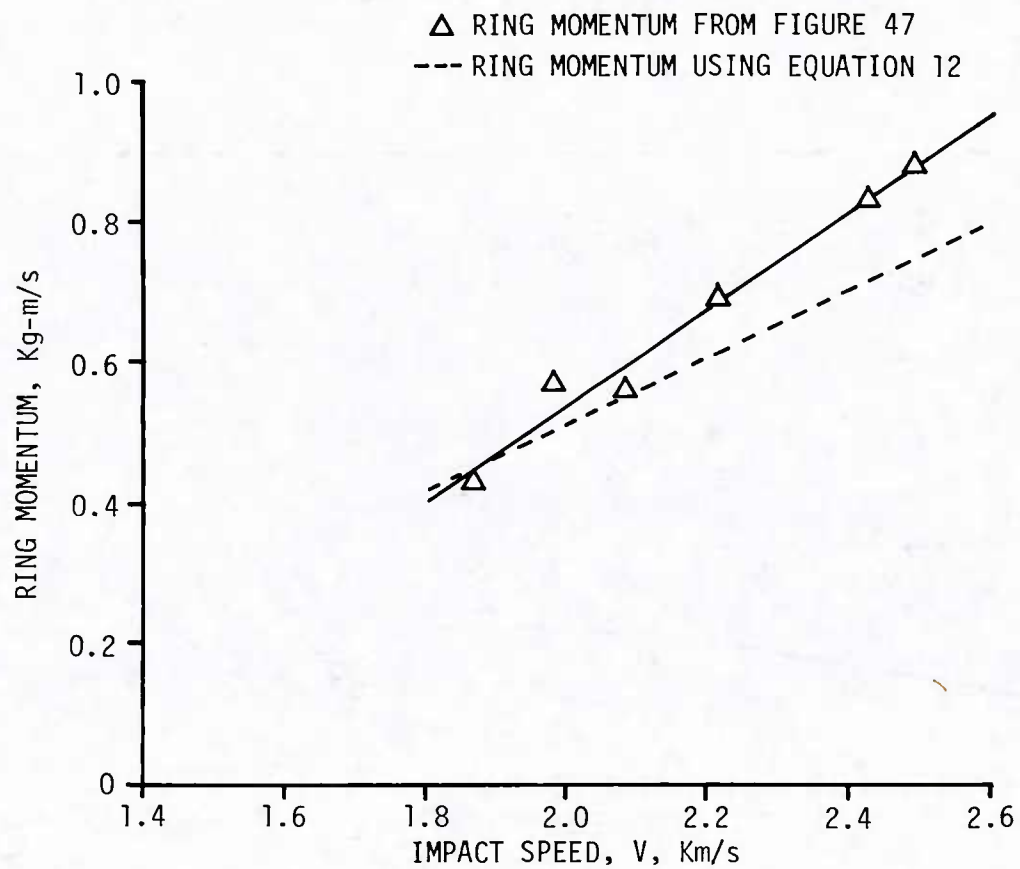


FIGURE 48. Momentum in the Peripheral System as a Function of Impact Speed. (Mild steel sphere, U.S. armor plate, $T/d = 1.$)

TARGET: 6.15 mm MILD STEEL
PROJECTILE: 6.35 mm MILD STEEL SPHERE

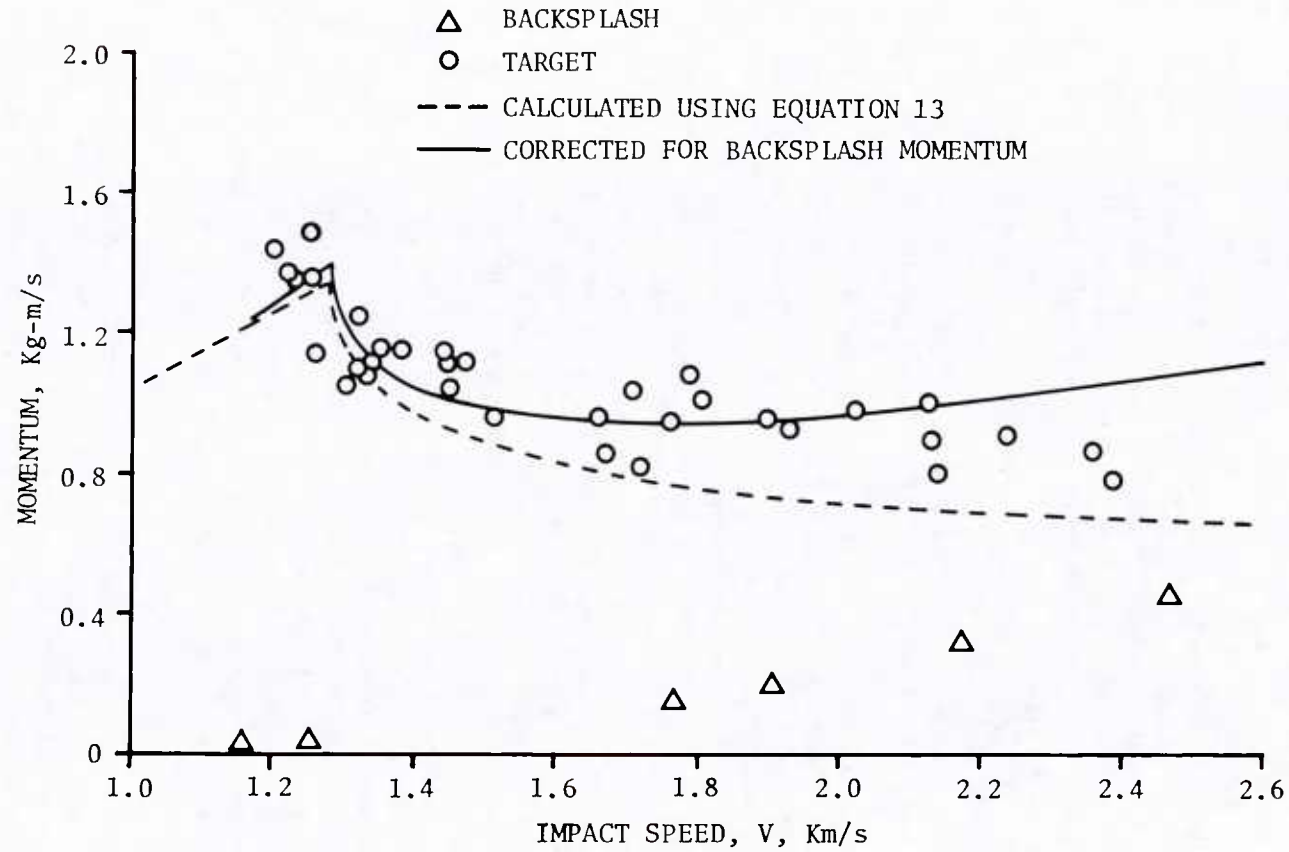


FIGURE 49. Momentum as a Function of Impact Speed. (Mild steel sphere, mild steel plate, $T/d = 1.$)

while the measured momenta at higher velocities fall significantly below the predictions even allowing for the scatter of the data. This behavior closely parallels that of the U.S. armor.

In an earlier project we chose SAE 4130 steel barstock cut into slices for a series of firings in order to avoid the fractures associated with rolling texture and the ring-type fragmentation that these fractures produce. It turned out that this choice of material eliminated ring-type peripheral fragmentation. The lead fragment speed of this target material as a function of impact speed has values intermediate between those measured for the U.S. armor and mild steel targets (Figure 50). Figure 33 showed a change in the dependence of V_x on impact speed, similar to that observed in firings against mild steel at high speeds and the U.S. armor material at virtually all speeds above the ballistic limit. In the case of the mild steel and U.S. armor targets these changes correlate to the observation of peripheral fragmentation in the form of ring-shaped additions to the exit side of the crater. Estimates of the momentum contributed by the fragments from the peripheral region correct the unexplained changes in V_x . In the case of SAE 4130 barstock, no change in crater shape occurs to indicate the onset of peripheral fragmentation. High speed photographs do show a group of fragments conspicuous for its large fragment sizes and low speeds. Some photographs actually show complete sleeves. Figure 51 presents measurements of these average fragment speeds. The fracture processes that form the fragments of the central region also form the fragments of the peripheral region. This precludes identification of all recovered fragments according to region by shape alone. Shape serves to identify fragments close to the axis of symmetry. A tedious process of comparing the shape of recovered fragments and photographic images of the group of large, slow-moving fragments resulted in identifying other recovered fragments as peripheral. In some instances this process leads to the estimates of the mass of the central region shown in Figure 52. In many other cases the identification proved impossible and the recovered fragments from the plate served only to measure the total mass ejected from the rear surface. The difference between a linear fit to the mass of the central region and a linear fit to the total mass beyond the point of an apparent change in the rate of increase of mass with impact speed gives our estimate of the mass of the peripheral region. From the data on the mass of the peripheral region and the average speed one can make an estimate of the momentum of the peripheral system L_y .

Figure 53 shows the relevant momentum data for the calculation of V_x as a function of V and Figure 33, presented earlier, shows the change in V_x for the inclusion of the peripheral momentum. A comparison of predicted and experimental momentum trends shows the same divergence at higher impact speeds that was seen in the other steels. This implies that the dynamics of the peripheral fragment systems are identical.

TARGET: 6.35 mm SAE 4130 BAR
PROJECTILE: 6.35 mm MILD STEEL SPHERE

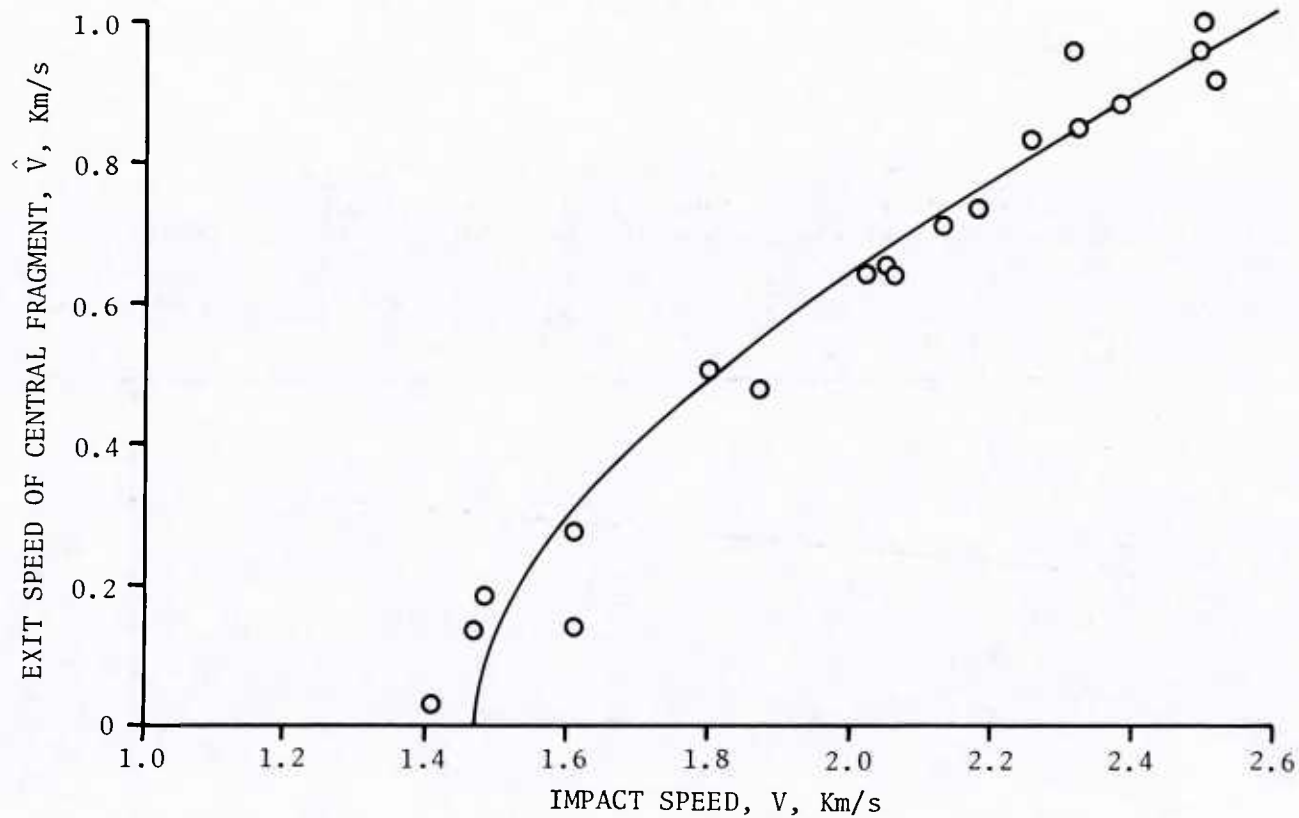


FIGURE 50. Residual Speed of the Lead Fragment as a Function of Impact Speed. (Mild steel sphere, 4130 steel bar, $T/d = 1.$)

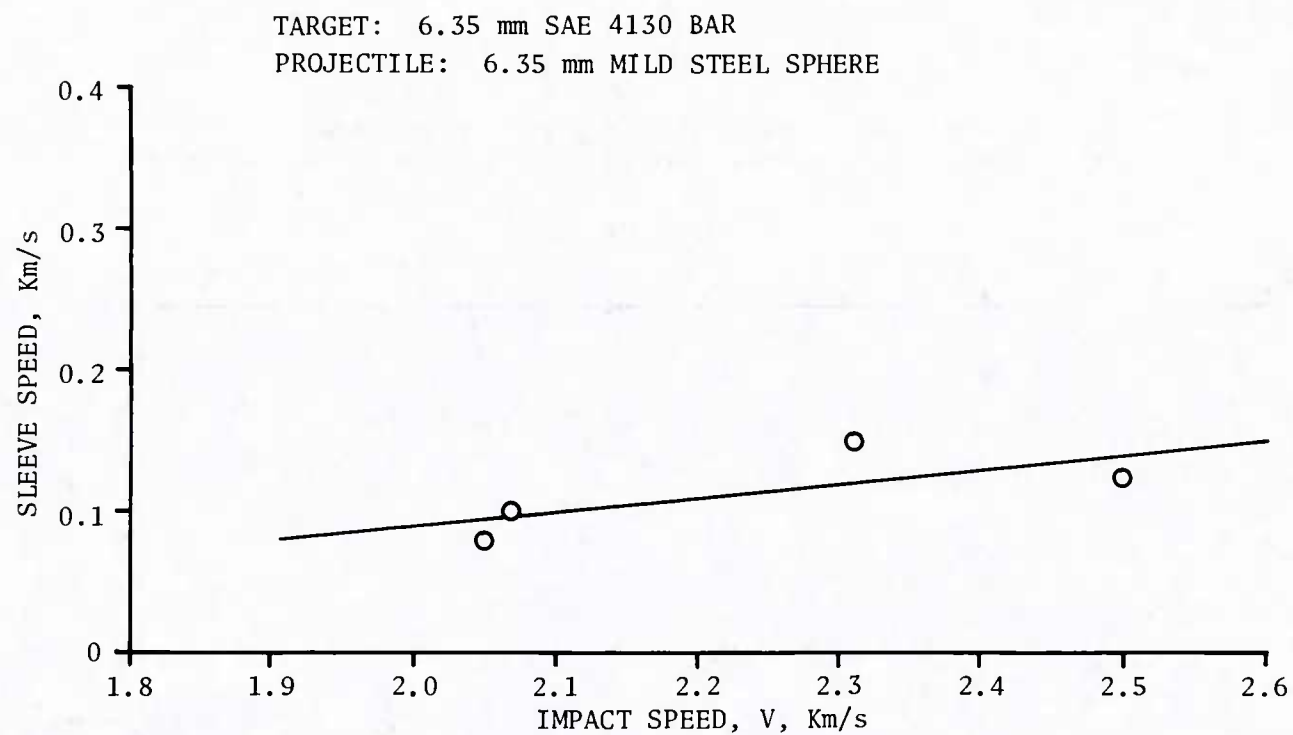


FIGURE 51. Average Speed of Sleeve Fragments as a Function of Impact Speed. (Mild steel sphere, 4130 steel bar, $T/d = 1.$)

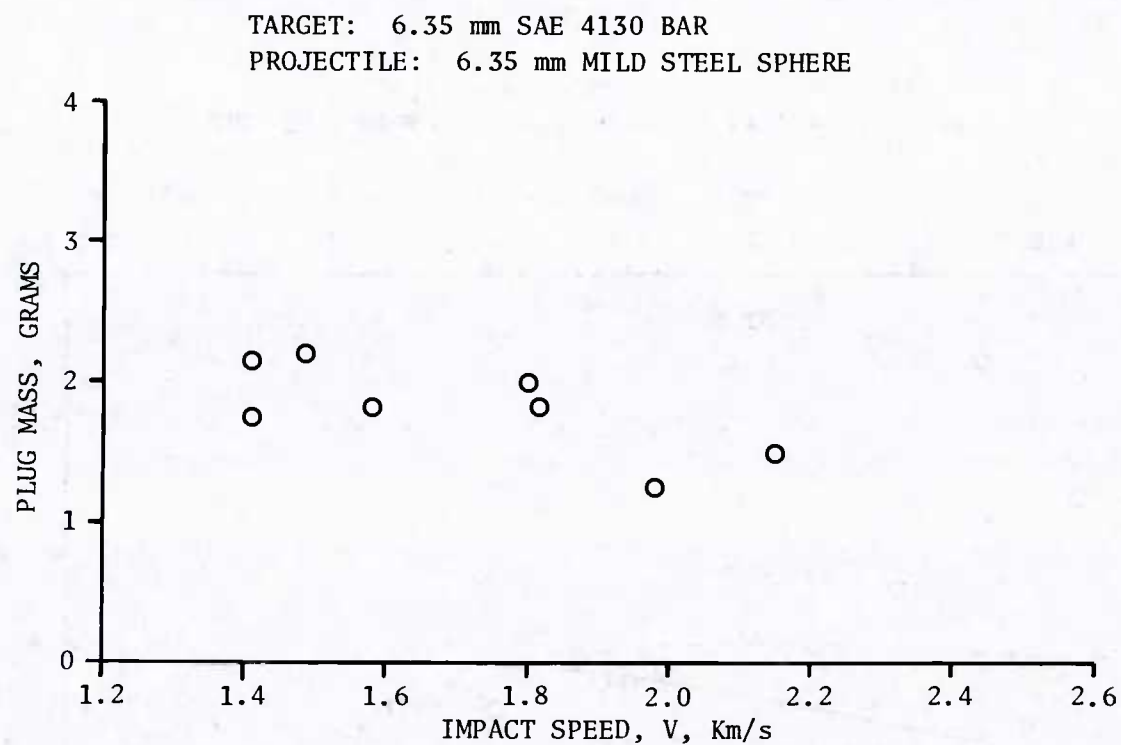


FIGURE 52. Mass of the Central Region as a Function of Impact Speed.
(Mild steel sphere, 4130 steel bar, $T/d = 1.$)

TARGET: 6.35 mm SAE 4130 BAR
PROJECTILE: 6.35 mm MILD STEEL SPHERE

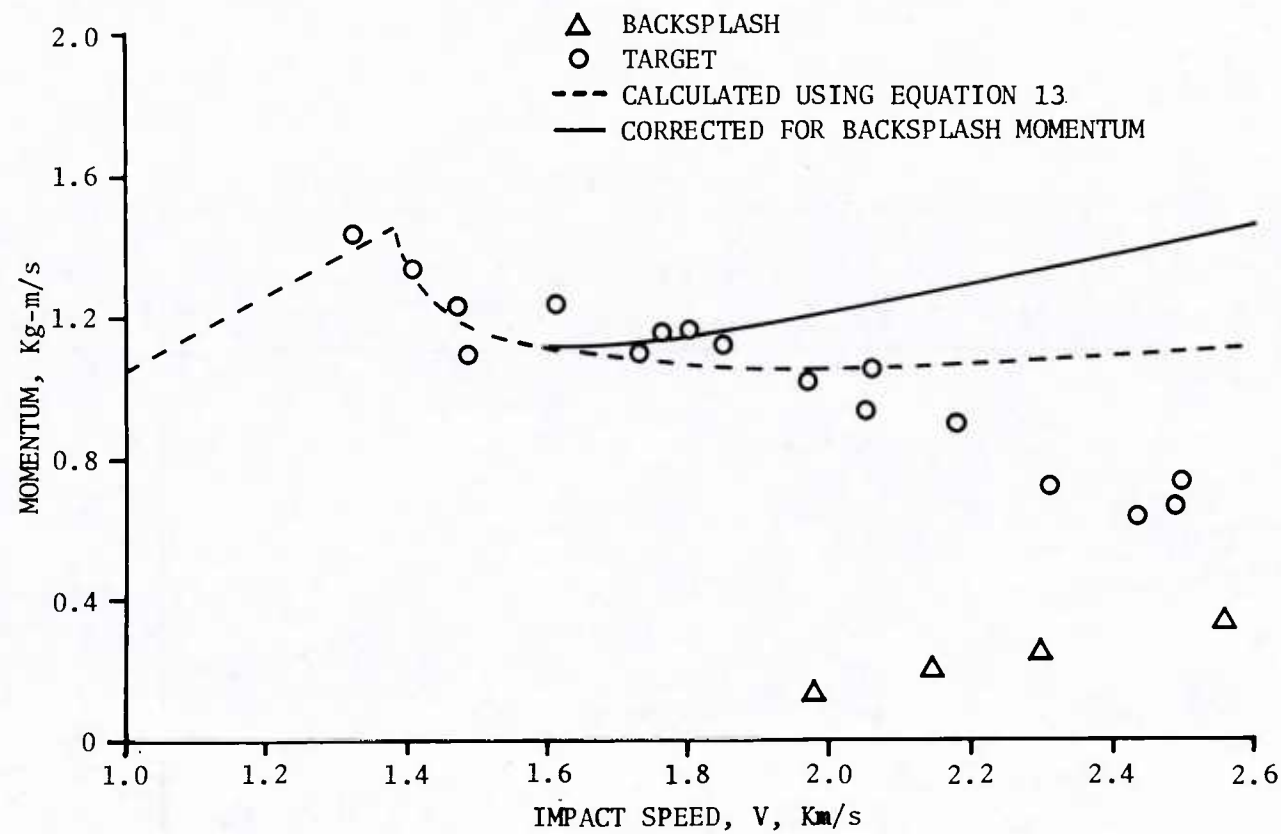


FIGURE 53. Momentum as a Function of Impact Speed.
(Mild steel sphere, 4130 steel bar,
 $T/d = 1.$)

Much of the data on the Soviet armor suffers from uncertainties in interpretation due to uncertainties about the microstructure of specific samples used as targets. These data come from earlier studies in which we cut thick samples of the armor into thinner plates and then treated these as identical in material properties. We now know that the plates from the outer parts of the parent material have martensitic microstructure while the microstructure of inner parts in addition contain free ferrite. As the preceding examples imply such differences of microstructure strongly influence the form of peripheral fragmentation. The data gathered on targets with such variations of material characteristics quite predictably exhibit considerable scatter.

Figure 54 presents data on the masses of collected fragments. The data on masses of the central region come from a limited number of firings in which it proved feasible to identify the central fragments with reasonable certainty by the procedures just described for the SAE 4130 steel targets. The data on ring mode masses come from firings in which ring mode fragments occurred. In some of these firings at higher speeds where ring mode fragments occurred fragments of sleeve mode appearance also occurred. Thus, the individual impacts varied with regard to the kind of peripheral fragmentation from impacts that exhibited sleeve mode fragmentation (markedly similar to that for SAE 4130 steel) to mixed mode fragmentation in which clearly identifiable ring mode fragments made up the bulk of the fragments.

Kerr cell camera photos tend to corroborate these differences in behavior. Figure 55 shows three fragment patterns; the top representative of a distribution with ring fragments only; the middle representative of a distribution of mixed modes and the bottom representative of a sleeve mode only. The sleeve mode patterns tend to have elongated shapes and to crowd the center line. Where the ring mode pattern exists it tends to have a disc-like shape and far greater divergence of the fragments than that exhibited by the sleeve mode. Figure 56 presents measurements of the average speeds of these groups as a function of impact speed.

For the Soviet armor, calculated values of V_x form two separate linear trends depending on whether the peripheral fragmentation is of a ring or sleeve mode (Figure 57). The complexities of the peripheral fragmentation process above 2 Km/s, where mixed modes commonly occur, result in large uncertainties in values of peripheral momentum. As a result, only data from impacts below 2 Km/s were used to calculate V_x values for perforations involving a sleeve mode (Figure 57). Perforations involving only a ring mode could be easily identified from an inspection of the target plates and also from the Kerr cell photos and so reliable values of peripheral momentum for this mode were obtained at all impact speeds.

TARGET: 6.35 mm SOVIET ARMOR
PROJECTILE: 6.35 mm MILD STEEL SPHERE

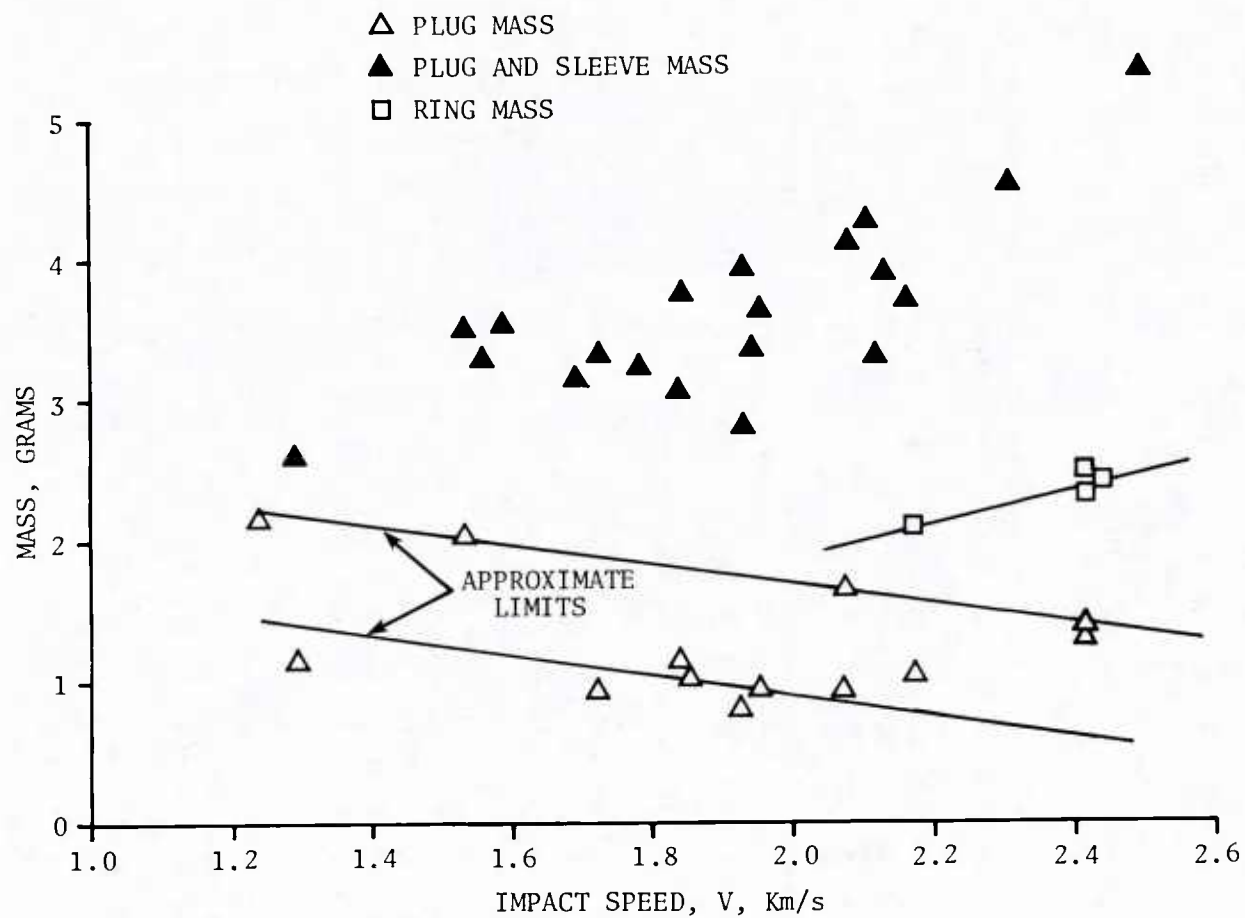
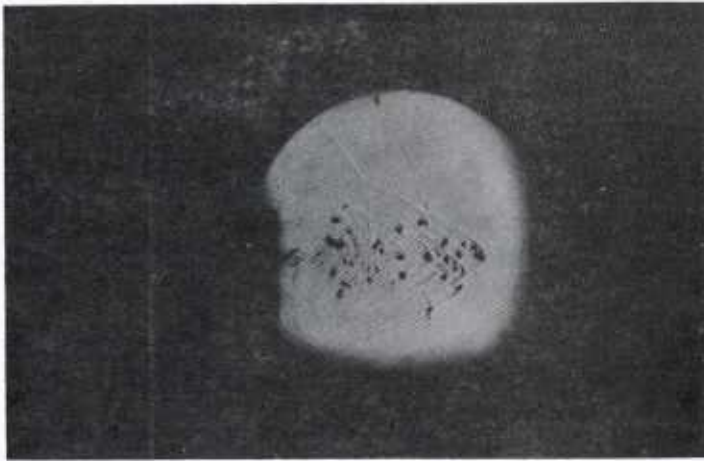


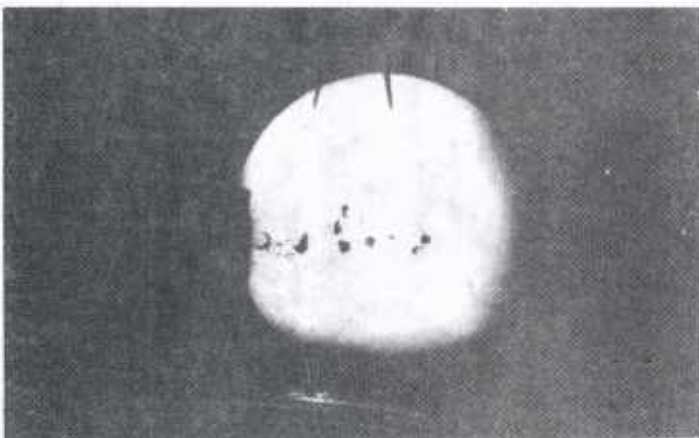
FIGURE 54. Peripheral Fragment Mass as a Function of Impact Speed. (Mild steel sphere, Soviet armor plate, $T/d = 1.$)



Ring mode, $V = 2.4 \text{ Km/s}$



Mixed mode
(ring and sleeve)
 $V = 2.2 \text{ Km/s}$



Sleeve mode,
 $V = 1.9 \text{ Km/s}$

FIGURE 55. High Speed Photographs of Fragment Distributions.
(Mild steel sphere, Soviet armor plate, $T/d = 1.$)

TARGET: 6.35 mm SOVIET ARMOR
PROJECTILE: 6.35 mm MILD STEEL SPHERE

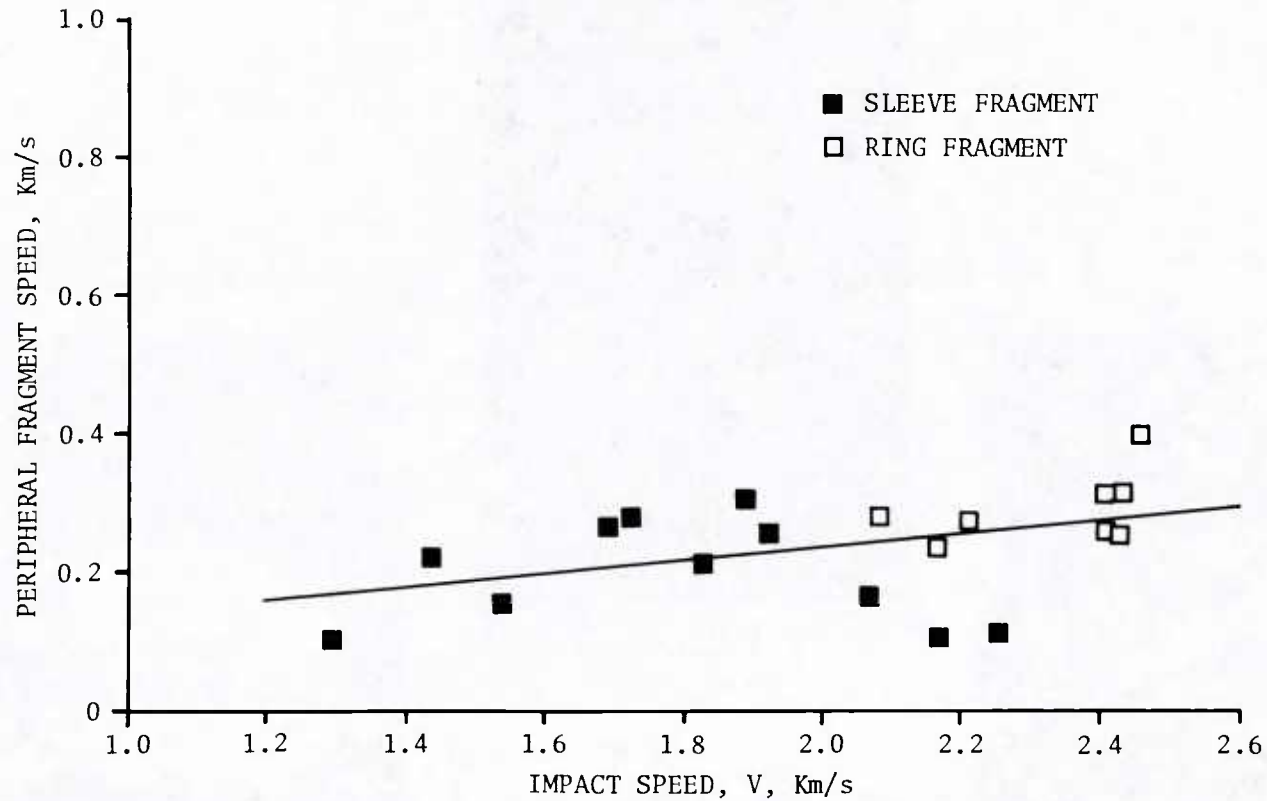


FIGURE 56. Average Speed of Peripheral Fragments as a Function of Impact Speed. (Mild steel sphere, Soviet armor, plate, $T/d = 1.$)

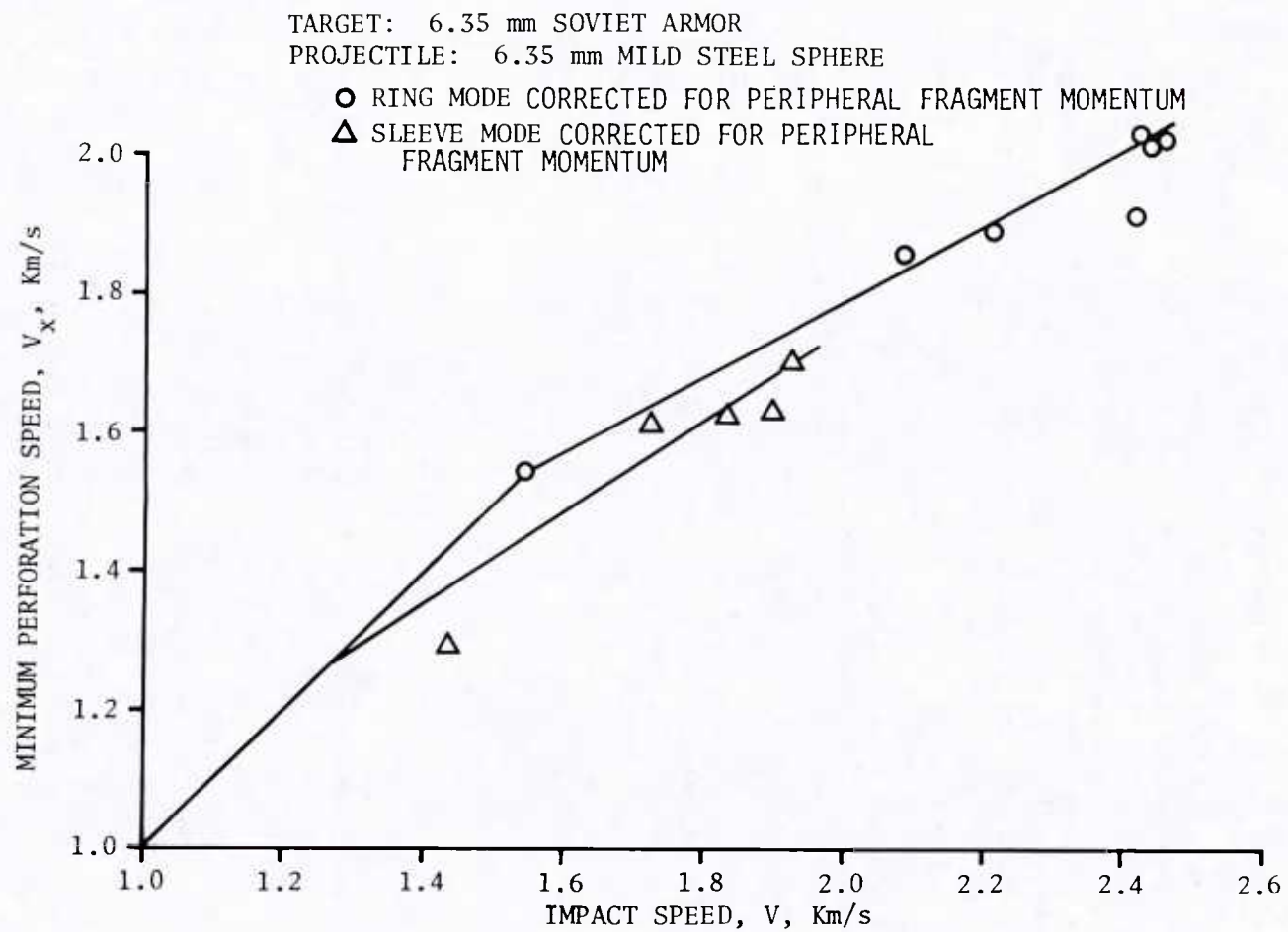


FIGURE 57. Minimum Perforation Speed as a Function of Impact Speed.
(Mild steel sphere, Soviet armor plate, $T/d = 1.$)

The corresponding momentum predictions for impacts involving these two modes of peripheral fragmentation are shown in Figure 58. Unfortunately, the lack of experimental data at the lower impact speeds prevented any comparison with the predictions from being made.

The preceding data on the three steels of this comparison, and the additional data on SAE 4130 steel, show that regions of peripheral fragmentation consistently develop at some impact speed above the ballistic limit. The lamellar microstructure of mild steel and the U.S. armoring material and its orientation parallel to the surfaces of the plate affect the fracture processes of fragmentation and result in annular shaped additions to the perforation orifice. These additions comprise simple visual evidence of a region distinct from the central region. Concurrent with the visual evidence of a peripheral region, momentum measurements provide evidence for the development of a new dynamic system. The remaining materials with different microstructures apparently can develop only fracture processes that belong to the same family that bounds the central region. As a result no visual changes in the perforation orifice mark the formation of a peripheral region, but momentum measurements again imply the development of a dynamic system distinct from that of the central region.

The peripheral system typically consists of large fragments moving at low speeds. The system derives its momentum from that transferred to the target as the projectile and central region of the target exchange momentum and come to the final states of motion observed on the exit side of the target. The shapes and velocities of the individual fragments depend on the fracture system that occurs for the given microstructural properties of the material.

Comparison of the Size of the Peripheral Regions

The preceding discussion of the evidence for the existence of distinct peripheral sources of fragments included measurements or estimates of the masses of the amount of peripheral material expelled as a function of impact speed. Figure 59 compares these data in a single plot. For the U.S. armor these data represent primarily the result of fragment collection and identification. For the Soviet armor and the SAE 4130 steel, these represent inferences from the total mass removed from the plates, estimates of the size of the central region, and an estimate of the amount of mass in the entry fragment system. These data suggest that the greatest amount of mass comes from the sleeve-type of peripheral fragmentation. This proves completely consistent with the concept that the sleeve form of peripheral region involves fractures that go all the way from contact with the projectile to the rear surface of the plate, while the ring form involves fragmentation at the rear surface.

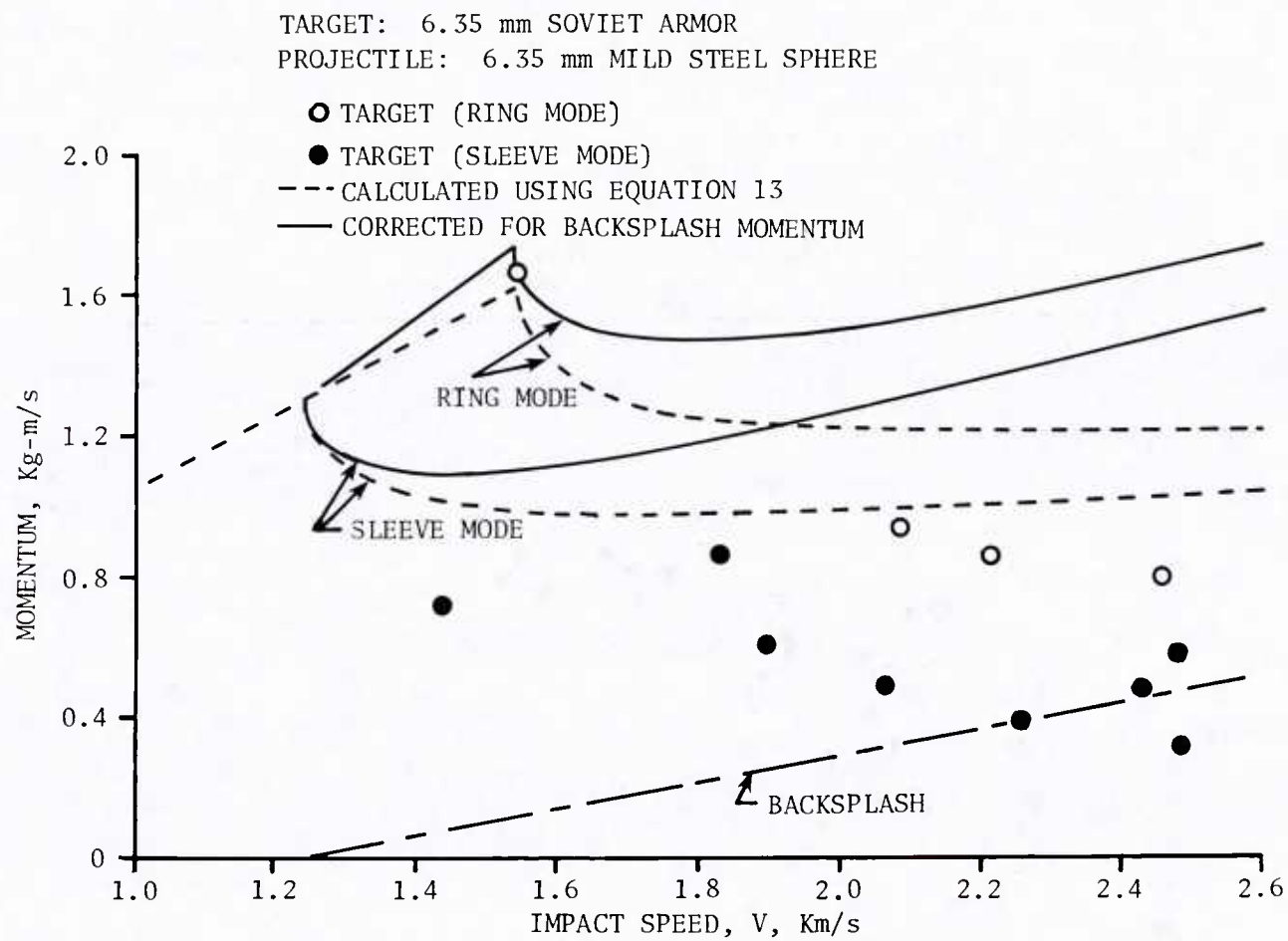


FIGURE 58. Momentum as a Function of Impact Speed. (Mild Steel sphere, Soviet armor plate, $T/d = 1.$)

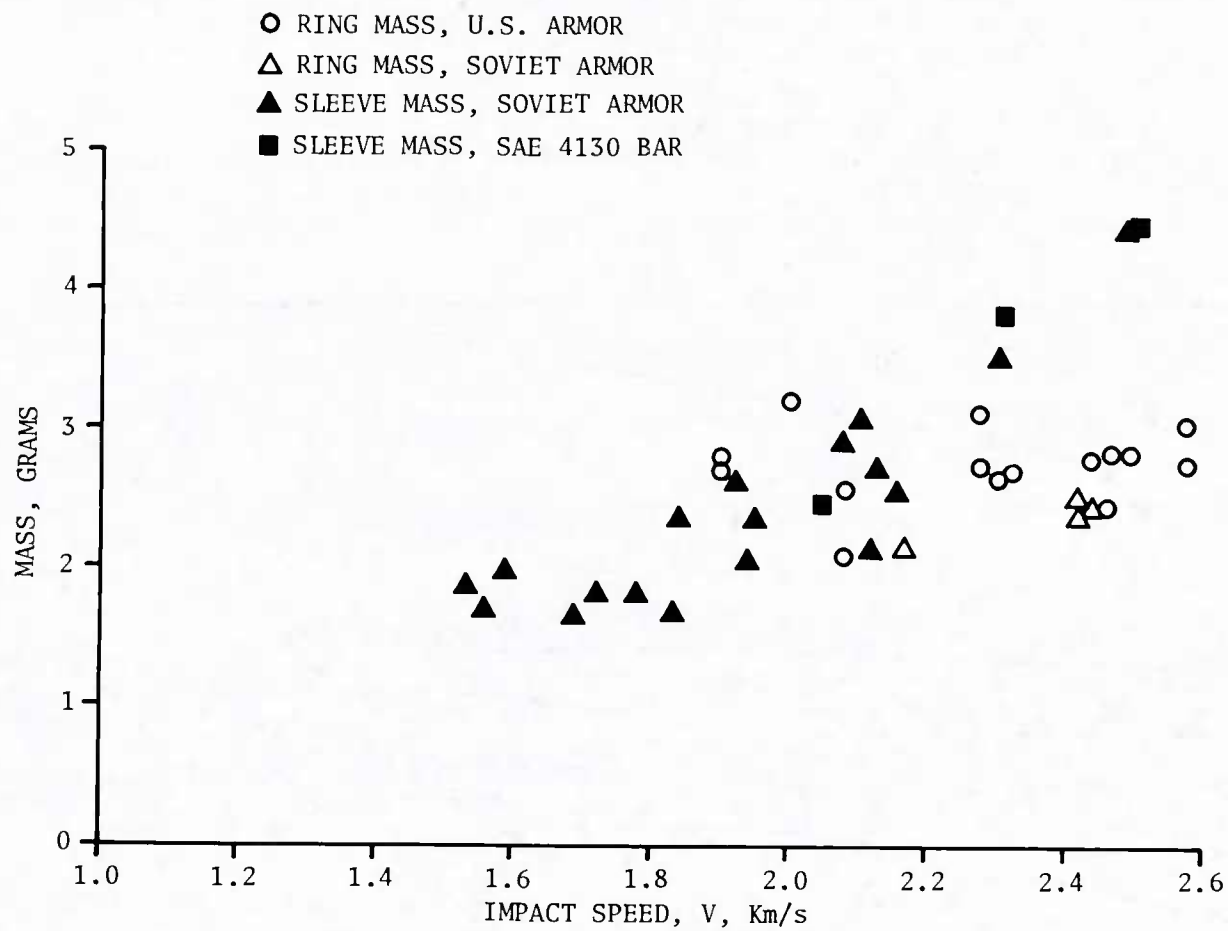


FIGURE 59. Comparison of the Masses of Peripheral Regions for a U.S. Armor, a Soviet Armor and 4130 Steel Bar. (T/d = 1.)

Measurement of crater diameters show that the lateral extent of these regions does not vary greatly from one material to another. Figure 60 shows these measurements as a function of impact speed.

On the whole the observations on the different alloys of steel support the hypothesis that the two fragmentation processes discussed earlier account for the peripheral regions. The principal fracture process is that associated with inhomogeneous plastic deformation which takes a special form if the material has well defined planes of weakness. The sample of Soviet armor exhibits the most complex behavior with indications that either both kinds of regions exist or one kind of region develops both kinds of fragments. The data and observations fail to give clear indication of how the two kinds of fragments occur. Perhaps a sleeve region has an early ring phase so that rings come off while the sleeve continues to form.

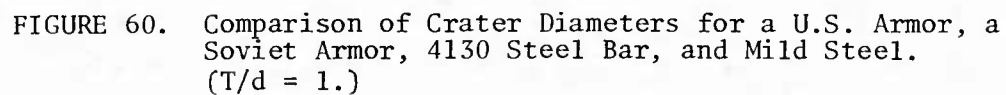
Fragmentation of the Peripheral Region

The preceding interpretations of the peripheral fragmentation of specific alloys prove consistent with an analysis of fragmentation that involves two major systems of fractures. The sleeve-mode system involves the same families of fractures that fragment the central region. Internal stress distributions appear to determine the spacial patterns of the shear-band fracture and cross fracture families. The ring-mode system involves completely distinct fracture families in that the distribution of planes of different material properties determines the spacial patterns of two of the families in the system. One of the families follows the lamellar structure of the alloy and fits the descriptive term "delamination fracture," while the other family tends to follow the direction orthogonal to the lamellar and fits the descriptive term "ring-separation fracture." A third family behaves the same way as the "cross fractures" of the central region.

Observations of crater cross sections suggest an increase in the number of shear-band fractures, delamination fractures, and cross fractures with increasing impact speed. On the other hand, the ring separation fractures appear to occur only once for any delaminated section. Figure 61 shows estimates of a number of peripheral fragments for the steels of the present comparison. The method of making these estimates was described in the section of the fragmentation of the central region and involves the use of Equation 9.

Effect of Variations of Plate Thickness

A limited amount of data on the U.S. armor illustrates the changes that occur in the previous results when the target thicknesses change. Residual velocity data measure the effectiveness of a target in resisting



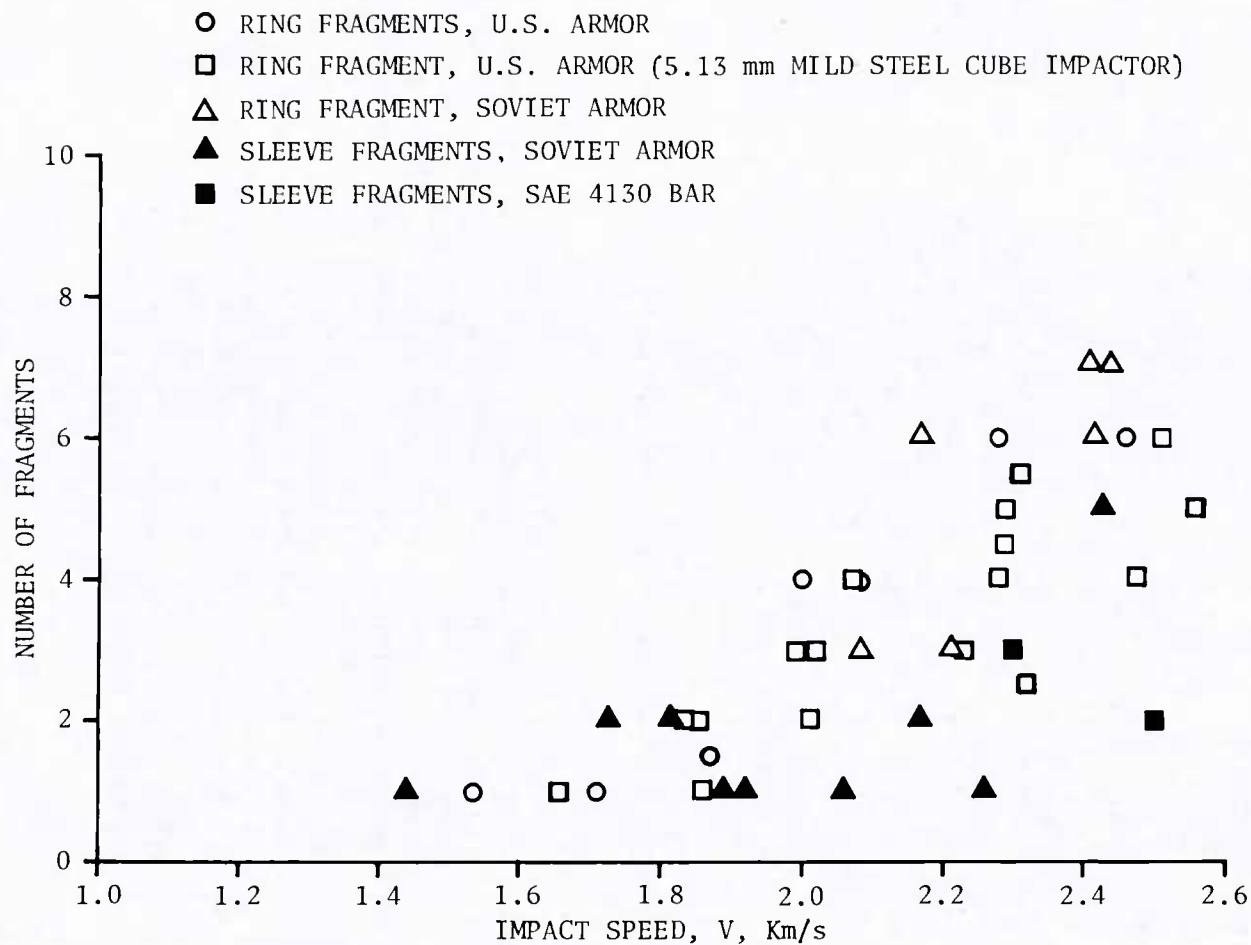


FIGURE 61. Number of Fragments from the Peripheral Region as a Function of Impact Speed for a U.S. Armor, a Soviet Armor and 4130 Steel Bar. ($T/d = 1.$)

a given projectile and provide a convenient means of demonstrating the effect of thickness. Figure 62 shows the velocity of the central fragment of the fragment system as a function of impact speed for $T/d = 1, 0.5,$ and 0.25 . The ballistic limits decrease with decreases of T/d and the slopes of the curves increase. These observations agree with the trends of empirical predictions.¹⁴

For $T/d = 0.5$ measurements of target momentum and backsplash momentum lead to the computed values of V_x shown in Figure 63. In the speed range from near the ballistic limit to above the speed where rings are initially developed, these data indicate a constant value of V_x and thus conform to the purest form of the plugging theory of perforation. Figure 64 shows the corresponding momentum predictions and the implication that peripheral fragmentation begins beyond 1.2 Km/s . Momentum measurements for plates of $T/d = 0.25$ give the V_x values shown in Figure 65. Again these conform to classical plugging theory near the ballistic limit and thus allow the momentum prediction of Figure 66. These data indicate peripheral fragmentation above 1.0 Km/s . These results have the interesting implication that the slope of the V_x curve for this material changes very rapidly with the parameter T/d since it goes from essentially zero at a value of 0.5 to 0.57 at a value of 1 .

FRAGMENTATION OF ALUMINUM TARGETS STRUCK BY ALUMINUM SPHERES

Certain data from an earlier investigation of aluminum systems allows a limited comparison of steel and aluminum systems. In this earlier effort 6.35 mm spheres and plates made up the impact system and the test results included many of the appropriate data such as the momentum measurements and collection of fragments. Unfortunately these data have gaps that prevent a complete characterization. Guesses and analogies have to replace solid experimental data. For example Figure 67 shows values of V_x computed by Equations 5 and 6 according to the methods described earlier. The scarcity of data at speeds just above the ballistic limit precludes a measurement of the slope of the V_x curve; however, similarities between the residual velocity curves for this aluminum-aluminum system and one of the steel-steel systems suggests comparable similarities in the V_x curves. The use of this similarity yields conclusions consistent with other independent observations and which indicate behavior like that of the steel systems.

¹⁴Joint Technical Coordinating Group for Munitions Effectiveness. *Penetration Equations Handbook for Kinetic-Energy Penetrators*, 61 JTCG/ME-77-16, 1 November 1977, pp. 16-17.

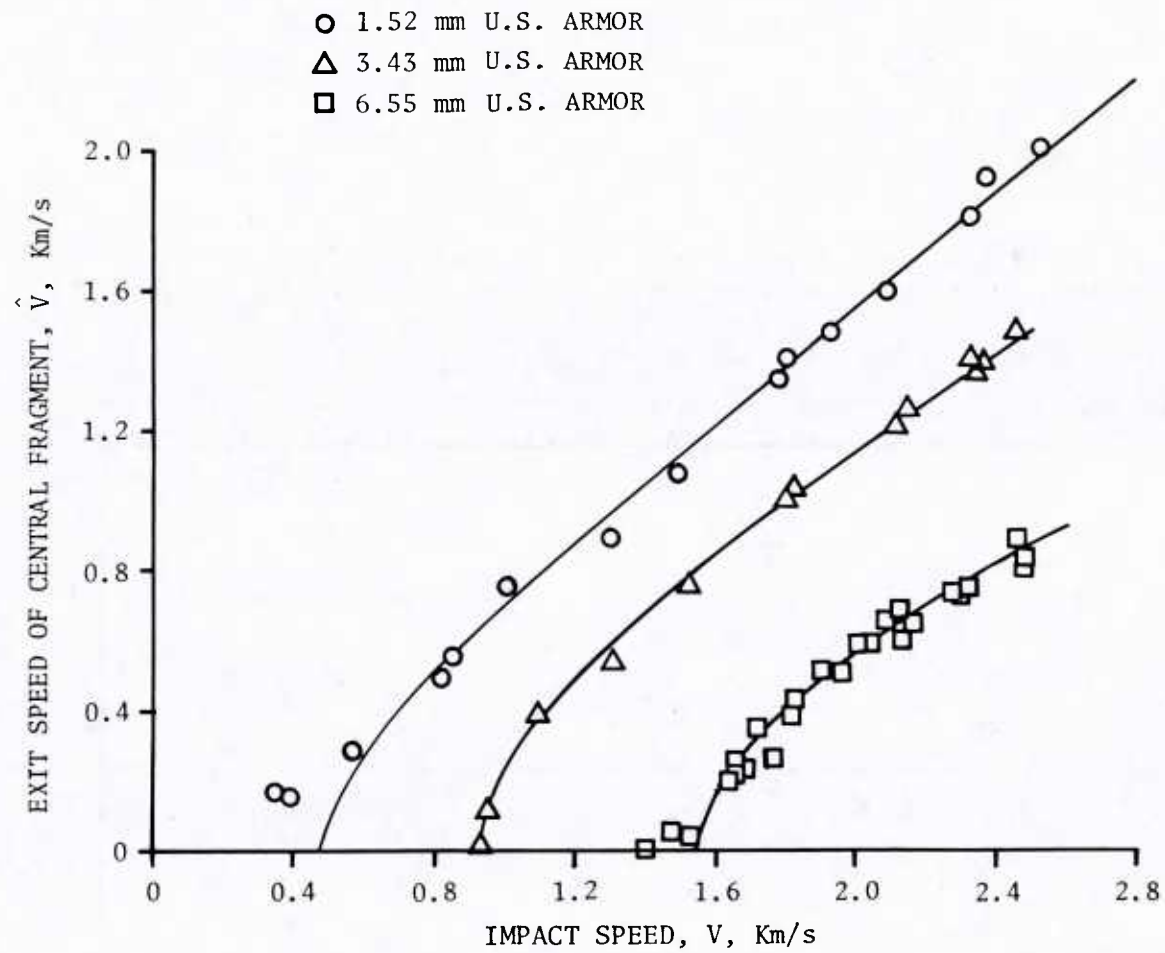


FIGURE 62. Comparison of Lead Fragment Speeds as a Function of Impact Speed for Three Values of T/d . (Mild steel sphere, U.S. armor plate.)

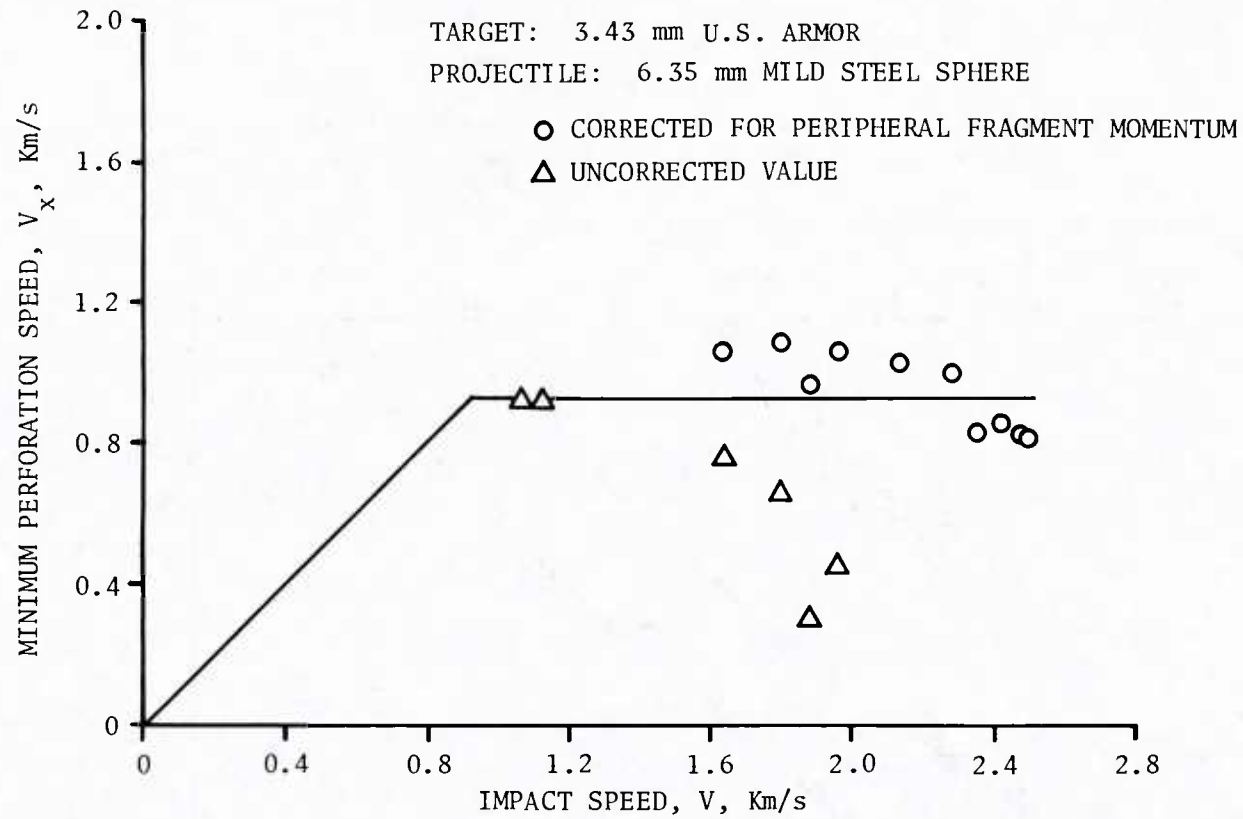


FIGURE 63. Minimum Perforation Speed as a Function of Impact Speed.
(Mild steel sphere, U.S. armor plate, $T/d = 0.5$.)

TARGET: 3.43 mm U.S. ARMOR
PROJECTILE: 6.35 mm MILD STEEL SPHERE

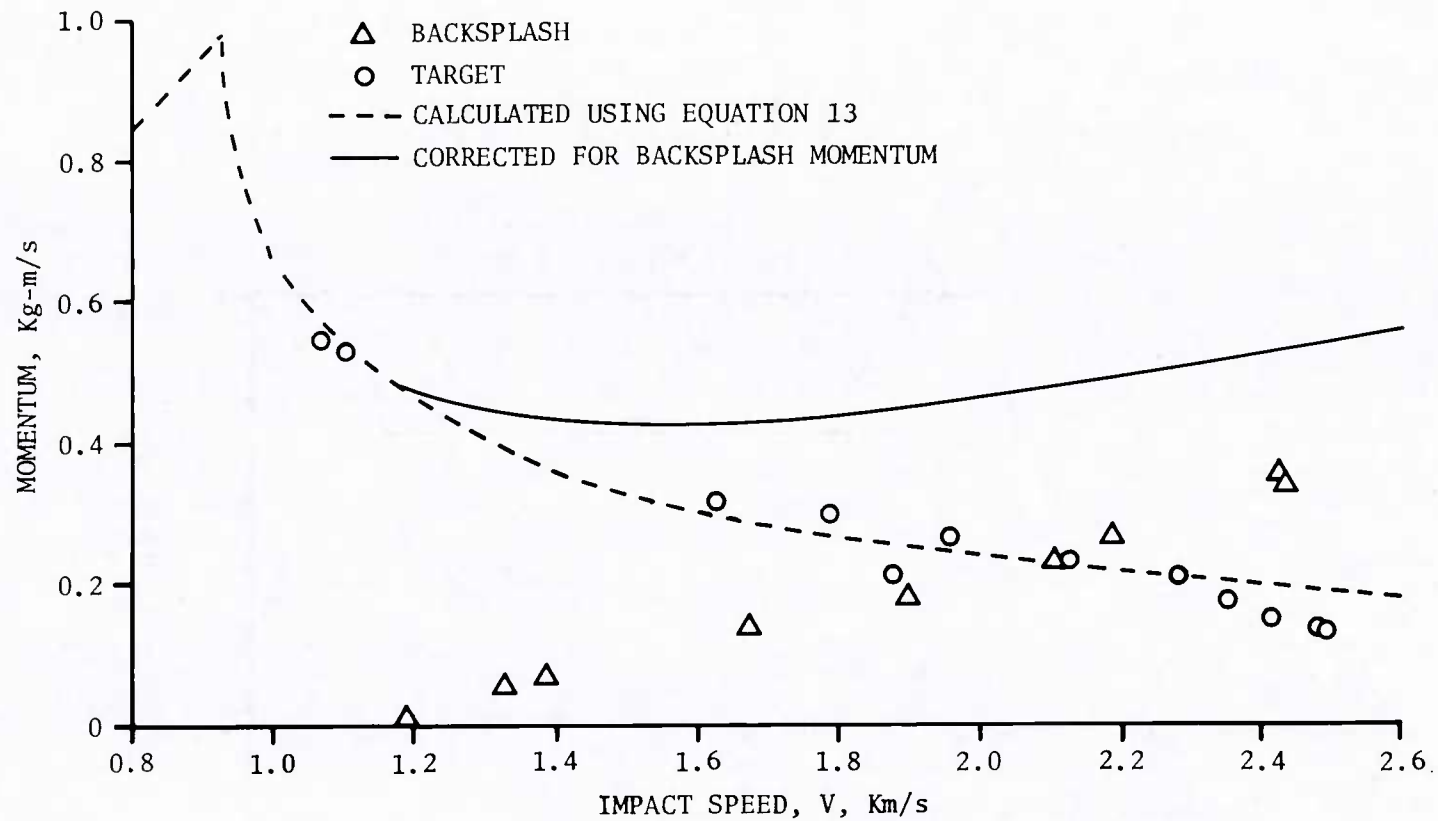


FIGURE 64. Momentum as a Function of Impact Speed. (Mild steel sphere, U.S. armor plate, $T/d = 0.5$.)

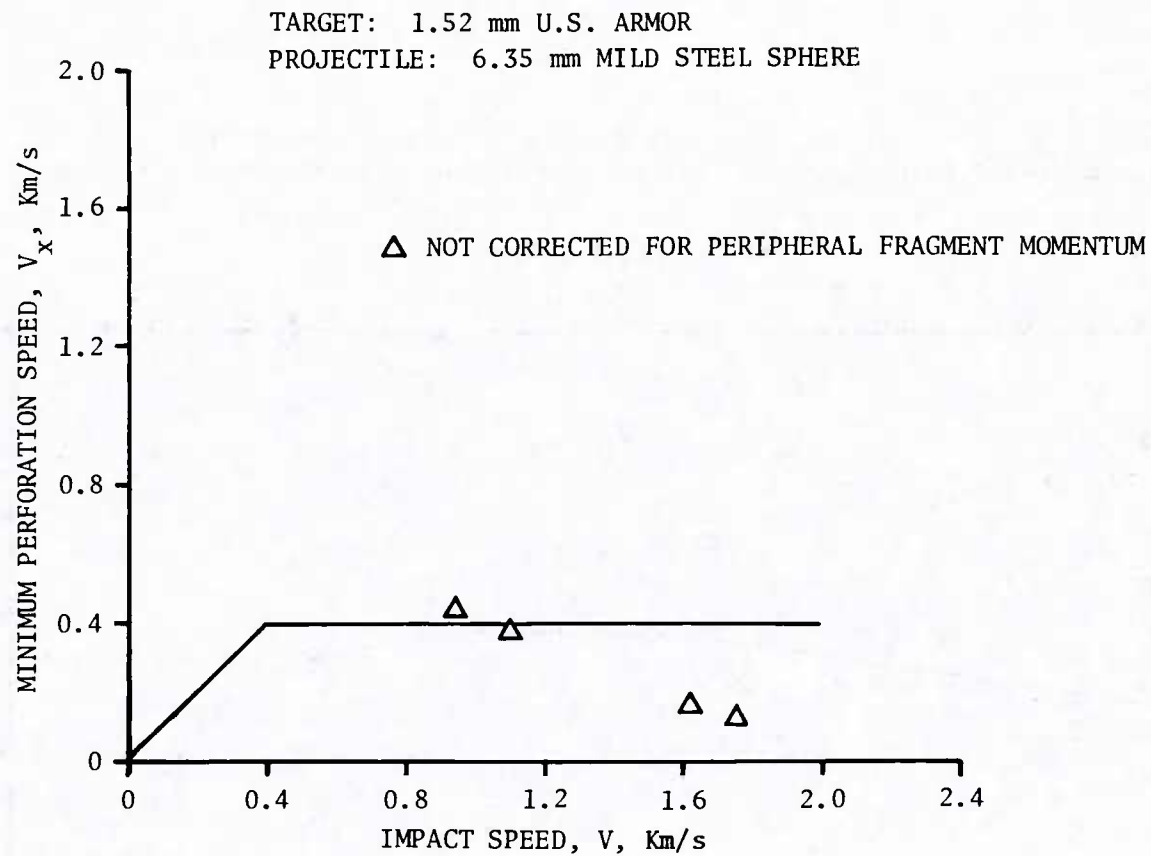


FIGURE 65. Minimum Perforation Speed as a Function of Impact Speed.
(Mild steel sphere, U.S. armor plate, $T/d = 0.25$.)

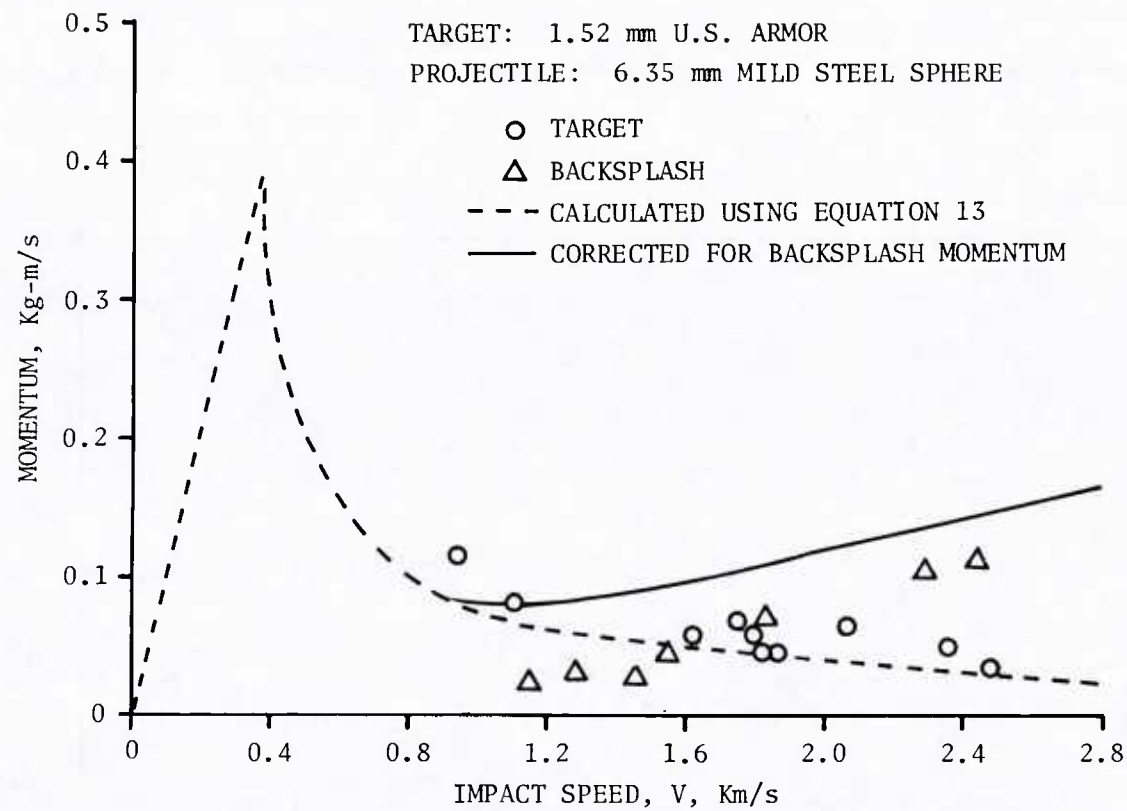


FIGURE 66. Momentum as a Function of Impact Speed.
(Mild steel sphere, U.S. armor plate,
 $T/d = 0.25$.)

TARGET: 6.35 mm 2024-T4 ALUMINUM

PROJECTILE: 6.35 mm 2024-T4 ALUMINUM SPHERE

○ CORRECTED FOR PERIPHERAL FRAGMENT MOMENTUM
△ UNCORRECTED VALUES

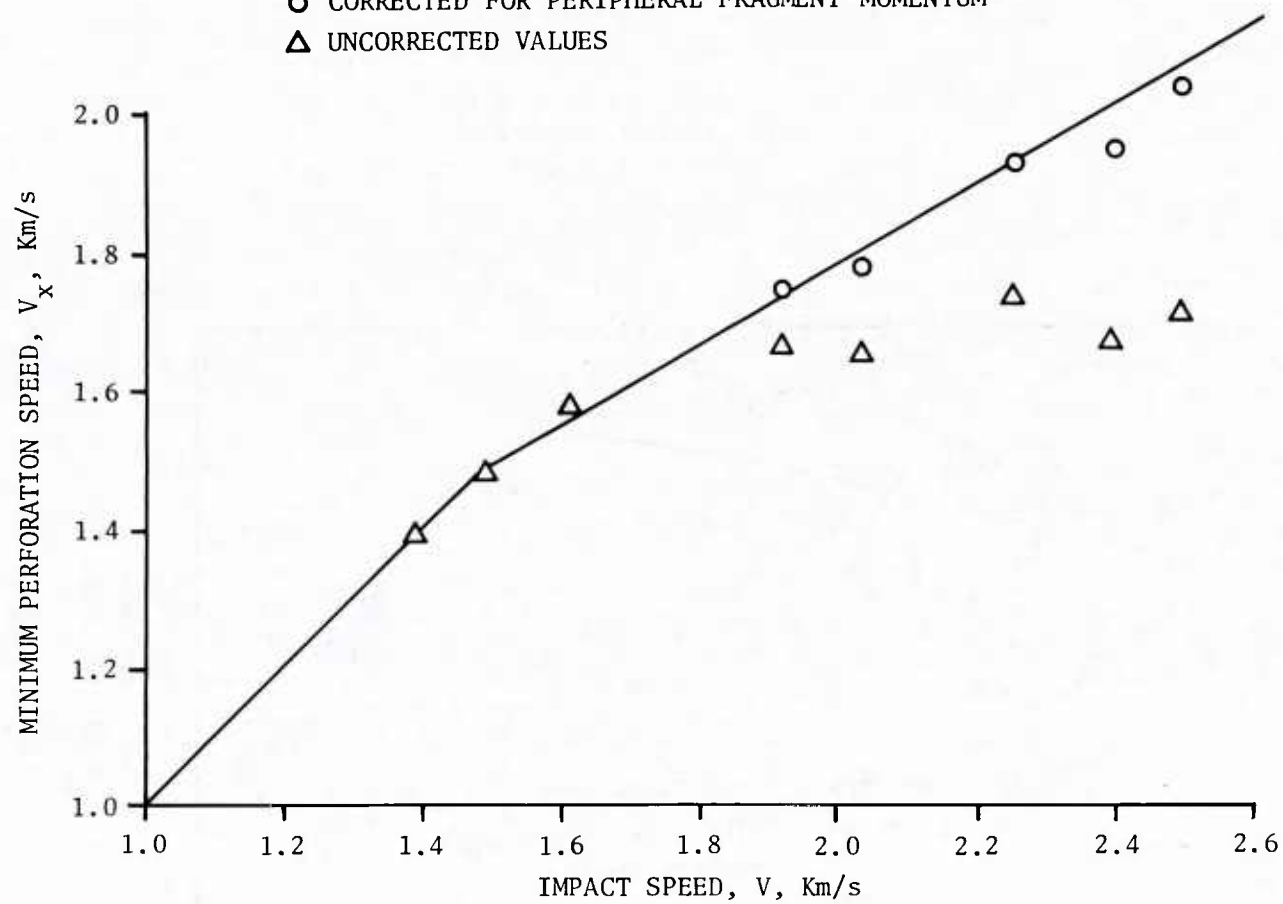


FIGURE 67. Minimum Perforation Speed as a Function of Impact Speed.
(Aluminum sphere, aluminum plate, $T/d = 1.$)

Figure 68 shows residual speed data for the lead fragment for the aluminum-aluminum system. The ballistic limit of this system comes within 5% of that for the mild steel sphere and U.S. armor. The rest of the curve falls within 10% of the steel-steel curve. These data approximately fit the empirical curve

$$V_r = R \sqrt{V^2 - V_x^2} \quad (14)$$

that has been derived from plugging theories. In these theories R is a dimensionless constant dependent on the ratio of plug to projectile mass, and V_x has the meaning of the minimum perforation velocity. It seems reasonable that the data from two systems of the same material and that fit the same form of the above equation either have the same values of R and V_x or variable values that compensate one for the other. Measurements of the size of the central region, or plug, by fragment collection and identification method give the data of Figure 69. These indicate sizes and a trend in the change of size like that for mild steel. Thus the similarity of residual speed curves and sizes of the central region suggests similarity in the values of V_x and R . On the basis of this similarity we chose a slope of 0.6 (which holds for the steel) as the slope of the V_x curve for the aluminum system.

Figure 70 shows the momentum data and the prediction based on the assumed V_x relation. The data at higher speeds imply a loss of momentum due to peripheral fragmentation. The observation of the onset of peripheral rings agrees with the onset of the momentum deficiency in these data.

Measurement of recovered ring fragments (Figure 71) and measurements of the speeds of ring fragments from Kerr cell camera data (Figure 72) combine to give momentum estimates that correct the data of Figure 67 to the circled points.

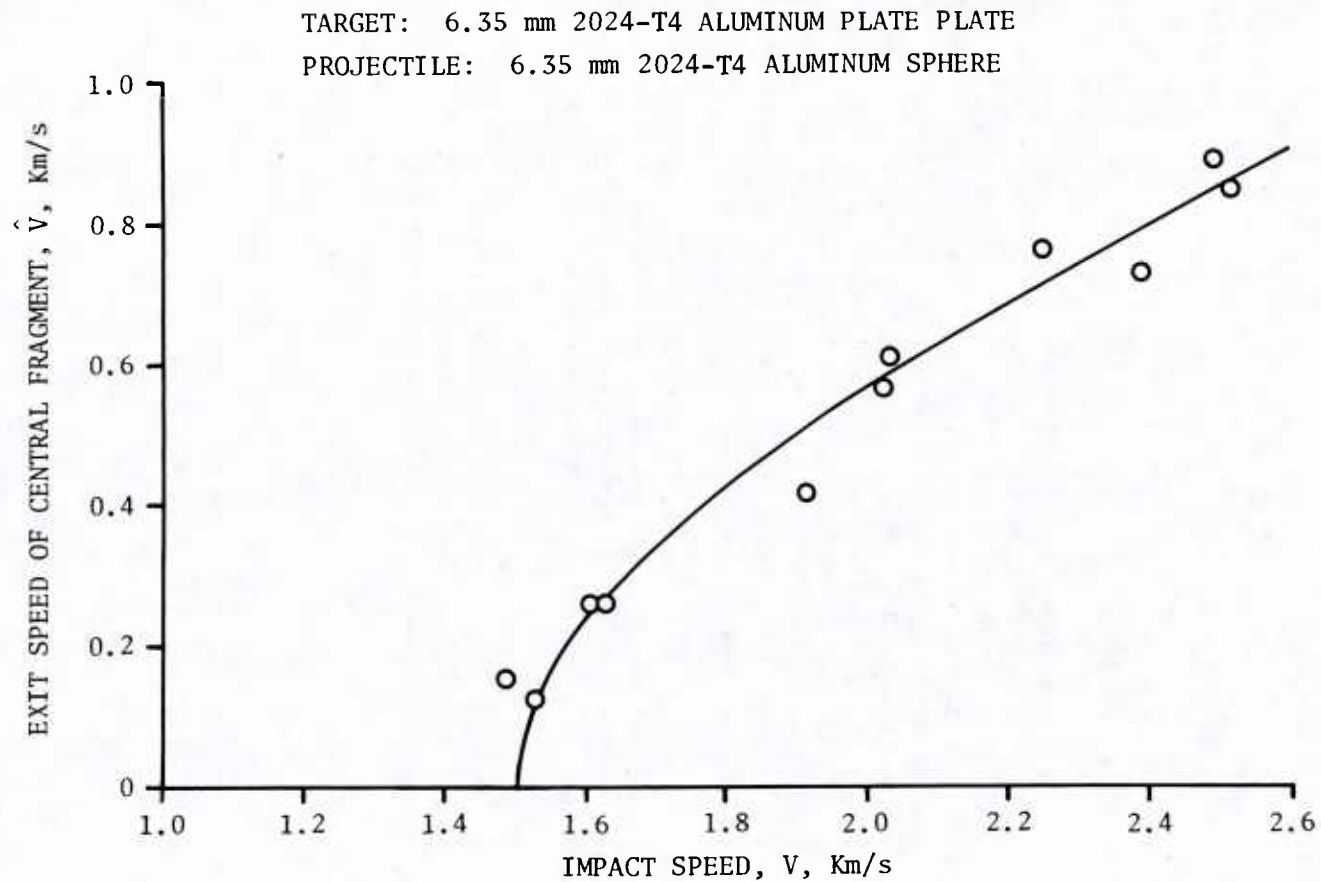


FIGURE 68. Residual Speed of the Lead Fragment as a Function of Impact Speed.
(Aluminum sphere, aluminum plate, $T/d = 1.$)

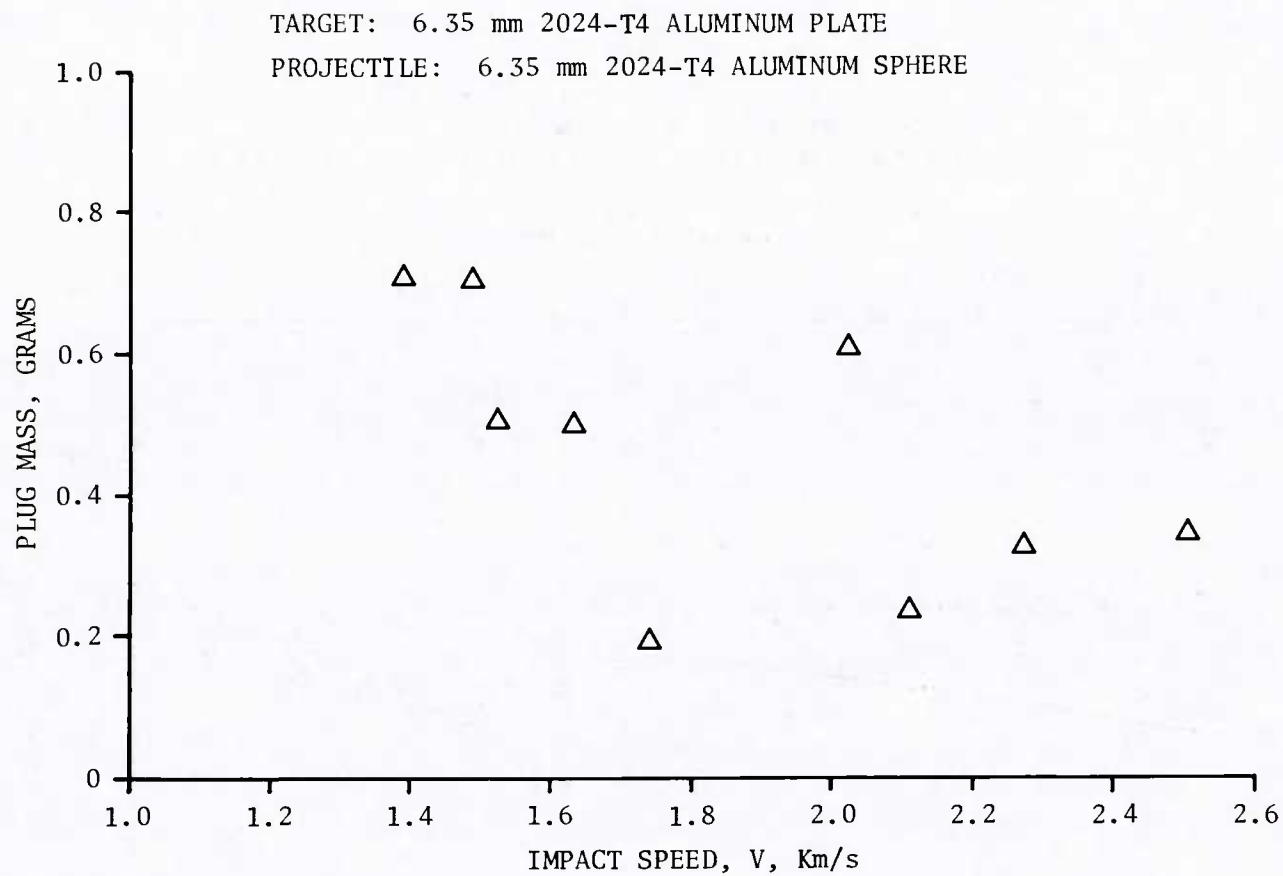


FIGURE 69. Mass of the Central Region as a Function of Impact Speed.
(Aluminum sphere, aluminum plate, $T/d = 1.$)

TARGET: 6.35 mm 2024-T4 ALUMINUM PLATE
PROJECTILE: 6.35 mm 2024-T4 ALUMINUM SPHERE

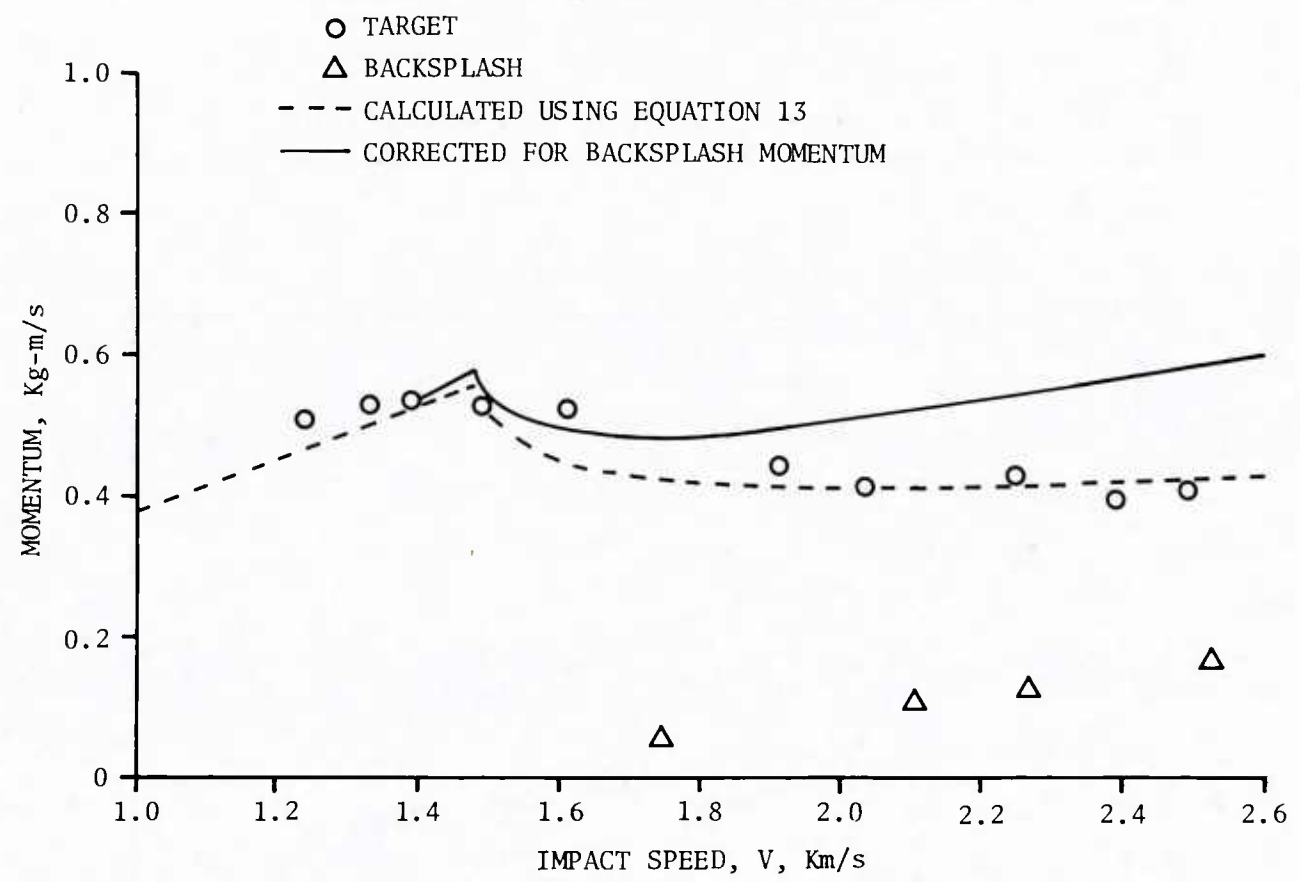


FIGURE 70. Momentum as a Function of Impact Speed.
(Aluminum sphere, aluminum plate,
T/d = 1.)

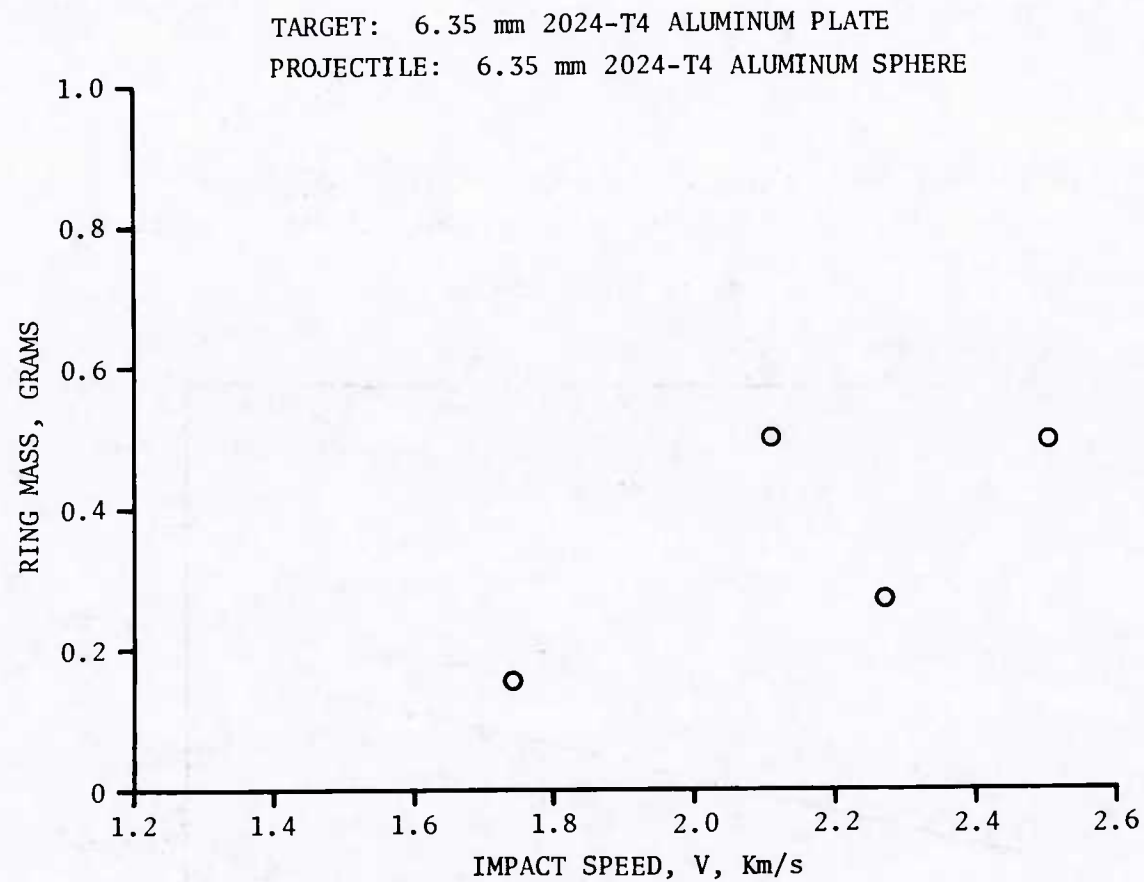


FIGURE 71. Mass of the Ring-Mode Peripheral Region as a Function of Impact Speed. (Aluminum sphere, aluminum plate, $T/d = 1.$)

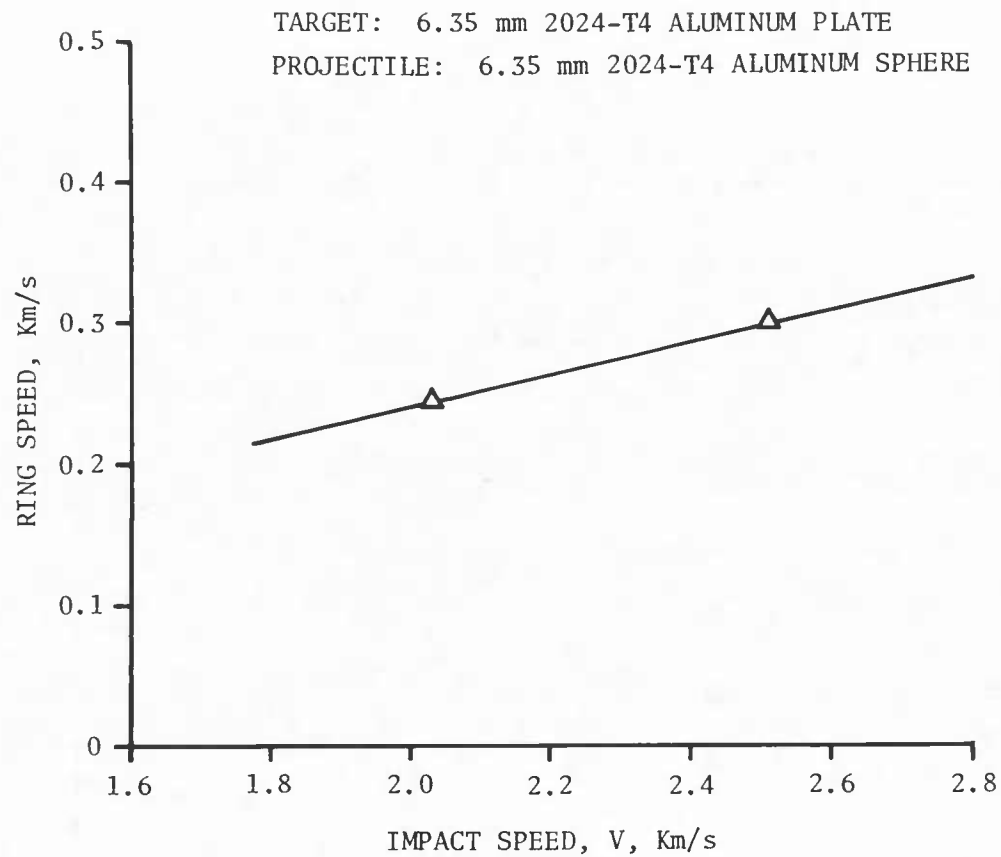


FIGURE 72. Average Speed of Ring Fragments as a Function of Impact Speed. (Aluminum sphere, aluminum plate, $T/d = 1.$)

CONCLUSIONS

The fragmentation of plates by the impact of compact projectiles has been studied for several systems. These show that while the fragmentation resulting from impact proves to be complex and variable, it has definite regularities that allow the identification of the major patterns and kinds of fracture. The fragments come from edges of the entry side of the crater and distinct central and peripheral regions of the exit side of the crater. Patterns due to inhomogeneous shear bands constitute the most common element, but in the peripheral region a lamellar microstructure may result in a kind of delaminating failure that overrides the tendency to follow shear bands. Momentum and energy considerations indicate that fragments from the peripheral region obtain their momentum from that transferred to the target during impact rather than from direct contact with the projectile.

NOMENCLATURE

D	Diameter of crater at front of plate
H	Axial thickness of crater
L	Momentum transferred to target
L^*	Momentum of ballistic pendulum
L_f	Backsplash momentum
L_y	Momentum of peripheral system
N	Total number of fragments from hole counts in a paper layer
N^*	Total number of fragments from hole counts in a Celotex layer
N_q	Estimated number of fragments from the central region
P	Penetration depth
R	Dimensionless constant
T	Target thickness
V	Impact velocity
V^*	Critical velocity where inhomogeneous plastic deformation initiates
\bar{V}	Velocity of center of plug/projectile mass system
\hat{V}	Velocity of lead fragment
V_o	Ballistic limit
V_r	Residual velocity
V_x	Minimum perforation velocity
V_y	Average velocity of peripheral fragments
V_{yo}	Constant
d	Diameter of spherical projectile
m_f	Mass ejected from impact side of target
m_p	Initial projectile mass
m_p'	Mass of projectile after perforation
m_q	Mass of central region
m_T	Total mass ejected from target
m_y	Mass ejected from the peripheral region
m_{yo}	Constant

n_i	Number of fragments from a given source region
n_p	Number of fragments identified as pieces of projectile
n_q	Number of fragments identified as pieces of the central region
n_x	Number of fragments collected but not identified
n_y	Number of fragments identified as pieces of the peripheral region
α	Constant
ρ	Constant
ϵ	Strain
ϵ^*	Critical strain where inhomogeneous plastic deformation initiates
ϵ_1	Mean strain in axial direction
ϵ_2	Mean strain along crater bottom

INITIAL DISTRIBUTION

- 8 Naval Air Systems Command
 - AIR-301 (2)
 - AIR-320, B. Warren (1)
 - AIR-320D (1)
 - AIR-541 (2)
 - AIR-7226 (2)
- 5 Chief of Naval Operations
 - OP-03 (2)
 - OP-05 (1)
 - OP-098 (1)
 - OP-55 (1)
- 1 Chief of Naval Material (MAT-05)
- 3 Chief of Naval Research, Arlington
 - ONR-102 (1)
 - ONR-461 (1)
 - ONR-474 (1)
- 7 Naval Sea Systems Command
 - SEA-62R (5)
 - SEA-09B312 (2)
- 1 Commander in Chief, U.S. Pacific Fleet (Code 325)
- 1 Air Test and Evaluation Squadron 5
- 1 Commander, Third Fleet, Pearl Harbor
- 1 Commander, Seventh Fleet, San Francisco
- 1 David W. Taylor Naval Ship Research and Development Center, Bethesda
- 1 Naval Academy, Annapolis (Director of Research)
- 1 Naval Air Force, Atlantic Fleet
- 2 Naval Air Force, Pacific Fleet
- 1 Naval Air Station, North Island
- 2 Naval Air Test Center, Patuxent River (CT-252, Bldg. 405)
- 1 Naval Avionics Center, Indianapolis (Technical Library)
- 1 Naval Explosive Ordnance Disposal Technology Center, Indian Head
- 1 Naval Ocean Systems Center, San Diego (Code 447)
- 1 Naval Ordnance Station, Indian Head (Technical Library)
- 1 Naval Postgraduate School, Monterey
- 3 Naval Ship Weapon Systems Engineering Station, Port Hueneme
 - Code 5711, Repository (2)
 - Code 5712 (1)
- 3 Naval Surface Weapons Center, Dahlgren
 - G13
 - D. Dickinson (1)
 - T. Wasmund (1)
 - G22, W. Holt (1)
- 5 Naval Surface Weapons Center, White Oak Laboratory, Silver Spring
 - R10, S. Jacobs (1)
 - R12, J. Erkman (1)
 - R13, R. Liddiard (1)
 - Guided Missile Warhead Section (1)
 - Technical Library (1)
- 1 Naval War College, Newport

- 1 Office of Naval Research, Pasadena Branch Office
- 1 Office of Naval Technology, Arlington (MAT-07)
- 1 Operational Test and Evaluation Force, Atlantic
- 2 Pacific Missile Test Center, Point Mugu
 - Code 1245, Nofrey (1)
 - Technical Library (1)
- 1 Marine Corps Air Station, Beaufort
- 1 Army Armament Materiel Readiness Command, Rock Island (DRSAR-LEP-L, Technical Library)
- 4 Army Armament Research and Development Command, Dover
 - DRDAR-LCU-SS, J. Pentel (1)
 - Technical Library (3)
- 1 Aberdeen Proving Ground (Development and Proof Services)
- 10 Army Ballistic Research Laboratory, Aberdeen Proving Ground
 - AMSAA
 - C. Alston (1)
 - Blomquist (1)
 - AMXAR-SEI-B (1)
 - AMXAR-T, Detonation Branch (1)
 - AMXAR-TSB-S (STINFO) (1)
 - AMXBR-TBD
 - J. Dahn (1)
 - J. Kenecke (1)
 - AMXBR-VLDA, T. Bentley (1)
 - AMXSY-AD (1)
 - AMXSY-J (1)
- 1 Army Materiel Systems Analysis Activity, Aberdeen Proving Ground (K. Meyers)
- 2 Army Research Office, R
 - DRXPO-IP-L, Informa.
 - Dr. E. Saible (1)
- 1 Harry Diamond Laboratories
- 1 Radford Army Ammunition Plant
- 1 Redstone Arsenal (Rocket Development and Test and Evaluation Branch)
- 2 Rock Island Arsenal
 - Navy Liaison Office (NVL)
 - Technical Library (SARRI)
- 1 White Sands Missile Range
- 1 Yuma Proving Grounds (ST)
- 1 Tactical Air Command, Langley (QD-M)
- 1 Air Force Armament Division, Eglin (AFATL/FWW)
- 1 Air Force Armament Division, Eglin (AFATL/DLYV, Technical Library)
- 1 Air Force Armament Division, Eglin (AFATL/DLYV, K. McArdle)
- 1 Air Force Armament Division, Eglin (AFATL/DLYV, A. Rutland)
- 1 Air Force Intelligence Service, Bolling (AFATL/INTAW, Maj. R. Lecklider)
- 1 Air University Library, Maxwell Air Force Base
- 1 Tactical Fighter Weapons Center, Hurler Army Base (OT, FWW/DTL)
- 2 57th Fighter Weapons Wing, Nellis Air Force Base (OT, FWW/DTL)
- 1 554th Combat Support Group, Nellis Air Force Base (OT, FWW/DTL)
- 1 554th Combat Support Group, Nellis Air Force Base (OT, FWW/DTL)
- 1 Defense Advanced Research Projects Agency, Arlington (Materials Science Division, Snow)
- 1 Defense Nuclear Agency (Shock Physics Directorate)
- 12 Defense Technical Information Center
- 1 Department of Defense-Institute for Defense Analyses Management Office (DIMO), Alexandria
- 2 Colorado Seminary, Denver Research Institute, Denver, CO
 - R. Recht (1)
 - J. Yatteau (1)
- 1 Lewis Research Center (NASA), Cleveland
- 1 California Institute of Technology, Jet Propulsion Laboratory, Pasadena, CA (Technical Library)
- 2 Hercules Incorporated, Allegany Ballistics Laboratory, Cumberland, MD
- 1 IIT Research Institute, Chicago, IL (Department M, Document Librarian)
- 1 Los Alamos National Laboratory, Los Alamos, NM (Reports Library)

- 1 Princeton University, Forrestal Campus Library, Princeton, NJ
- 1 Stanford Research Institute, Poulter Laboratories, Menlo Park, CA
- 1 The Boeing Company, Seattle, WA (MS 8C-61, E. Wilhelm)
- 2 The Johns Hopkins University, Applied Physics Laboratory, Laurel, MD (Document Library)
- 2 The Johns Hopkins University, Applied Physics Laboratory, Chemical
Propulsion Information Agency, Laurel, MD
- 1 The Rand Corporation, Santa Monica, CA (Technical Library)
- 1 University of California, Lawrence Livermore National Laboratory, Livermore, CA (Code L39, Landingham)